Master Thesis

Fibre Reinforced Additive Manufacturing of Eco-efficient Topology Optimised Structures

D. Canosa Ybarra

Delft University of Technology

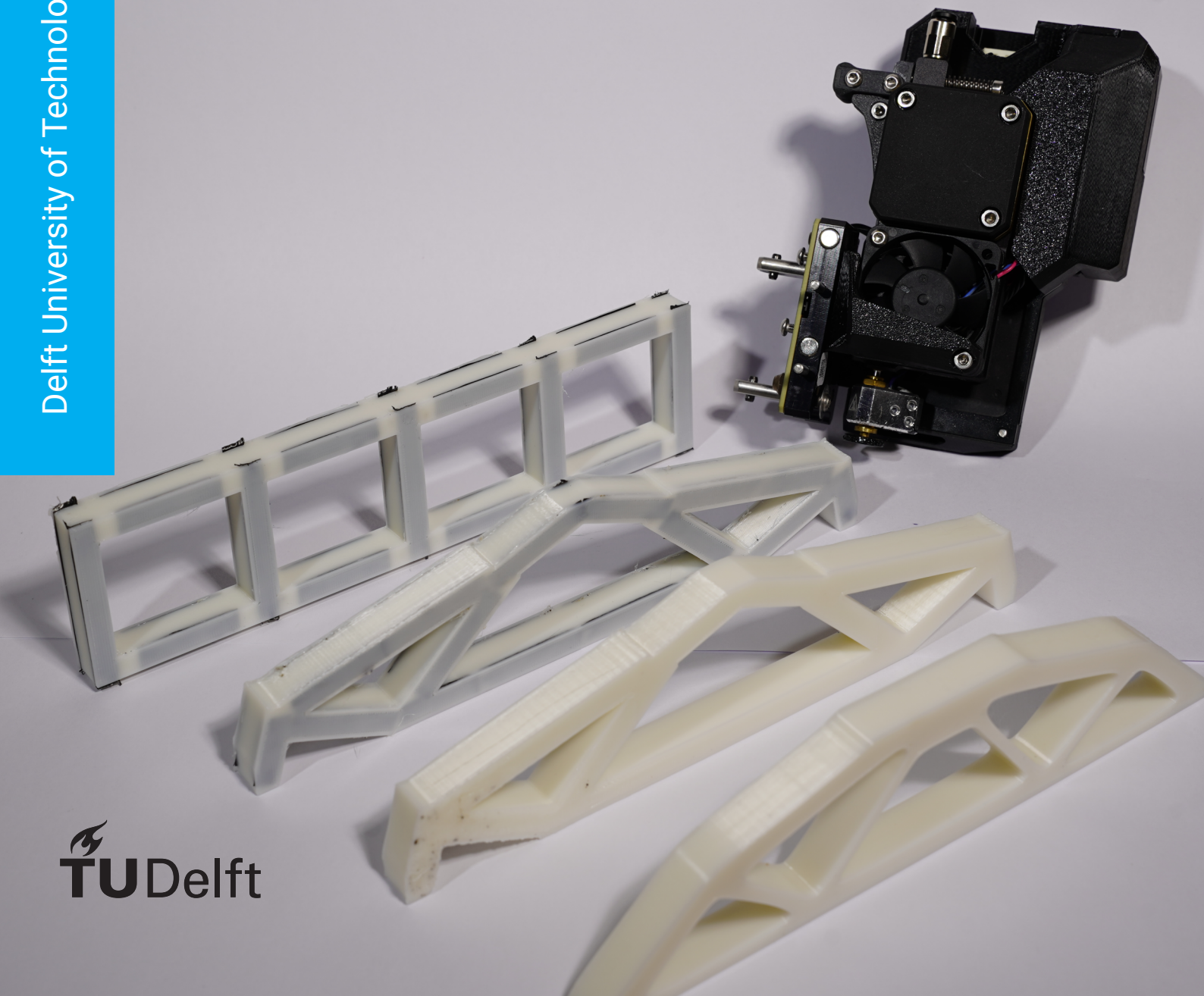

TU Delft

This page is intentionally left blank.

Master Thesis

Fibre Reinforced Additive Manufacturing of Eco-efficient Topology Optimised Structures

by

D. Canosa Ybarra

to obtain the degree of Master of Science
at the Delft University of Technology,
to be defended publicly on Thursday May 28, 2026 at 14:00 PM.

Student number:	4839277	
Project duration:	December 23, 2024 – May 28, 2026	
Thesis committee:	Prof. Kunal Masania,	TU Delft, Professor Supervisor
	Dr. Chintan Jansari,	TU Delft, Daily Supervisor
	Prof. Clemens Dransfeld,	TU Delft, (Chair) Committee Member
	Prof. Baris Caglar,	TU Delft, Committee Member

TU Delft

Preface

This work is the result of combining a long-standing passion for 3D printing with the knowledge and skills I developed during my Master's in Aerospace Structures and Materials at TU Delft. When the opportunity arose to explore composite materials through the lens of additive manufacturing, it felt like a natural convergence of everything I had been working towards and this thesis is the product of that journey. I would like to express my sincere gratitude to Chintan Jansari for his supervision and support throughout this project. His guidance kept the work on track and his feedback consistently pushed me to think more critically and rigorously. I would also like to thank Kunal Masania and the rest of the SML group for welcoming me into their research community. The open and collaborative atmosphere they fostered made this a genuinely enjoyable experience, and I am grateful for their willingness to help whenever I needed it. I would further like to extend my thanks to the technicians whose practical support was essential to the experimental work in this thesis. In particular, I am grateful to Dave Ruijtenbeek for his invaluable assistance with the mechanical testing — his expertise and patience made a real difference.

D. Canosa Ybarra
Delft, January 2026

Contents

List of Symbols

AFP Automated Fibre Placement

AM Additive Manufacturing

ATL Automated Tape Laying

ATLAM Advanced Tape Layer Additive Manufacturing

CFRP Carbon Fibre Reinforced Polymer

CTE Coefficient of Thermal Expansion

DIC Digital Image Correlation

DTO Density-based Topology Optimisation

ePa12 Engineered Polyamide 12 (substrate filament material)

FDM Fused Deposition Modelling

FEM Finite Element Method

FRC Fibre Reinforced Composite

FRP Fibre Reinforced Polymer

GPTO Geometric Projection Topology Optimisation

GPTOGR Geometric Projection Topology Optimisation Ground Case

GPTONT Geometric Projection Topology Optimisation without Tapes

GPTOPP Geometric Projection Topology Optimisation Post Processed

MBB Messerschmitt-Bölkow-Blohm (beam benchmark load case)

MDM Metamorphic Development Method

MMM Moving Morphable Method

Pa12 Polyamide 12 (Nylon 12)

PMC Polymer Matrix Composite

SIMP Solid Isotropic Material with Penalisation

TO Topology Optimisation

TP Thermoplastic

TS Thermoset

UD Unidirectional

α_s Substrate density variable -

α_t	Tape density variable	-
ν	Poisson ratio	-
ν_{12}	Poisson ratio in the 1-2 plane	-
ϕ_s	Signed-distance function for substrate	-
ϕ_t	Signed-distance function for tape	-
ρ	Density	g/cm^3
σ_{st}	Failure strength	MPa
σ_{yy}	Normal stress in the y-direction	MPa
ε_{vm}	Von Mises strain	-
ε_{xx}	Normal strain in the x-direction	-
ε_{xy}	Shear strain in the xy-plane	-
ε_{yy}	Normal strain in the y-direction	-

(x_{t1}, y_{t1})	Tape start-point coordinates	mm
(x_{t2}, y_{t2})	Tape end-point coordinates	mm
E	Elastic (Young's) modulus	MPa
E_1	Elastic modulus parallel to fibre direction	GPa
E_2	Elastic modulus perpendicular to fibre direction	MPa
E_m	Elastic modulus of matrix	MPa
E_{2f}	Elastic modulus of fibre perpendicular to fibre direction	GPa
F_y	Applied force in the y-direction	kN
G	Shear modulus	MPa
G_{12}	Shear modulus in the 1-2 plane	MPa
I	Embodied CO_2	$kgCO_2/kg$
k	Structural stiffness	kN/mm
k_{exp}	Experimentally measured stiffness	kN/mm
k_{num}	Numerically predicted stiffness	kN/mm
L_s	Substrate length variable	mm
L_t	Tape length	mm
L_t^{min}	Minimum allowable tape length	mm
RE	Relative error	%

t	Tape thickness	mm
v_f	Fibre volume fraction	-
v_m	Matrix volume fraction	-
w	Tape width	mm
W_s	Substrate width design variable	mm
W_t	Tape width design variable	mm

1

Introduction

1.1. Motivation

Global warming is one of the most important issues humanity is facing in this century, and addressing it will require all industrial sectors to work-together to find innovative ways to reduce CO_2 emissions. Air travel contributes 2.5% of global CO_2 emissions [1], and, as the number of air travel passengers increases at a rate of 5% per year, it is expected to continue to grow at a similar rate throughout this century, as will projected emissions from the sector.

Structures used in the aerospace industry are mainly made of carbon fibre reinforced polymer composites. The sector is extensive in its use of these high performing yet environmentally costly carbon fibres (high embodied CO_2). Carbon fibres are created from polyacrylonitrile (PAN) fibres, which are stabilised, carbonised, and graphitised. This process is energy-intensive as they must be placed in an environment of 180-300°C, 300-1200°C and 1500-2800°C respectively, this makes their embodied CO_2 high. Avoiding complete use of these fibres is not an option, as the environmental cost of their production is far outweighed by the fuel savings in the operation of the aircraft. This comes from the high specific stiffness and strength of carbon fibres in the fibre direction. In Fibre Reinforced Polymer (FRP) structures, carbon fibres have a high alignment of internal bonds and, therefore, a higher specific stiffness in the direction of the fibres. The fibre directions can be tailored to enhance the load-bearing capacity of the FRP structures. This high specific specific stiffness and strength of FRP structures allow lighter aircrafts, resulting in a higher fuel efficiency and fatigue resistance. Therefore, an aircraft can have a longer service life with the more efficient use of the embodied CO_2. However, direction-dependent behaviour of FRP requires complex design and manufacturing techniques.

Conventionally, FRP structures are created by stacking laminas of unidirectional or weaved fibres in varying orientations. As, a laminate used in a fuselage can have up to 60 laminae, hand laying of fibres becomes expensive and time consuming. Therefore, automated techniques such as Filament Winding (FW) and Automated Tape Laying (ATL) are typically used. An ATL machine can lay 3, 6 or 12 inch wide tapes at speeds of up to 1 m/s of pre-impregnated FRPs to deposit layers of the laminate. Since these tapes are wide and thin, there is little ability to steer them as they are being deposited, but a structure can have locally varying loads, changes in the directionality of the load within a component, concentrated loads or holes, all features that could benefit from changes of fibre direction within a lamina. In other manufacturing methods such as automated fibre placement (AFP) the fibres can be steered to create variations in the layup to align the fibres to local load directions. The drawback of AFP being the lower deposition rate as it is a placement tape of $\frac{1}{8}$ to $\frac{1}{2}$ inches wide at $0.6 m/s$ this is a maximum deposition rate area of $0.3 m^2/s$ compared to ATLs $12 m^2/s$.

In ATL and AFP the limited steering combined with the geometry of the tapes will limit the paths that can be deposited. Diverging or converging tows will leave gaps which a rectangular tape geometry cannot be filled. Ply drops or increases are avoided because they can become crack initiation points. Therefore, at times tapes are used to spatially fill a layer or more laminae are used than required in a laminate. This is a waste of a material that has high stiffness, strength, and such high embodied CO_2.

Additive manufacturing (AM) fused filament fabrication (FFF) is a method in which an extruded

thermoplastic filament is pushed out of a heated nozzle to deposit beads of molten thermoplastic; typically, layers are stacked to create a final product. AMFFF products without fibre additives (ePa12, 4.6 $kgCO_2/kg$) tend to have 12 times less embodied CO_2 than ATL (54.8 $kgCO_2/kg$). This method has shown great shaping freedom and has the ability to cover for the drawbacks in ATL. Therefore, a new manufacturing method in development is ATLAM, where the excellent mechanical properties but the poor shaping freedom of ATL can be complemented with the shaping freedom and low embodied CO_2 AM. In this method, the ply drops could be replaced with thermoplastic filler material and the tapes can be used sparingly to reduce the end parts embodied CO_2.

The fusion of both manufacturing methods has added to the complexity in design; previously a design of an ATL part would include an optimisation for the layup size and orientation, now there is an added geometric variable of should that section be FRP or Thermoplastic. In addition, as embodied CO_2 is important, this requires a new framework to optimise the parts. Size and shape optimisation is too limited, as the solutions would be sensitive to the initial geometry that was picked. Thus, a method is needed that can handle the increase in the design space and find optimal solutions for performance metrics such as stiffness to weight and embodied CO_2.

Topology optimisation (TO) is a method that can be used in structural optimisation which keeps FEA in the loop. This method is much less sensitive to the initial geometry and provides parts with high specific stiffness. The most common TO approaches are density based and level set. Density based methods will use a pseudo non-integer density of the material to allow the optimisation problem to smoothly introduce or remove material. This allows the optimiser to converge to a solution which is typically then penalised for using non integer densities to create the final design. Level set methods will use a higher dimensional space where a function crossing the zero plane is contour of the design.

Among TO methods, there are emerging methods called Moving Morphable Method (MMM) and Metamorphic Development Method (MDM). In these methods, the shape is deliberately constrained to a design primitive such as a polygon with some constraints on its ability to morph. The manufacturing methods mentioned previously, such as ATL and AFP, are limited to the deposition of rectangular tapes; therefore, these emerging TO methods could be combined with ATLAM to design structures whose manufacturing constraints are set implicitly in the optimisation scheme, as seen in MMM and MDM methods.

Another method, geometry projection method holds several advantages over the Moving Morphable Method (MMM). Most notably, it can remove bars from the design space entirely during optimisation, a capability MMM lacks. Because the geometry projection is effectively a density-based method operating on a fixed grid with standard FEA, it avoids the need for XFEM that MMM requires to explicitly represent structural boundaries, XFEM incurs additional computational cost and re-meshing overhead.

Geometric Projection Topology Optimisation (GPTO) has previously been implemented to design thermoplastic substrate structures reinforced with tape with high specific stiffness and low embodied CO_2. The approach has been tailored to the constraints posed by ATLAM by setting the primitives to the shape of the tapes.

The GPTO framework is yet to be validated with experiments, this is vital to create confidence in the methodology and to show it reflects the behaviour of the structures that are designed. There are 2 claims in this approach, 1 that the model can accurately predict the behaviour of the material, and 2 that the designs are optimum. For the first claim, validation should be based on destructive mechanical tests of designs made through GPTO. For the second claim it is impossible to verify without exploring the whole design space, so validation should rely on showing an improvement over other methods that confidently find optimums in a design space such as density based methods.

1.2. Problem Statement

ATLAM works on a 1-10m scale that makes testing prohibitively expensive due to the material that is needed to create large fibre reinforced polymer structures can cost up to 80£/kg of thermoplastic and 200 £/kg for CFRP material, and mechanical testing of the structure will require a specialised testing machine and set-up. An alternative method needs to be developed to generate mechanically similar structures to validate the design methodology at a lower cost and facilitate a accelerated development cycle. An experiment must be designed to validate the current method and compare it to other topology optimisation methods.

This thesis will set out to design a manufacturing method that can create structures mechanically similar to ATLAM products, but that can be made on a conventional 3D printer. A benchmark loadcase will be chosen, designs will be made for this loadcase. The manufacturing method will then be used to produce fibre reinforced polymer structures. Then these designs will be tested to compare their performance with the models used in the GPTO algorithm.

1.3. Report Outline

The remainder of the thesis report is structured as follows. The relevant literature and background to the thesis is presented in Chapter 2. Using the context given in the previous chapter, the knowledge gap is identified and a set of research questions is proposed in Chapter 3. The manufacturing method for a desktop ATLAM is developed in Chapter 4. Then, the desktop ATLAM method is used to produce samples of GPTO designs to test the stiffness in Chapter 5. Finally, the conclusions of this thesis are compiled in Chapter 6.

2

Background

2.1. Composites in Aerospace

The evolution of aircraft materials has progressed from early wood-and-fabric constructions to advanced metal and composite structures over the past century. The Wright brothers constructed the first successful powered airplane in 1903 using a structure made primarily of wood, canvas, and steel wires for control [2]. The first fully metallic aircraft, the J 1 Junkers monoplane, appeared in 1915 [3]. During the 1920s and 1930s, aircraft structures were built mostly from aluminium because of its high strength-to-weight ratio [4]. By the 1950s, aluminium dominated most of the airframe, and titanium alloys were introduced for selected high-stress and high-temperature components [4]. In the 1940s and 1950s, fibreglass composites were first used for components such as fairings and radomes [4], and by the 1970s, carbon-fibre composites began to appear increasingly in aircraft structures [4].

Today, carbon fibre composites are widely used in modern commercial aircraft thanks to advances in manufacturing that allow larger and more complex parts to be produced. Around a quarter of the Airbus A380, introduced in 2005, is made from composite materials, marking a major step in their adoption. The Boeing 787 Dreamliner took this even further, becoming the first major commercial airliner with a composite fuselage and wings, and using composites in most airframe components, by weight 50% composite, with the rest mainly aluminium, titanium, and steel. Similarly, the Airbus A350 XWB uses more than 50% composites, a design choice that delivers about a 25% reduction in fuel burn compared with aluminium-based competitors, highlighting the efficiency gains that composites offer in today's aviation industry.

In the aerospace sector, structural components must exhibit high stiffness and strength relative to their weight, along with strong resistance to fatigue. They should also possess sufficient elongation before fracture, which generally rules out brittle ceramic materials, and they must demonstrate a high level of reliability throughout their service life, as well as good corrosion resistance and, in some applications, resistance to high temperatures.

In aerospace engineering, a wide range of advanced materials is used, each selected for its specific mechanical and physical properties. Titanium alloys are commonly used in high-strength, high-temperature structural components such as engine mounts and landing gear due to their excellent strength-to-weight ratio and corrosion resistance. Aluminium alloys are widely used in fuselage skins, wing structures, and internal frames because they are lightweight, relatively inexpensive, and easy to form and machine. Nickel superalloys are primarily found in the hottest sections of gas turbine engines—such as turbine blades and discs—where they maintain strength and creep resistance at extreme temperatures. Glass fibre-reinforced polymers (GFRPs), are often used in radomes, fairings, and secondary structures where cost and good dielectric properties matter more than maximum stiffness. GLARE (glass laminate aluminium reinforced epoxy), which is a fibre metal laminate combining thin aluminium sheets with glass fibre/epoxy layers, is used in aircraft fuselage panels and upper shells to improve fatigue and impact resistance while reducing weight. Carbon fibre-reinforced polymers (CFRPs), made from carbon fibre tows impregnated with polymer resins (prepregs), are used in primary load-bearing structures like wings, fuselage barrels, and tailplanes, where high stiffness and low weight are critical.

In 1950, non-structural fibreglass parts were first used on the Boeing 707, followed by the introduction of the first primary composite structures on the Airbus A310 in 1980, and composites are now heavily used in major airliners. These materials provide a superior strength- and stiffness-to-weight ratio compared with aluminium and can be engineered with directional properties to align with design loads, thereby achieving an even higher stiffness-to-weight ratio.. Additionally, they provide good resistance to cyclic loading and excellent corrosion resistance, which can extend the service life of an aircraft.

In today's aircraft production, 50% of the components are manufactured from CFRPs, continuing a growth trend that began in the 1960s [5]. As the price of CFRPs continues to fall, their share of use in industry is rising, especially in the automotive, biomedical, maritime, and construction sectors [6, 7]. Conventional composite fabrication techniques, such as autoclave processing and vacuum bag molding, continue to rely on manual labor, are time intensive, and demand substantial energy input [6]. The aviation sector is increasingly adopting thermoplastics rather than thermosets for structural components because they offer greater toughness and require less energy to process. In addition, research is underway on recycling CFRPs, a task that is considerably more straightforward with thermoplastics due to their ability to be melted or reshaped [5].

Composite use in aerospace is dominated by fibre-reinforced composites (FRCs), most of which are continuous fibre FRCs. In these composites, carbon fibres are used most frequently because they offer the highest strength-to-weight ratio; however, glass or aramid fibres are sometimes used instead to reduce cost or to provide particular electromagnetic properties. The fibres typically have diameters of about 10 μm for glass and 7 μm for carbon, which makes them individually flexible and fragile, so they require a matrix to protect them and keep them aligned [8].

2.2. Fibre Reinforced Composites in Aerospace

Fibre-reinforced composites are made up of strong, stiff fibres embedded within a matrix that keeps them aligned along the main tensile direction. Although the fibres deliver high tensile strength, the overall structure can be relatively thin and therefore prone to buckling. The matrix phase preserves fibre alignment, facilitates load transfer between fibres, and shields them from damage and environmental exposure. Fibre-reinforced composites are commonly categorised by the type of matrix they use, such as polymer, metal, ceramic, or carbon matrices [8]. This thesis concentrates on polymer matrix composites, as these are most applicable to the aerospace sector; ceramic and carbon matrix composites are typically too brittle, whereas metal matrix composites are generally more challenging to manufacture.

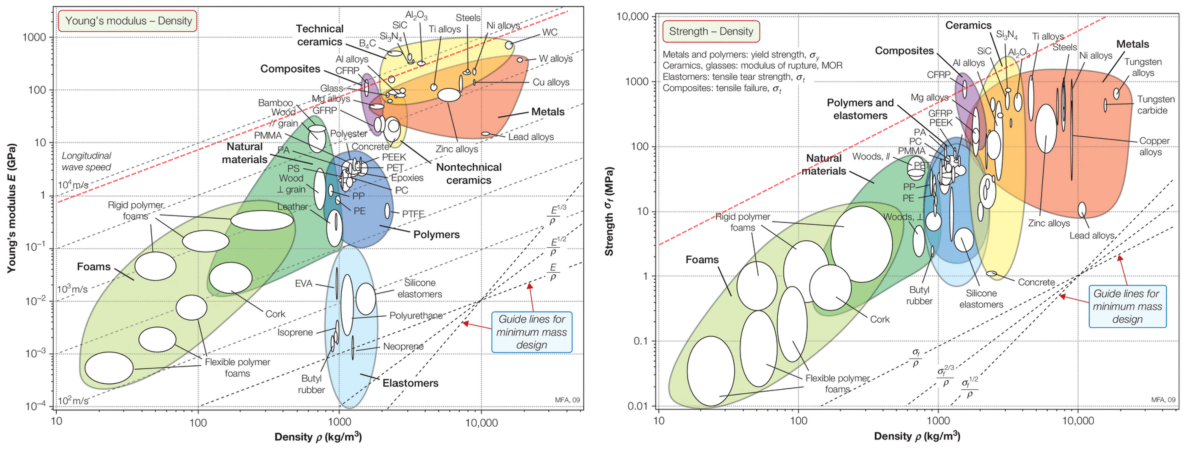

(a) Specific E modulus

(b) Specific strength

Figure 2.1: Ashby plots of mechanical properties of engineering materials

In figure Figure 2.1a and Figure 2.1b it can be seen that carbon reinforced polymers have some of the highest specific stiffness and strengths from engineering materials. The only competing materials are ceramics that are too brittle for most structural applications.

Fibre-reinforced composites feature a large interfacial area between fibres and matrix, which promotes efficient stress transfer from the matrix into the fibres and leads to stiffness and strength characteristics that are predominantly fibre-dominated, in contrast to systems using particulate or flake reinforcements where the interface tends to fail before the reinforcement is fully loaded which results in matrix-dominated stiffness and strength.

Fibre-reinforced composites can be categorized by fibre length as short (L<1 mm), long (L≥1 mm), or continuous (L limited by the component dimensions)[9]. Short fibres offer the benefit that, at sufficiently low fibre volume fractions, they can be suspended within the polymer melt during flow, enabling short-fibre-reinforced 3D printing and injection molding. Long fibres, however, do not flow as easily, so forging processes are typically employed, requiring high pressures ($\tilde{1}$00 bar) to produce defect-free components[10]. In most short- and long-fibre FRCs, the fibres are randomly oriented, resulting in quasi-isotropic behaviour[9]. In contrast, continuous FRCs are manufactured with controlled fibre orientations and arranged in laminae, which imparts anisotropic properties.

Fibre-reinforced composites can be engineered as laminas with anisotropic behaviour, enabling them to exceed the stiffness-to-weight performance of isotropic materials when the loading is strongly directional. By stacking individual laminae at different fibre orientations to create a laminate, reinforcement can be concentrated along the main load paths while also offering excellent fatigue endurance limit (up to 60% of ultimate tensile strength[11]).

Historically, thermoset (TS) polymer matrix composites (PMCs) have been the dominant choice. This is mainly because their resins are cheaper, can be processed at lower pressures and temperatures, and therefore require less capital investment to manufacture TS components. Moreover, the low viscosity of thermoset resins makes it possible to infuse very large structures, such as wind turbine blades, at room temperature, something that cannot be achieved with thermoplastics (TPs). The fact that these composites can be produced without an autoclave has been a major factor in their widespread use in both shipbuilding and wind energy applications.

There are two principal approaches for manufacturing composite parts with thermoset resins. In the first, the resin and hardener are supplied separately and mixed just prior to infusion (A-stage). In the second, a pre-mixed matrix is used, with the reaction rate slowed down for storage (B-stage). The A-stage route typically employs vacuum-assisted resin infusion: the resin is drawn through the fibre preform by a vacuum pump positioned at the opposite end. With this technique, achieving a precise fibre volume fraction is challenging; if it is not well controlled, the component can develop resin-rich or resin-starved regions, which can significantly degrade its performance. The B-stage route, on the other hand, requires freezer storage for the prepreg plies, because the resin will cure quickly if maintained at elevated temperatures.

The other category of polymer matrix is the thermoplastic. Thermoplastics offer a major advantage in that their production cycle can be very short. In contrast, thermosets require time for chemical cross-linking, which can be accelerated by heat but still imposes a limit on processing speed. A disadvantage of thermoplastics is their higher material cost compared to thermoset resins. However, in the aerospace sector this drawback can be offset by the potential for automated manufacturing and the improved impact resistance they provide.

The global push toward a circular economy is increasing the focus on re-use, recycling, or downcycling of components after their initial service life. Because thermoplastics can be remelted, it becomes possible to reshape the original product at the end of its life into a new component for a

different application.

Given the high specific stiffness and strength of continuous FRCs, along with the increasing research on recycling and reusing thermoplastic-matrix FRCs, it becomes evident that, to meet the demands of an eco-efficient aerospace industry, attention should be directed toward continuous fibre-reinforced composites with thermoplastic matrices. Consequently, this necessitates the production of continuous fibre thermoplastic composites.

2.3. Manufacturing of Continuous Fibres Thermoplastics Composites

Unlike thermoset resins, thermoplastics do not undergo curing. As a result, they are usually handled in solid form (most often as pellets) and then heated until they melt during processing. At processing temperatures, thermoplastics exhibit high viscosity, which restricts their flow and therefore requires the use of higher pressures.

There are two main approaches to combining thermoplastics with fibres. In the first, semi-finished products are manufactured, typically via pulltrusion, to produce continuous fibre-reinforced thermoplastic tapes that are later consolidated into the final component. In the second approach, the fibres are directly impregnated with the thermoplastic matrix during the final manufacturing process.

Any high-quality thermoplastic composite manufacturing process must account for the key parameters shown in Figure 2.2a, and defects arise when one or more of these are not properly controlled. Fibre deposition defines the position, orientation, and stacking sequence of the fibres, which directly affects the mechanical performance. Impregnation introduces the matrix material into the fibre network and ensures adequate wetting to minimise voids and enable effective load transfer. Heating raises the temperature above the melting point to promote bonding. Matrix pressure is applied to reduce void content and consolidate the layers. Fibre compaction aligns the fibres and regulates the laminate thickness. Finally, cooling governs the crystallinity, residual stresses, and dimensional accuracy of the part.

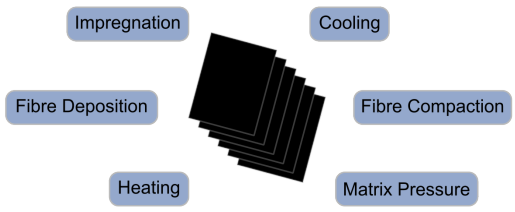

(a) Key Parameters in Polymer Composite Processing [12]

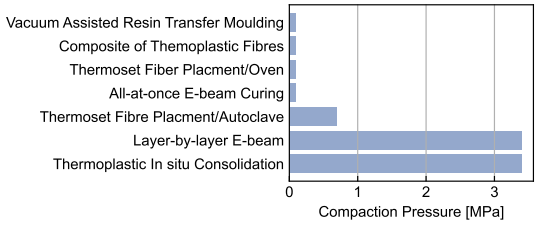

(b) Compaction pressure for manufacturing method [13]

Figure 2.2: Key parameters in composite processing and characteristic compaction pressures of multiple manufacturing methods

Thermoplastic composite manufacturing processes encompass pultrusion, used to fabricate continuous components with a uniform cross-section such as beams and profiles; filament winding, ideal for axisymmetric parts like pipes and pressure vessels by winding heated, impregnated fibres onto a rotating mandrel; compression molding, injection molding, and stamp forming, which shape thermoplastic composites by applying heat and pressure to melt and consolidate the material into complex forms; and automated fibre placement (AFP) / automated tape laying (ATL), advanced robotic techniques that deposit heated thermoplastic tapes or tows layer by layer to produce high-performance, large structural parts with accurately controlled fibre orientation [14].

Automated Fibre/Tape Placement is an additive manufacturing technique that is used to create thins structures from either thermoset or thermoplastic infused fibres. In this method the fibre deposition is handled by a machine which can place the layers accurately. The difference between

tape and fibre placement is the width of tow that the machine places, this changes the curvature that the machine can steer the composite before introducing defects and the speed of deposition [15]. It is a trade-off between having your fibres be able to take steep curvatures that can help the part be more materially efficient or being more time efficient. A(F/T)P involves laying a flat tape of composite with one or multiple rollers, this is then combined with a autoclave or oven to cure for a thermoset matrix tape or can be in-situ consolidated for a thermoplastic.

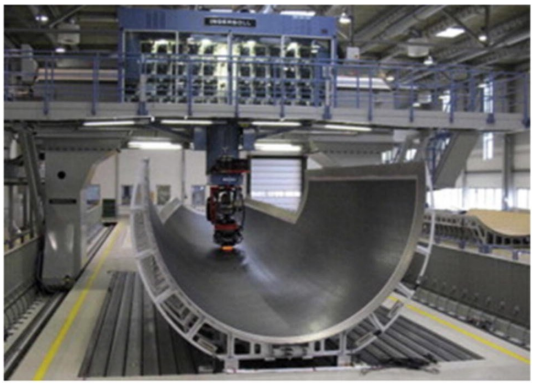

(a) Fuselage mould with layers of tape being placed by gantry mounted deposition tool

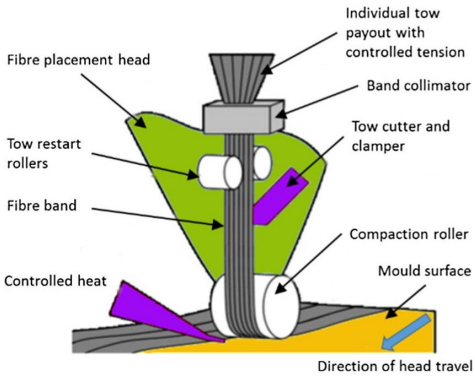

(b) Simplified process schematic showing key components in a AFP machine

Figure 2.3: Automated Fibre Placement (AFP) [16]

The compaction rollers in AFP are set on free-spinning bearings and provide contact pressure on the top side of the composite to remove voids and increase molecular diffusion between the layers in the lay-up without shearing the layer as it passes over. Studies suggest that the flexibility in the roller is key to providing sufficient consolidation force on the tape such that small irregularities in the surface will not cause variations in contact pressure [17].

Controlling the temperature in the material is key to ensure that the composite is properly bonded to the previous layer. To do this industry uses hot gas torches, lasers and infra-red emmitors aimed at the nipping point. The nipping point is the region between the tape being deposited and the previous layer, just in front of the roller. This is done to make sure the mold side gets enough heat flux to fuse but avoid that the roller side of the tape gets hot as the tape will get tacky and stick to the roller post-consolidation.

Studies have shown that it is best to apply pressure and heat but cool the part before releasing the pressure to make the molecules immobile in their compacted state. This avoids spring back which will allow voids to reform again in the composite.

In the joining of polymer composites the compaction and the temperature are both key aspects. The temperature will soften the polymer and make the molecules mobile whilst the the compaction pressure will remove the asperities between the two surfaces so that their area in contact is maximized [18]. Therefore it is key to apply the pressure on the composite and heat it whilst the pressure is being applied, then ramp down the heat. Only when the composite is fully cooled should the consolidation pressure be reduced.

In filament winding, a mandrel shaped like the final component is mounted on a rotating spindle. A carriage positioned alongside the mandrel lays down thermoset resin–impregnated tows as the spindle turns. By adjusting the carriage speed along the mandrel's length, different fibre winding angles can be obtained. The component is built up in multiple layers with varying orientations until the required thickness is reached, after which it is vacuum bagged and cured in an autoclave or oven.

Filament winding is primarily employed for manufacturing drive shafts, helicopter rotor blades, pipelines, and pressure vessels. Deposition speeds of 90–110 m/min can be achieved [8], although

the method is restricted to producing hollow, axisymmetric components [8].

2.3.1. Automated Fibre Placement

Automated Fibre Placement (AFP) is a process in which a deposition head mounted on a gantry or robotic arm lays down pre-impregnated, fibre-reinforced tapes, typically 1/8 inch to 1/2 inch wide [19], onto a mold surface. An AFP system is usually equipped with a heating unit, which may use hot gas (the most economical and safest option), a laser (suitable only for carbon fibre reinforcements), or xenon pulsed light (a costlier but more precisely controlled heat source).

The heater concentrates energy at the nip point, the initial contact zone between the incoming tape and the underlying layer or mold. This localized heating raises the temperature of both the tape and the substrate. For thermoset materials, this increases tack, helping the tape stay in place after deposition. For thermoplastic materials, it conditions the interface to enable proper bonding[20].

The tapes are delivered to a compaction roller that ensures close contact with the previous layer, promoting fusion bonding[21]. Additionally, the AFP machine incorporates a tape-cutting mechanism that allows the placement process to be stopped and restarted as required.

AFP is an automated manufacturing process that has enabled users to cut costs by 43% and increase the deposition rate to 1.9 kg/hr [19]. AFP can process both thermoset and thermoplastic materials; in the case of thermoplastics, it permits in-situ consolidation of the component, eliminating the need for autoclave curing [22]. The primary drawback of in-situ consolidation is the relatively low crystallinity of the matrix compared to autoclaved laminates[23]. The tapes laid down by AFP can be steered, creating intra-laminar variations in fibre orientation that improve the structural design. As a result, AFP structures are lighter, stiffer, and stronger, while material waste has been reduced from 62% to 6% compared to manual ply collation [19].

Future developments in AFP technologies are expected to emphasise machine modularity and broader accessibility. It is argued that AFP should evolve in a direction similar to 3D printing by introducing smaller, modular, and more adaptable systems [19]. Another key trend is enhanced tooling flexibility, as illustrated by General Atomics Aeronautical Systems Inc. (GA-ASI) [24], which has shown that a second robot can be employed to supply the reaction force needed by the placement head to lay AFP tows, thus making it possible to deposit tows without relying on a mold. Furthermore, current efforts also involve the design of high-temperature sensors and bearings tailored for AFP applications [19].

2.3.2. Automated Tape Laying

Automated Tape Laying (ATL) is a more straightforward predecessor of Automated Fibre Placement (AFP), introduced to reduce the high expenses associated with manual composite layup. Compared to AFP heads, ATL heads are generally heavier and therefore are commonly mounted on gantry systems, which increases the initial investment cost [25]. Like AFP, ATL relies on a heater, a roller, and a cutter to place segments of pre-impregnated fibre-reinforced polymers (FRPs), but it makes use of a broader tape, typically between 3 and 12 inches wide. During layup, the tapes must be positioned side by side with a gap of 0.5 mm to 1 mm to compensate for placement inaccuracies [25].

ATL has a more limited steering capability, with a minimum radius of 610 cm when using 150 mm tape, whereas AFP can achieve a minimum radius of 50.8 cm [26]. The operations of cutting, turning, and repositioning take about 9 s on ATL and about 7 s on AFP [27], primarily because the heavier ATL head requires more time to accelerate and decelerate. Regarding productivity (kg/h), AFP is more effective for smaller components (on the order of 10 m^2), while ATL provides higher efficiency for larger components (around 250 m^2) [25].

Ongoing work in ATL concentrates on implementing in-situ monitoring to detect and classify

defects using several non-destructive testing approaches, on in-situ defect repair, and on enhancing the design flexibility of ATL. Thermography is one such method, enabling the identification of foreign object debris, such as fragments of the roller that have broken off and become embedded in the composite. A second method is profilometry, which can detect missing tows, gaps, and overlaps, while computer vision techniques can be applied to recognise wrinkles and twists in the tows [25]. Another approach is to explore repairing defects, such as gaps, with a 3D printer using carbon continuous fibre-reinforced plastics [28]. Additionally, tape spreading can be applied to achieve variable tape widths during placement by adjusting the roller pressure [29] which can expand the design freedom of ATL.

2.3.3. Additive Manufacturing

Additive manufacturing is a method where a part is made by slicing a 3D model into a set of contours that describe the boundary of the object at parallel planes and then depositing the material within those contours with the objective of an end result that resembles the initial 3D model.

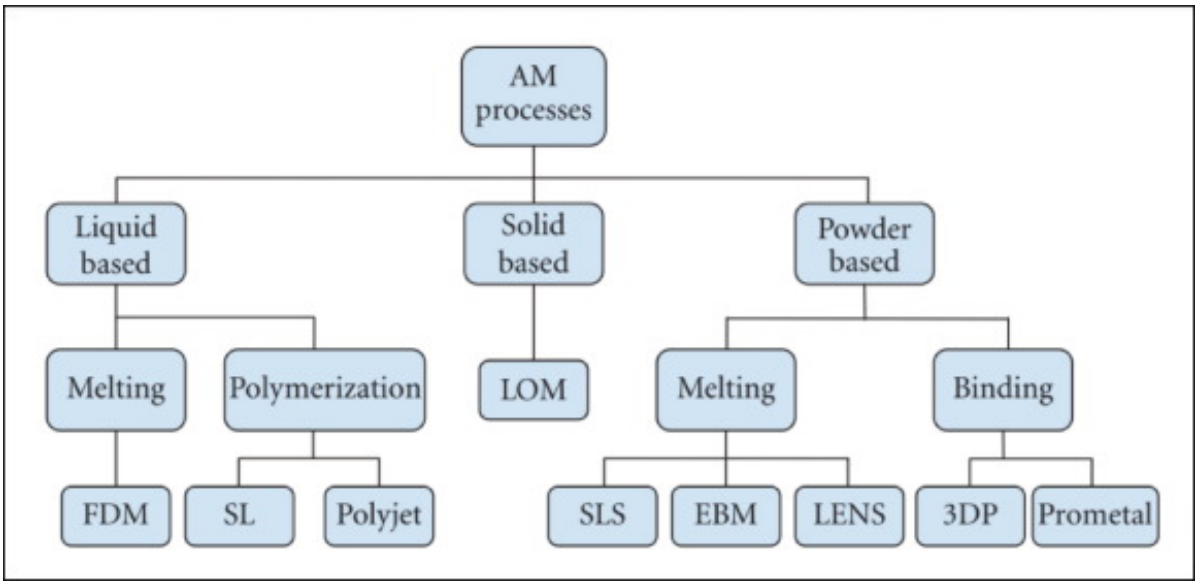

Figure 2.4: Additive manufacturing types map [30]

As shown in Figure 2.4, AM processes can be categorized into liquid-based, solid-based, and powder-based techniques. In powder-based processes, a powder bed is selectively sintered, after which a new layer of powder is spread for the next layer. Once all layers have been built, the part is extracted from the surrounding powder, which can often be recycled. In solid-based processes, Laminated Object Manufacturing (LOM) involves laser-cutting the part contours along parallel planes from flat sheets of material and stacking them vertically to form the final object. In liquid-based processes, either a UV-sensitive resin is cured layer by layer, as in vat polymerization, or a thermoplastic filament is melted and extruded through a nozzle to build the object, as in fused deposition modeling [30].

Additive manufacturing is materially efficient and enables complex geometries that are not possible in conventional manufacturing methods (milling and turning). The additional freedom in geometry has allowed for more efficient material placement which allows lighter and stiffer structures.

2.3.3.1 Fused Deposition Modelling

Fused Deposition Modelling (FDM) is a additive manufacturing method that uses a thermoplastic filament (a circular extrusion that is often coiled) to which is driven by extruder wheels through a heated nozzle to melt and flow to deposit beads in paths that will build up a part layer by layer, as

seen in Figure 2.5a. The first layer will be deposited on a heated bed which will allow it to adhere. The process will use an extruder which is typically mounted on a gantry with typically 3 degrees of freedom.

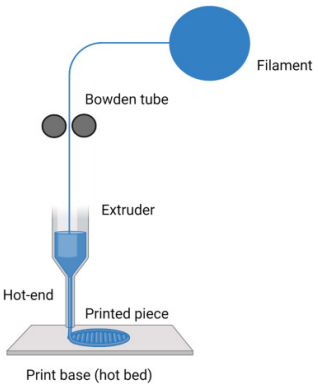

(a) Fused deposition modelling process [31]

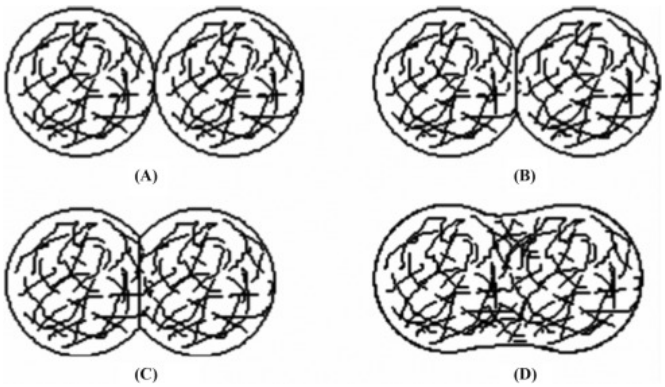

(b) Fused deposition modelling bonding. (A) Initial contact between adjacent filaments with distinct, non-interacting polymer chain networks. (B) Early-stage sintering showing surface wetting and the onset of interfacial contact. (C) Progressive chain diffusion across the filament boundary as thermal energy drives reptation of polymer chains into the neighbouring layer. (D) Advanced coalescence with significant neck growth and extensive chain entanglement across the interface, resulting in improved interlayer mechanical bonding.[32]

Figure 2.5: Fused deposition modelling (FDM) process and interlayer bonding mechanics

An issue in FDM is the inter layer strength, once the nozzle lays a layer, it begins to cool down so when the next layer is placed the molten polymer is laid on a solidified bead of polymer. Since not both sections of the interface are molten there is limited mobility of the polymer chains across the interface which causes the sections between layers to have low crystallinity and not many polymer chains crossing the plane. This lowers the mechanical properties in that direction.

Fused deposition modelling offers great geometric flexibility and supports the processing of many different materials[31]. Although it is a relatively inexpensive manufacturing technique, the resulting parts generally exhibit inferior properties compared with those produced by injection moulding, and the process is also slower. On the other hand, with FDM, the development cycle and the time required to implement changes are significantly reduced, since there are no moulds to reproduce or specialized tooling to prepare. The mechanical performance is strongly influenced by the selected printing parameters, including layer height, printing temperature, build orientation, and print path[33].

FDM is used across a wide range of industries, from biomedicine for producing prostheses and implants to engineering for manufacturing moulds and drone components. Many other sectors also rely on it as a tool for quickly prototyping designs before moving on to the final manufacturing process.

In the future, FDM is anticipated to broaden the range of usable materials. Extensive research is currently focused on 4D printing, which refers to objects capable of performing active functions in response to changes in temperature, humidity, or electric fields [31]. As FDM is adopted by an increasing number of industries, its integration with conventional manufacturing techniques is expected to create a complementary relationship [34].

2.3.3.2 Hotpressing

Hotpressing is a type of post-processing method in which a composite part is placed in a closed mould and then placed in a heated press to eliminate voids and consolidate the part. The method is used in combination with FDM continuous fibre printing to deposit the fibres, regular FDM printing is unable to process the continuous fibre filaments such that they are consolidated when placed

which typically leaves voids and uncompacted fibres. Adding a hotpressing step can then re-process the part to reduce porosity from 10-30% to near zero (1.4%), which has been shown to increase the short beam shear strength by 410% [35].

The advantage of this method is to create parts of 60% fibre volume fraction (aerospace grade) with near zero porosity [35] using highly optimised fibre paths and compensates for poor processing in the deposition step. The disadvantage is the need for custom moulds for each part shape which not only adds an extra cost to different designs and limits the geometries that can be made to allow de-moulding.

In the past a combination of 3d printing and conventional manufacturing has been used. One technique is to lay the prepreg filament as done in regular FDM and then place it in a mold in the shape of the final part and hot press it. This technique has created parts of high strength and good surface finish but required shape dependent tooling and an extra step. Since this compromises one of the main advantages of fdm: the shaping freedom, this is critical to the manufacturing process.

2.3.3.3 Compaction Printing

Similarly to Automated Fibre Placement with In-Situ Consolidation: one method to reduce the porosity and increase the quality of the prints is to provide a consolidation pressure using a roller/-compactor that follows the nozzle to press the material perpendicular into the print bed [36, 37]. This method is able to introduce matrix pressure and compact the fibres using a heated tool, this shows a great improvement the strength and bending properties of the finished part and showing that the properties are comparable to hot-press post-processing (at 0.1MPa which is a low pressure for CFRP processing as shown in Figure 2.2b) [36].

The advantage of compaction printing is that the design freedom of FDM is almost fully utilized except for the inability to print overhangs and bridges as the deposited filament must be well supported when compacting. Another advantage is the low cost of this method compared to more conventional composite manufacturing methods. The parts produced using this method are able to steer fibres to small radii which increases the ability to steer and orient the fibres within the part.

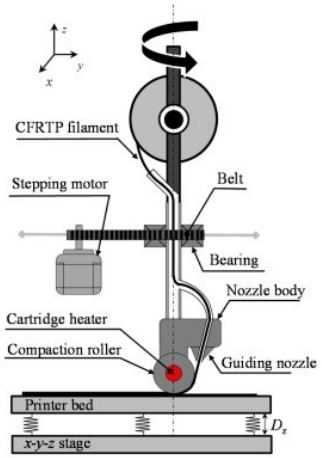

Figure 2.6: Compaction Printing [36]

The method that the paper established as "3 dimensional compaction printing" showed that the roller considerably reduced the porosity in the samples and had achieved strengths comparable to hot-press post processing a regularly FDM printed sample.

This roller adds an extra axis to the printer and makes the system more complex, so an article mentions an alternative way of compacting the material. This method consists of laying segments of laying paths and then using a hot tapered tool to compact it. The compacting end starts from the centre of the path and follows it to one and and then lifts and moves to the centre again and

compacts the path in the opposite direction [37]. The method was referred to as "Discrete In-situ Consolidation".

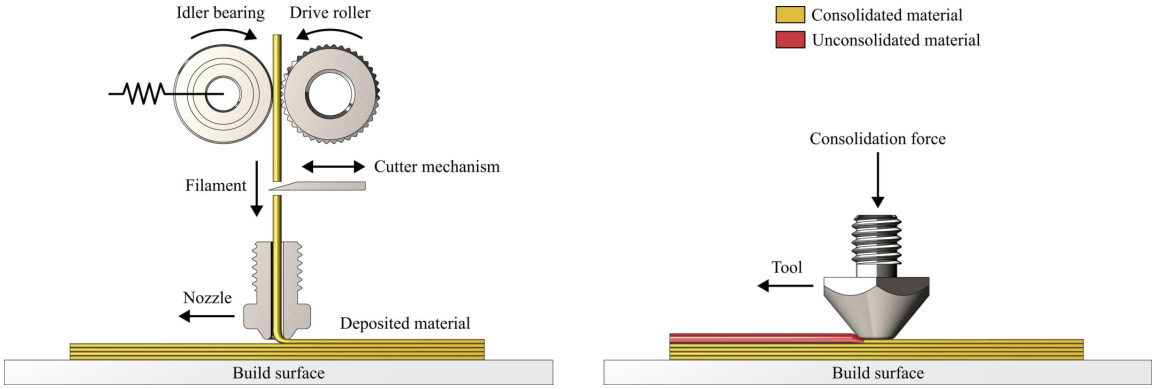

Figure 2.7: Discrete In-situ Consolidation [37]

Several companies are currently working to commercialise compaction printing, which makes detailed information about their printer designs and performance difficult to access. Patents have therefore been used to gain insight into the present state of the art in commercial compaction printing.

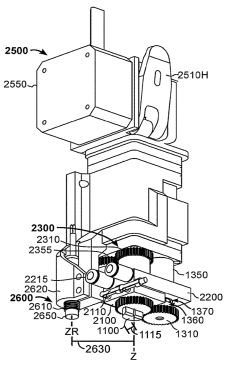

(a) Full 9T labs extruder

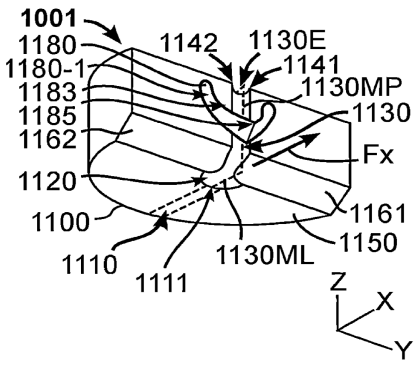

(b) Nozzle compactor that trails the deposited bead. The path is curved to avoid fibre damage and a flat is added to compact and spread the filament.

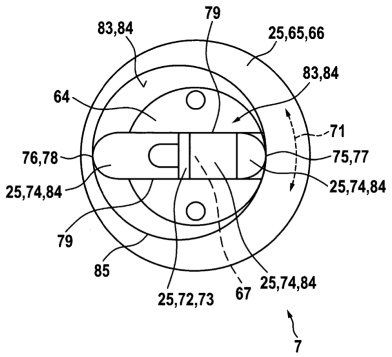

(c) Filament cutter that uses rotational motion in a cam to drive a blade through the filament

Figure 2.8: 9T labs printer[38, 39]

The 9T labs printer (Extruder in Figure 2.8 (a)) has a nozzle with a radii to avoid fibre damage and a flat section to iron the tape as it is begin laid shown in Figure 2.8 (b). This printer also has an unconventional filament cutter which uses a blade that is guided by a slot, the blade is pushed by an internal cam mechanism that converts the rotation from a servo into a linear motion that allows the blade to cut through the continuous carbon fibre filament, shown in Figure 2.8 (c).

The desktop metal printer appears more like an AFP machine than a printer as it is laying tapes instead of filaments, the printhead contains a roller to apply a consolidation force and it requires an additional rotation axis to spin the printing plane in-line with the printing direction. The printer shows 2 methods of heating: the first is to use a heat block that is placed adjacent to a tape as it is fed, conducting the heat into it, which is shown in Figure 2.9 (a). The second is a method that guides air through a heat sink to heat the air, the air is then fed to the nipping point under the tape to melt the section between the tape and the previous layer, shown in Figure 2.9 (b). This printer has the

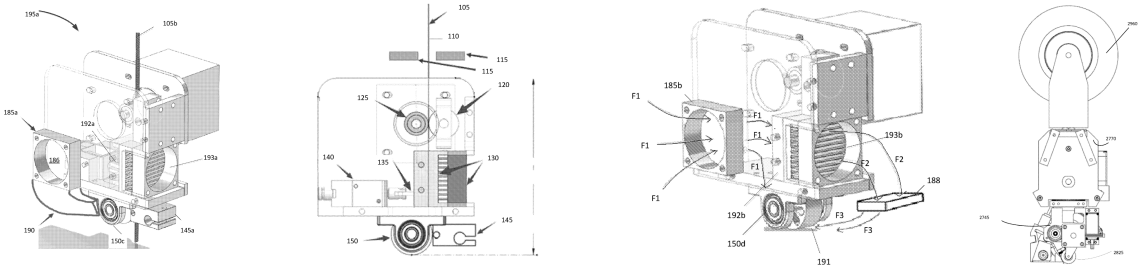

(a) Conduction heater

(b) Side view of conduction heater

(c) Hot gas heater

(d) Print head and material spool

Figure 2.9: Desktop metal printer, using a architecture similar to that of an AFP machine where the head deposits a tape that is heated then compressed using a roller[40]

spool of material placed on top of the printer to allow it to spin with the deposition tool to avoid tangling of the material on the spool.

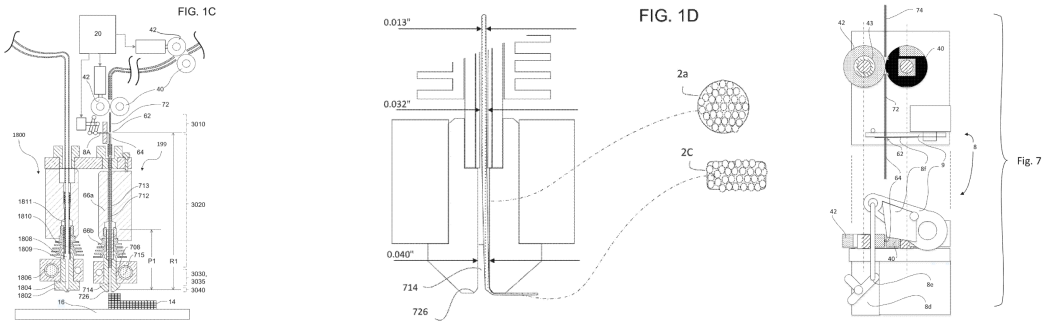

(a) Dual extruder left side deposits thermoplastic, right side deposits fibre reinforced thermoplastic.

(b) Continuos fibre nozzle cross-section showing the reshaping of the filament cross-section as it is deposited.

(c) Cutter placed after the extruder wheels with the blade placed on a mechanism that allows force multiplication.

Figure 2.10: Markforged printer, using a dual extruder concept with pre-impregnated fibre reinforced cylindrical filament and regular FDM filament[41, 42]

The mark forged is a dual extruder set-up with a thermoplastic extruder and a pre-impregnated continuous fibre extruder. This printer prints fibre volume fractions of around 34% which is low enough to allow a nozzle that is similar to that of a regular 3d printer. The nozzle has radii to avoid fibre damage as it is placed and a flat section on the bottom to iron it as it is placed.

The Anisoprint printer has a dual nozzle set-up, but this time the fibre and the thermoplastic are being impregnated in-line with the nozzle, making it need 3 extruders. The continuous fibre nozzle and an inlet of thermoplastic filament are combined to create a hot melt impregnation system within a heat-block that keeps the temperature above its melting temperature. The nozzle uses a radii to avoid fibre damage and also a flat section to iron it as it comes out.

2.3.3.4 Vacuum Printing

Vacuum printing is a variation on FDM printing with continuous fibre filaments that places the printer in a vacuum chamber. The vacuum chamber has been shown to have a beneficial effect on the quality of continuous fibre filament printing by reducing porosity in the final print.

The advantage of vacuum printing is that the method is straightforward and does not modify any processing steps or constraints of the manufacturing process. The drawback is that a vacuum chamber is costly and prevents any manual intervention during printing. It was shown that in PLA matrix composites the porosity volume could be reduced by 5.7% in carbon fibre, 1% in glass, and

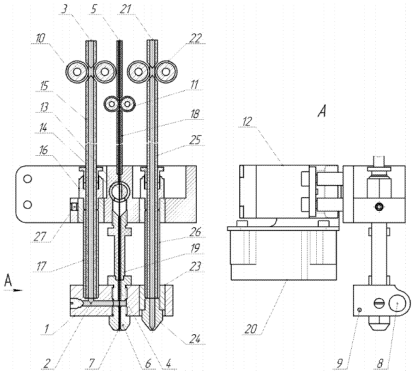

(a) Consonous fibre nozzle and thermoplastic nozzle placed in the same heat-block with in-line impregnation of the fibres.

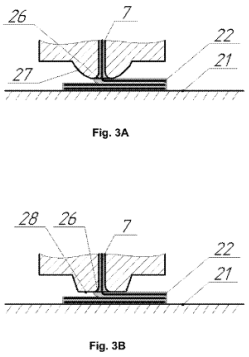

(b) Two different nozzle concepts used to deposit and compact the fibres.

Figure 2.11: Anisoprint printer, using a in-line impregnation concept with three materials from left to right: the matrix material for the impregnated fibres, the fibre material and the thermoplastic filament material that is directly deposited[43, 44]

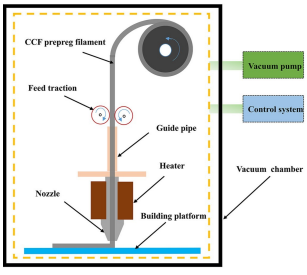

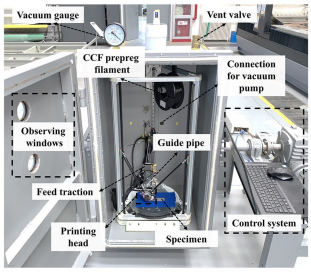

(a) Set-up for printing in a vacuum Li et al [45]

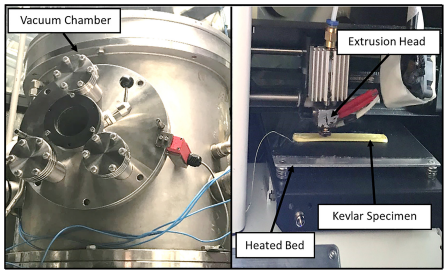

(b) Set-up for printing in a vacuum O'Connor et al [46]

Figure 2.12: Vacuum printing set-ups used to print continuous fibre using a modified FDM printer

1.7% in kevlar. This subsequently resulted in an increase in inter-laminar shear strength of 33%, 22% and 12% respectively [46], this was attributed to an increase in fibre-matrix bonding. In another article, some of the performance gains were partially attributed to the lack of convection in a vacuum environment, which would reduce the heat loss into the environment of the material that had been laid, allowing the material more time to diffuse between the boundaries of the layers [45].

Although vacuum printing did improve mechanical properties, claims made in Li's paper [45] indicate that a portion of the improvement may come from a variation in the heat transfer in the process. Since convection is no longer a viable way of transferring heat, the laid material is kept hotter for longer, which allows the polymer chains to be mobile for longer, which is already known to increase the mechanical properties of FDM.

2.3.3.5 Advanced Tape Layer Additive Manufacturing

In Advanced Tape Layer Additive Manufacturing, automated tape laying is integrated with large-scale additive manufacturing through a thermoplastic extrusion printhead fitted with a tape-laying unit that can be oriented in multiple directions. This allows the ATLAM machine to deposit thermoplastic substrate bead and then FRP pre-impregnated tapes are placed ontop compressing and heating the tape to fuse it to the substrate. CEAD BV's ATLAM machine can be seen in Figure 2.13.

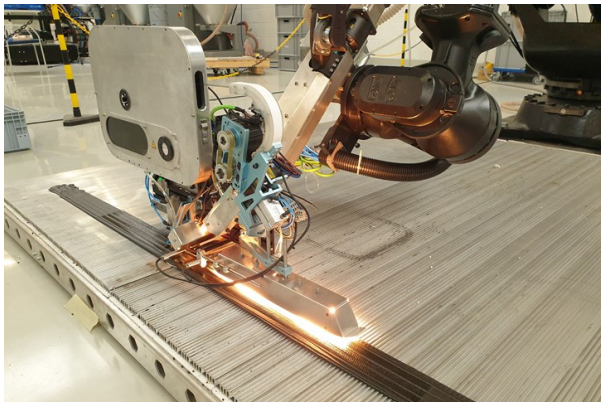

Figure 2.13: Advanced Tape Layer Additive Manufacturing [47]

ATL provides high structural performance, but the geometric freedom is limited, and significant tooling is required. AM has high geometric freedom and requires little tooling, but shows mediocre structural performance. ATLAM is a middle ground where the shortcomings of both methods are complemented to reduce the tooling needed, increase the geometric freedom compared to ATL, and increase the structural performance compared to AM.

In the design, it is possible to employ either pre-impregnated FRP tapes or a thermoplastic substrate. The two technologies are mutually supportive: the superior mechanical performance achieved through automated tape laying (ATL) can be integrated into additive manufacturing (AM), while AM can overcome the limited geometric flexibility of ATL. However, designing such components becomes more challenging and the combination of these two manufacturing approaches may give rise to new defects that have not yet been investigated.

The AM extruder employs a screw-based system to shear thermoplastic pellets containing short fibres, extruding them in a molten state through the nozzle as the print head moves, forming thermoplastic beads. Infrared heaters are used to heat both the tape and the substrate, generating a heated thermoplastic layer onto which a continuous fibre tape is fusion-welded [47]. Subsequently, a roller traverses the tape to compact it and promote strong bonding with the thermoplastic substrate.

Currently, ATLAM is mainly applied to manufacture moulds with low coefficients of thermal expansion (CTE), since the tapes exhibit a lower CTE, and their addition allows the substrate to

better retain its geometry at elevated temperatures [47]. Although ATLAM is used in some structural applications, the designs are not fully optimised and therefore do not realise the full potential of this manufacturing method.

To be viable as a structural design approach, the emphasis must shift from CTE to stiffness and strength. Using a multimaterial isotropic substrate together with an anisotropic tape will demand effective positioning and orientation of both materials, which in turn calls for a robust and high-performance design strategy.

2.4. Design of Continuous Fibres Thermoplastics Composites

In the design of continuous fibres thermoplastics composites the objective is to leverage the versatility of the manufacturing process to explore the design space and achieve solutions that exhibit high stiffness and strength. Because each manufacturing technique comes with its own limitations and advantages, only a customised design strategy can fully capitalise on these specific characteristics.

In design for manufacturing methods, essential requirements and limitations are integrated into the design workflow from the outset. This can involve, for example, applying a steering constraint for AFP or an overhang constraint for FDM. Introducing these constraints early on leads to more cost-efficient designs and minimises the amount of rework needed in later phases.

In conventional design practice, a component is developed primarily to meet structural demands, with little attention given to manufacturing aspects. Manufacturability is assessed only after the design has been finalised. Subsequently, the design may have to be altered to accommodate manufacturing limitations, which can result in diminished performance and increased cost.

Topology optimisation (TO) is a group of computational design approaches which determine how to distribute material most effectively within a defined domain. TO relies on knowledge of the specified loads and boundary conditions. In many cases, it outperforms conventional design methods because it is driven by performance criteria and can reveal solutions that are not immediately obvious.

2.4.1. Topology Optimisation

Topology optimisation is an optimisation approach that permits the insertion and removal of material within a domain, including the creation and elimination of holes. This capability lets it investigate a broader design space than conventional size or shape optimisation, uncovering non-intuitive configurations and supporting a high level of design automation.

Topology optimisation starts by specifying the design domain, boundary conditions, and applied loads. Then, the objective function and constraints are defined. Afterward, the domain is discretized, a mesh is generated, and an initial distribution is assigned to the mesh elements. A sensitivity analysis on the objective function is carried out for each element in the domain, and these results are used to adjust the local design variables (typically a element density) in a direction that moves the solution toward the objective function target. Once converged, in the final step, the optimised layout is post-processed according to a chosen manufacturing process to obtain a realisable design.

Topology optimisation strategies are typically grouped into density-based, level-set-based, and feature-mapping methods, depending on how they represent and update the material layout. In density-based approaches such as SIMP, the material is modelled using element-wise density variables that are treated as continuous design fields over the domain. Level-set-based approaches instead encode the structure implicitly via a level-set function, and optimisation proceeds by moving the material boundary rather than adjusting densities. Feature-mapping approaches describe the

design using explicit geometric primitives (such as beams or plates), optimising their dimensions, locations, and orientations. This categorisation reflects a progression from implicit to increasingly explicit geometry description and from less to greater direct control over manufacturability, moving from density-based to feature-mapping methods.

In density-based topology optimisation, the design domain is discretised into a mesh, with each element assigned a density variable. A gradient-based optimisation algorithm then iteratively adjusts these densities until a converged design is obtained. Although density-based methods are comparatively straightforward to implement, they may yield a non-binary density distribution if the penalisation is not chosen appropriately. In addition, the final layout typically requires post-processing to generate a CAD-compatible 3D model.

In level-set–based topology optimisation, the geometry is represented by a function defined in a higher-dimensional space, where the zero level set of this function defines the geometric boundary. The geometry is altered by changing this function. Level-set methods yield sharp interfaces between material and void; nevertheless, they are more difficult to implement, have limited capability to handle multiple constraints, and exhibit sensitivity to the initial design.

Feature-mapping topology optimisation methods can create manufacturing-aware structures that are explicitly constrained to manufacturable geometries. In these methods, a structure is built from geometric primitives, such as polygons, with design variables that include position, orientation, and dimensions. These design variables are then optimised to create the final structure. Although feature-mapping is a less general method, it typically requires less post-processing because the resulting geometries are composed of relatively simple primitives and clear boundaries.

This method is based on explicit features and is particularly well suited to automated tape laying (ATL), where the manufacturing process restricts the tapes to rectangular geometries. It operates with continuous tapes of constant width and thickness and allows only limited steering curvature. By directly matching the design variables with the constraints and capabilities of these manufacturing techniques, the method ensures that the resulting designs are directly manufacturable and do not require translation from a density map or contour-based description.

Out of all of the TO methods geometry projection topology optimisation is most suitable for our application. In this method, geometric features are mapped onto a fixed grid, eliminating the need to re-mesh the domain between iterations. A continuous parameter ranging from 0 to 1 is associated with the primitives to represent the effective density of each feature, similarly to the DTO methods. This technique preserves the computational advantages of density-based methods while imposing geometric constraints in a way that is comparable to feature-based TOs [48].

2.5. Geometry Projection Topology Optimisation Implementation for ATLAM

A GPTO computational design method has been previously implemented on the ATLAM manufacturing method by Chintan Jansari[49], the method has taken the following manufacturing constraints characteristic of ATLAM: each tape must lay on substrate or the tape will have no support, the tapes must not intersect as they are then thicker than the ATLAM methods allows to deposit the next layer, the minimum length tape relating to distance between the ATLAM tape cutter and roller otherwise proper tension cannot be added to the tape and accurate placement cannot be assured, the tapes placed can be varied in length but constrained in width by the width of the material used.

Implementing the shape constraints is done using rectangular features, the width of the rectangles being set to the width of a tape and the characteristic width of the substrate material. The tape rectangle is coupled to the substrate rectangle by defining them using the same position variables. The tape is defined by a starting point in a 2D Cartesian space $[x_{t1}, y_{t1}]$, an endpoint $[x_{t2}, y_{t2}]$ and a width, the substrate is defined as having the same mid axes line as the tape and 2 length variables $[L_{s1}, L_{s2}]$ that allow the substrate to vary in length from the start and end points of the tape as seen

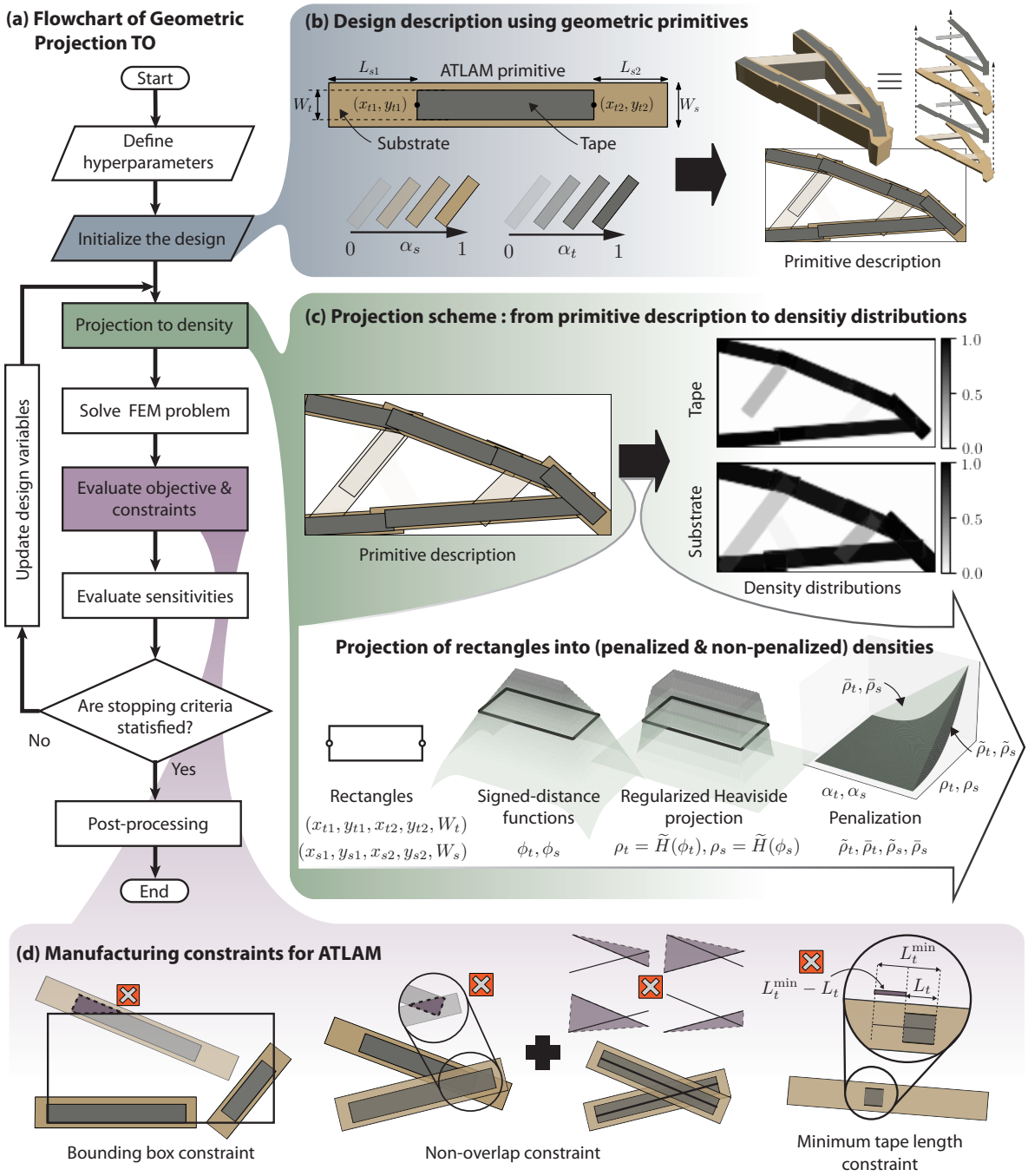

Figure 2.14: Geometric Projection Topology Optimization (GPTO) implementation for ATLAM.[49]

in Figure 2.14. As part of the GPTO method both the tape and the substrate are assigned a density $[\alpha_t, \alpha_s]$ that allows tapes and substrates to be removed as the design space is explored.

The rest of the manufacturing constraints are implemented using the following numerical constraints: the tape minimum length constraint, the straddling tapes constraint, and the bounding box. The tape minimum length constraint limits the use of tapes below a set length. The straddling tapes constraint ensures that overlapping tapes have the tape density capped at 1, an additional penalisation is added based on the volume of the 4 triangles formed by a tape mid-axes intersection. Each triangle is composed of the quadrilateral formed by the endpoints of each tape mid-axes line which is then separated by both mid-axes. The lowest of the volumes is used to penalise the tape intersection. This is used to create a negative gradient in the direction that will not cause a larger intersecting volume. The bounding box constraint limits the tape volume placed outside of the domain.

Two more constraints are used to explore the design space, a volume fraction constraint and a sustainability constraint. The volume constraint sets the maximum allowable space in the domain filled by tape or substrate as a ratio to the domain. The sustainability constraint will calculate the structure's embodied CO_2 then limit it to a value on a linear scale from the minimum which is calculated as a design which is made fully from substrate and the maximum which is a structure made from equal parts substrate as tape both fill the volume in the domain up to the volume constraint.

The input of the algorithm is the material properties are required in the calculation of the compliance and embodied CO_2, therefore the elastic properties and embodied CO_2 of the substrate and the tape are requisite in the initialisation. In addition a domain, loads, and boundary conditions are used to generate a design. Finally, 2 design choices must be made to set the allowable volume fraction and the environmental impact constraint.

The output of the algorithm is then an optimised design composed of tapes and substrates with positions in the domain. The positions are then exported as a list of endpoints, each rectangle mid-axes with an x, y location in the domain. The compliance and embodied CO_2 is also calculated to show the performance and sustainability of the design.

3

Research Definition

This thesis will focus on 2 aspects:

- Manufacturing tape reinforced fused filament fabricated structures
- Experimental validation of Geometric Projection Topology Optimization

3.1. Knowledge Gap

ATL enables components with a high stiffness-to-weight ratio, but its manufacturing limitations lead to considerable inefficiencies in both design and production. ATLAM can overcome many of these manufacturing constraints; however, GPTO is required to fully unlock the capabilities of this fabrication approach. A GPTO framework has been developed specifically for ATLAM's constraints and additionally allows the eco-efficiency of the structure to be imposed as a design constraint. Because ATLAM is a new process, the structural configurations it makes possible have not yet been experimentally validated.

The large scale of these structures makes testing both challenging and costly. There is a need for methods that can rapidly produce these structures so they can be tested, and the resulting data can be fed back into the GPTO algorithm to refine it for the types of structures ATLAM plans to develop in the future.

3.2. Research Objective

Research Objective - Scaled Automated Tape Layer Additive Manufacturing

To produce 200–400 mm (Largest Dimension) fibre-reinforced additively manufactured structures that function as a prototyping approach for advancing the design and testing capabilities of future ATLAM components.

3.3. Research Question

First a new manufacturing method is created to accelerate the development cycle. The method will be successful if it cuts the time and cost of manufacturing and testing compared to regular ATLAM.

Research Question 1 - Tape Reinforced Structure Manufacturing

RQ1.1 How can scaled Advanced Tape Layer Additive Manufacturing architectures be produced with a conventional desktop 3D printer?
RQ1.2 Does the inclusion of continuous fibre-reinforced tapes provide measurable mechanical reinforcement to the additively manufactured thermoplastic substrate?

Then the model used in the computational design methods must be validated with the structures that are manufactured and experimentally tested.

Research Question 2 - Structural Model

RQ2.1 Do the numerical models accurately reproduce the experimentally measured stiffness of the Geometrically Projected Topology-Optimised structures designed for ATLAM?
RQ2.2 Does the local strain field obtained from Digital Image Correlation align qualitatively and quantitatively with the predictions of the finite element model?

Finally the GPTO implementation will be compared to existing methods by its relevance to the aerospace industry and its ability to create eco-efficient structures.

Research Question 3 - Design Methods

RQ3.1 How does the structural efficiency of GPTO compare to that of conventional density-based topology optimisation approaches?
RQ3.2 How does the stiffness of the GPTO optimised design compare to that of its unoptimised initial configuration?
RQ3.3 How does the structural performance of the tape-reinforced GPTO design compare to the geometrically equivalent isotropic unreinforced substrate design?
RQ3.4 How does the stiffness-to-embodied-CO_2 ratio achieved by GPTO compare to that of established industry-standard topology optimisation methods?

4

Scaled Advanced Tape Layer Additive Manufacturing

The ATLAM process has typically been applied to manufacture moulds and tooling and is now being developed to create structural parts. ATLAM printer developed by CEAD B.V. is a large-scale printer, manufacturing structures with the characteristic dimensions in the range of 1-10 m. With such a large scale, printing cycles are expensive and time-consuming. In addition, mechanical testing of large structures is also logistically challenging. Therefore, we need a small-scale printing and testing workflow to experimentally validate of our propose design method. This has limited ATLAM adoption for structural purposes. In this chapter, we aim to develop an in-house desktop-scale version of ATLAM process and utilized it to print optimised design given by our topology optimization-based design method. A 400-200mm scaled version of the ATLAM manufacturing process would allow the use of universal force testing machines for characterisation, and would also require less material used to be in the process.

4.1. Desktop Scale ATLAM Work Flow

Designing a process to mimic ATLAM begins with separating its two simultaneous steps: additively laying substrate material and automated tape laying. In the original ATLAM process, a molten bead of thermoplastic is laid additively from a screw extruder mounted on a robot arm, and then, a carbon fibre reinforced prepreg tape is deposited and fusion-bonded on top of the substrate layer under applied heat and pressure. Then, these steps are repeated layer-by-layer to manufacture an entire structure. The standard ATLAM process is illustrated in Figure 4.1.

The ATLAM process uses a screw extruder to additively lay substrate material as shown in Figure 4.2a. This has the advantage of using thermoplastic pellets which are cheaper and do not require as high shape fidelity as FDM filaments. The screw extruder feeds have pellets to an inlet, and the pellets are sheared and heated by the motorised screw into a nozzle. The nozzle flows out the molten thermoplastic before it solidifies into an extrudate as shown in Figure 4.2a. This additively laying of substrate material can be replicated at a 400mm-200mm scale by conventional FDM printing, where a circular profile filament spool is used instead of pellets. The FDM printer used for the substrate material is the Prusa XL, a commercial off-the-shelf 3D printer. There are 3 main reasons for choosing the Prusa XL: the larger printbed (360mmx360mm), the multiple toolheads that allow for multi material prints and the detachable toolhead design would allow for additional modularity and ease in handling.

The second step in ATLAM process is laying and fusion bonding of tapes on top of the substrate layer as shown in Figure 4.2b. This step involved mainly five tasks: heating of previous layer of substrate, feeding and heating of tapes, placing of tapes, cutting of tapes, and applying pressure using consolidation roller on top of the tape. In our workflow, we simplify these tasks into two tasks, manually cut and place tapes, and fusion weld the tapes using soldering. The tapes are manually cut from the spool using scissors and positioned on the substrate layer. In order to place the tapes precisely in the desired locations and minimise the placement inaccuracies, we keep the rectangular recessed pockets of 0.2mm depth while printing substrate material. Once the tapes are placed in

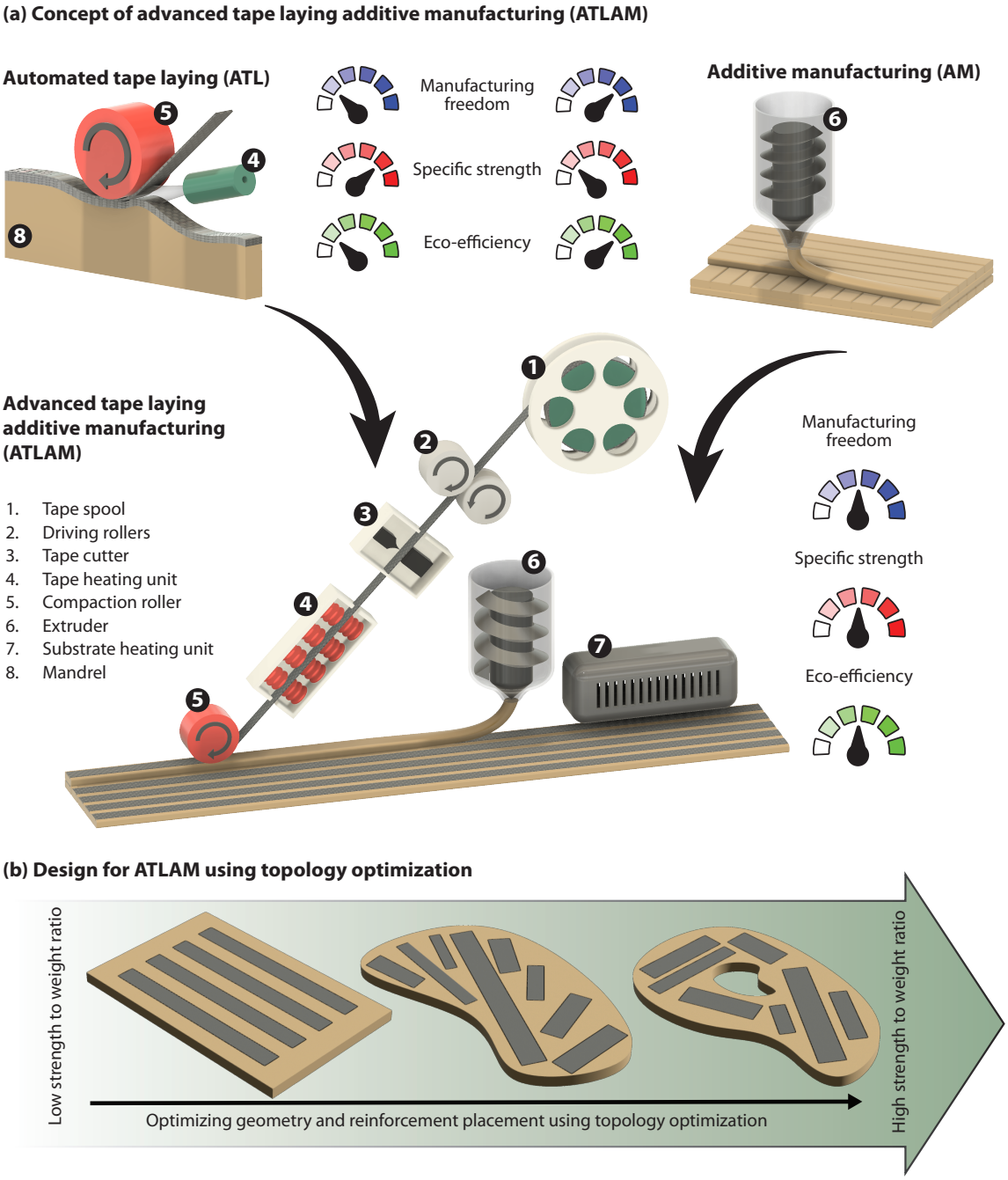

Figure 4.1: Advanced Tape Layer Additive Manufacturing (ATLAM) designs (Taken from [49])

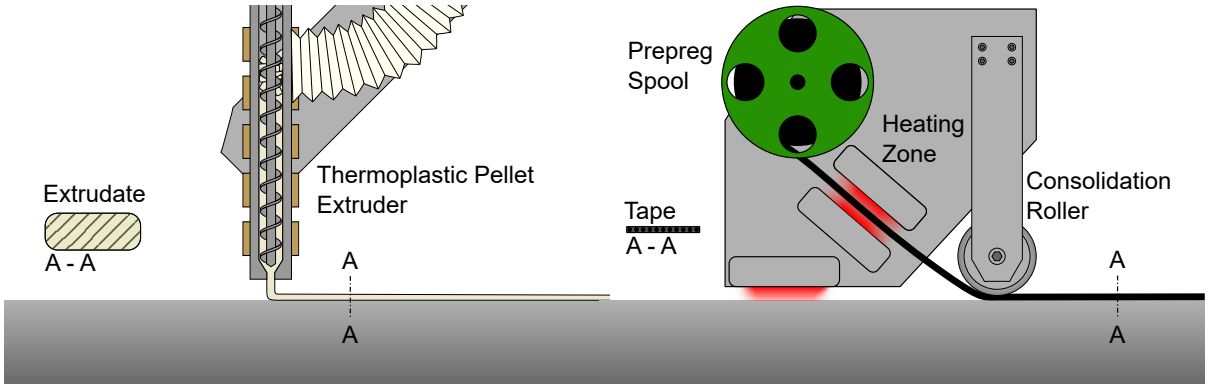

(a) Additive manufacturing thermoplastic pellet extruder with cross-section of the extrudate formed in the process

(b) Automated tape laying method with associated laid tape cross-section shown

Figure 4.2: AM and ATL methods which compose the combined method known as Advanced Tape Layer Additive Manufacturing (ATLAM)

these pockets, they are fused on the substrate layer using thermoplastic fusion welding. The welding process heats the tape and the substrate surface below it. Then, the pressure applied through the tool head bonds both surfaces. We choose manual fusion welding, as it fundamentally creates a fusion bond similar to ATLAM's tape laying. Please note that the manual tape laying has a limited manufacturing accuracy compared to ATLAM because ATLAM's tape laying is a continuous and highly automated process.

As illustrated in Figure 4.3, the process starts with depositing the substrate, leaving a pocket recess in the shape of the tape. The print is then paused between steps a and b to allow the tape to be placed using the pocket as a guide. In step c, the tape is bonded to the underlying substrate from above, and finally, in step d, printing resumes to encapsulate the tape within the substrate material.

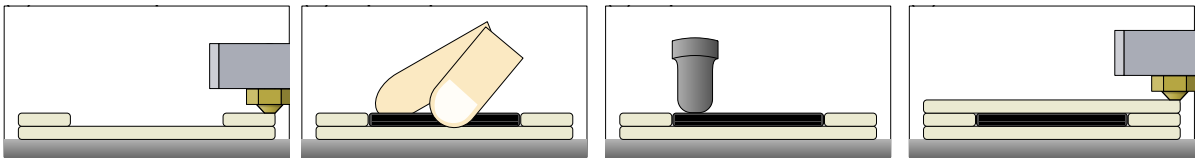

(a) Pocket is printed **(b)** Tape is placed **(c)** Tape is welded **(d)** Print continues

Figure 4.3: Scaled Advanced Tape Layer Additive manufacturing concept

(a) Prusa XL **(b)** Toolhead Nextruder

Figure 4.4: FDM printer Prusa XL with 5 toolheads and extruder toolhead Nextruder

Additional Information - Prusa XL, Fused Deposition Modelling Printer

The Prusa XL (refer to Figure 4.4 (a)) is a printer with multiple toolheads (refer to Figure 4.4 (b)), which allows all the tools to be loaded with different filaments and operate at differing temperatures during the same print. The toolheads are picked up by a core $x-y$ gantry driven by belts that is fixed at the top, and can move on a plane parallel to the ground. The print bed can move vertically with two lead screws that run along the side of the printer. All axis are controlled by stepper motors using displacement control. The initial position of the $x-y$ plane is found using sensor-less homing. Sensor-less homing moves the toolhead into a corner of the printer until it collides with the end of the rail, this stalls the motor which the control board can be detected through the back EMF to calibrate the zero position. The z axis is calibrated by using an on-board strain gauge, which turns the nozzle into a vertical load cell. The nozzle is slowly pressed into the print bed in a grid pattern to create a z-zero surface along the $x-y$ plane. This method ensures that the first layer is always deposited at a known distance from the printbed.

4.2. Manual Tape Welding

For fusion welding of tapes, we explore two methods, both of which induce local heating in the material to allow thermoplastic fusion at the interface. The first method is thermal conduction welding and the second is ultrasonic welding, the welding tools utilized in both methods are presented in Figure 4.5. The thermal conduction welding tool is a soldering iron with a 5mm blade cartridge used to spread the heat over a larger surface area. The ultrasonic welding tool is a transducer with a rounded 10mm tip used to transfer mechanical energy.

(a) Conduction heating welding tool **(b)** Ultrasonic welding tool

Figure 4.5: Manual welding tools used to adhere the tape onto the substrate

Preliminary experiments were performed to confirm the ability of forming a suitable bond between continous carbon fibre thermoplastic pre-preg and 3D printed polymer substrates using the proposed manual welding methods. The initial thermal conduction welding tests, performed at 300°C, showed severe fibre damage with undulations in the fibre alignment as shown Figure 4.6a.

At first, PLA is used to print a substrate layer, PLA was used for its low cost, accessibility and simplicity of printing. Then, a tape is bonded on this substrate layer using thermal conduction welding. Following this, the next layer of PLA is printed on top. However, as can be observed from Figure 4.6b, the next layer of PLA fails to bond effectively on the tape surface. The main reason behind the poor quality of this fusion bond can be given as PLA printed at 215°C could not transfer sufficient heat to the underlying layer to generate adequate chain mobility in the PA12 matrix of the tape to achieve a fusion bond. Given that PA12 has a melting temperature of about 260°C and a processing temper-

(a) Tape fibres damaged and misaligned after thermal conduction welding

(b) Poorly adhered PLA on the top surface of the CFRP tape

Figure 4.6: Initial welding tests using polylactic acid (PLA) filament

ature near 285°C, the tape and substrate must have comparable processing temperatures for this approach to be feasible.

To ensure compatibility, the substrate material was switched to ePa12, which has a processing temperature of 285 degrees. During the second round of printing, this filament bonded to the layer above the tape, allowing the tape to be fully encapsulated by the substrate. Given that the tapes could be deposited, welded and then printed over, the structures could now be manufactured. The next step was to identify the best welding technique.

Next, we compare both welding techniques; in order to do so, both welding techniques were employed to fabricate double lap shear samples, these samples are then subjected to tensile testing to compare their failure strengths. Because the tapes can only be welded from the top, each sample was produced in two symmetric parts before joining them using a cyanoacrylate adhesive. Also, while manufacturing each part, a Kapton tape was added between tape and substrate before welding to protect the fibres and keep them aligned. This process with a sample and testing setup is illustrated in Figure 4.7. The bonds are colour-coded to indicate their positions within the experiment. In this process, adhesive is used to keep the sample together until the clamping pressure is added, whereupon the sample is then held by friction. The top half uses a spacer made from ePa that keeps the tapes aligned as the clamping pressure deforms the substrate.

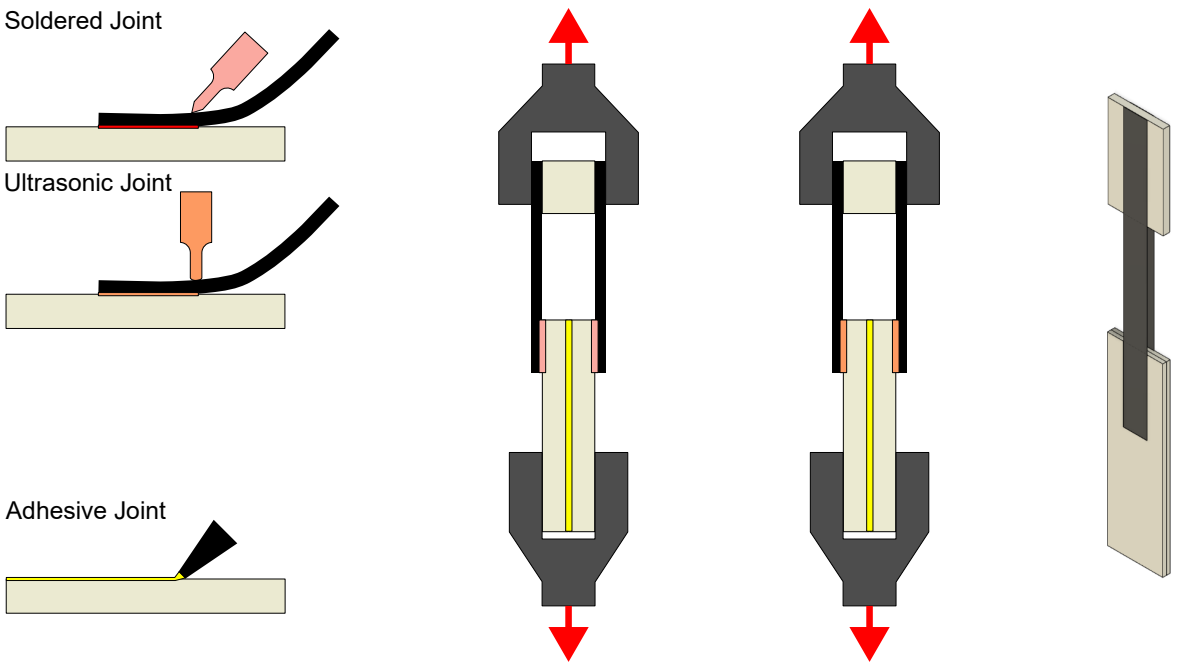

Figure 4.7: Double lap shear of soldered and ultrasonic joint for characterization

The double-lap shear samples are shown in Figure 4.8. We can observe that the fabrication qual-

ity of thermal conduction welding outperforms ultrasonic welding visually. Notably, the utrasonic-welded samples exhibit fibre distortion at the tape ends.

(a) Thermal conduction welded samples

(b) Ultrasonic welded samples

Figure 4.8: Double lap shear joint photos

The double lap-shear samples were then tested on a 250kN Zwick force testing machine using the cross-head displacement and an in-line 250kN load cell. The samples were placed with the welded sections on the underside of the tape and the upper section of the tape clamped. This set-up was intended to load the lower interface but use friction to keep the upper interface together, whereupon the failure force would then indicate the strength of the joint. The results are presented Figure 4.9.

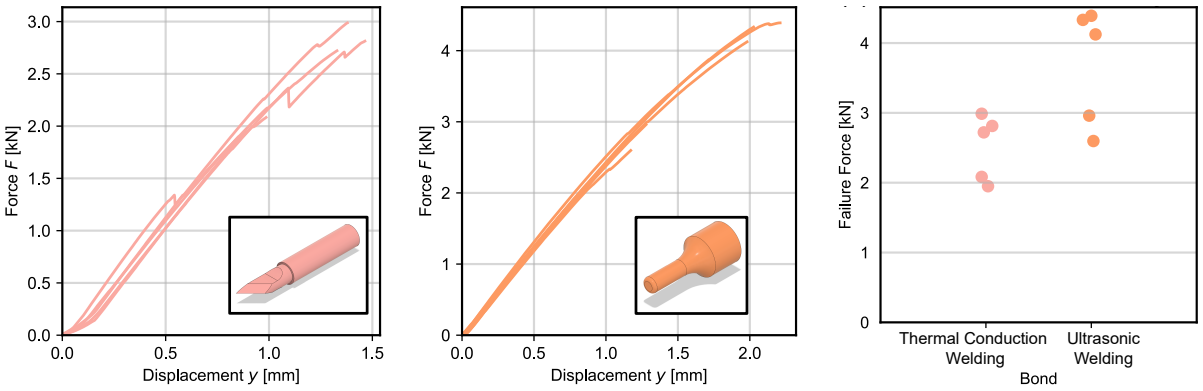

(a) Force-deflection of 5 thermal conduction welded double lap shear samples

(b) Force-deflection of 5 ultrasonic welded double lap shear samples

(c) Failure force for each weld type

Figure 4.9: Force displacement graphs of double lap shear tests of ePa12 and CF-Pa Tape interface with associated failure force

The manufacturing of the double-lap shear samples revealed that the manual welding is time intensive; for instance, welding a 40 mm strip requires approximately 15 minutes. Therefore, a design with 1000 mm tape-length will require over 6 hours for welding. This poses a stringent time constraints for manufacturing in the available time frame.

In addition, the welding process is performed by considering a steel build plate (which had been heated to 100 °C from the printing process) off the heat bed. By removing the build plate, we allow the plate to cool, which produces a thermal expansion mismatch between the build plate and the first substrate layer. For larger components (200 mm or longer), this mismatch causes the separation between the first layer and the build plate. Once the initial layer is detached, the part can no longer stay accurately positioned during printing, resulting in a layer shift defect. Consequently, welding

must be performed with the build plate kept on the heat bed at 100 °C.

Altogether, this makes the hand welding of tapes unfeasible for large or high-volume samples. Therefore, we need an automated welding approach that allows the substrate to stay on the heated bed whilst welding as well as enhances the welding speed and accuracy.

4.3. Automated Tape Welding

The Prusa XL comes with all the components needed to fully automate the welding process. The printer's heatblock can be adapted to heat a tape-welding tool, while the printer's firmware can be utilized for both precise positioning and temperature regulation. Therefore, we design a compactor tool that fits within the thread used by a standard nozzle. The compactor tool is shown in Figure 4.10.

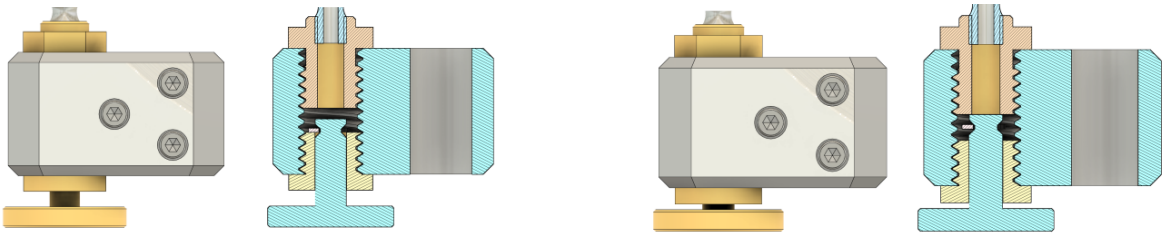

(a) Extended position tape compactor tool with a section view at the mid-plane

(b) Retracted position tape compactor tool with a section view at the mid-plane

Figure 4.10: In-house tape compactor tool showing extended and retracted position inside the Prusa XL heatblock. Showing the ability to retract to compensate for surface irregularities.

This tool is designed to ensure contact with the top surface of the tape, allowing the compactor to transfer enough heat transfer to melt the matrix of both the tape and the substrate at the interface. The vertical movement would follow the surface and the gantry would allow for consistent compacting speed and accurate placement of the tool. In addition, we can vary several of the process parameters including the speed of the compaction tool and the temperature of the tool using the original printer control settings.

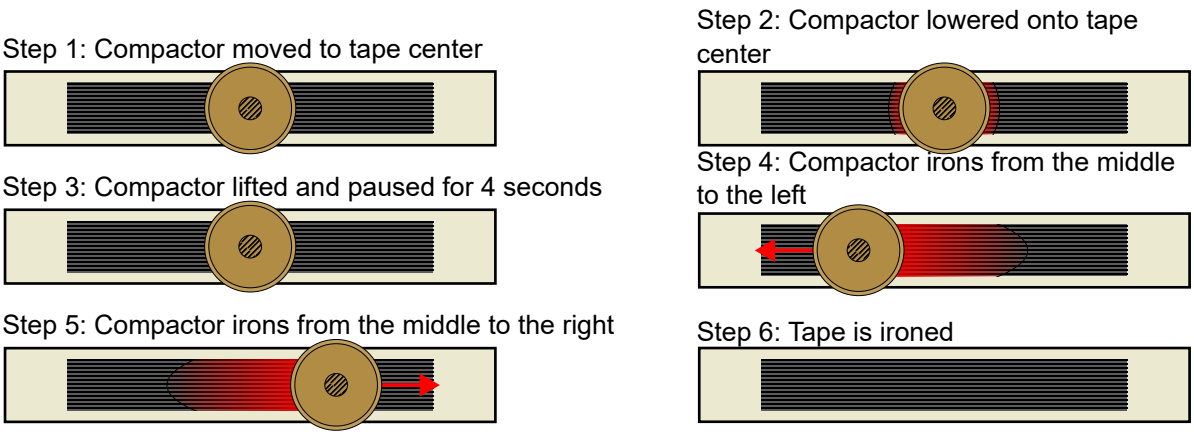

Figure 4.11: Tape compaction sequence used to weld tapes to the substrate below. Compactor tool shown from above, with red trails when heat is being transferred to the tape.

The automated tape welding follows a similar process as the hand welding: the print is paused, tapes are cut to length, and placed into the pockets that are left by the print and then compacted with the tool to fuse them in place. The compactor pathing and welding process takes inspiration from Elderfield et al. on discrete in situ consolidation [37] where a printer-mounted tool was used to consolidate extrudates of continuos fibre-reinforced filament. The tool pathing would take a

lengthwise outward path from the middle of the tape in two strokes, one in each direction. This sequence allows the tool friction on the tapes to keep the fibres in line with the placed fibre direction. As the lengthwise strokes can shift the tape as it compacts, so an additional step was added to spot weld the tape in place (seen in Figure 4.11 Step (1-3)). The compactor tool would place itself above the centre of the tape, press the middle tape from above at 280°C and raise again, allowing some time for the solidification of the matrix. This would attach the matrix of the tape in the middle without moving it. The time of compaction and the time allowed for the matrix to solidify was critical. If the compaction time was too low, the tape would melt but the substrate below would not, and this would instead attach the tape to the tool. If the time allowed for solidification was too low, then the tape would once again move with the compactor as it irons because the interface would still be molten. During the compaction, the speed of the tool was also tuned as it was found that if the tool was too fast, the tape would not heat in time and would begin to split edgeways under the force from the compactor. The final compaction sequence can be seen in Figure 4.11.

Given that the compactor is rounded and the tapes are rectangular, the compactor is designed to run over the side of the tape to ensure that the whole top surface is properly compacted. In some designs, there are small overlaps of the tooling path and an adjacent tape. These overlaps combined with the need to run over the sides of the tape caused the compactor path to collide with the adjacent tape. The adjacent tape would create a small height step from the the substrate to the top of the tape which would push the compactor onto the side of the tape, resulting in a movement or wrinkle of the tape. Instead, the tapes were placed and compacted one by one, making sure the compactor was only on the topmost tape in an overlap and avoiding situations where a tape is moved after it is placed.

The paths of the compactor were added to the slicer as a g-code at the end of each layer with tapes on it. The code would be generated for every design using the script shown in Appendix A. The code would also list the lengths of tape to cut and in what order to place them. Pauses would be added to the code with the tape number to keep track of the tape being placed on large designs. The code is explained in Figure 4.12, a layer of tapes will start with parking the current tool and picking up the tool with the compactor installed. Then, for each tape in the layer a pause is added that will show a message on the screen to indicate the tape number being placed, the tape is stamped in the centre, welded and then the tool is moved to the top right of the working space to allow the manual placement of the next tape. Once the step is repeated for all tapes the tool with the compactor is parked and the print is resumed. The code uses move commands at 2 speeds, sp1 is the travel speed of the tool and sp2 is the welding traversal speed.

The Prusa XL printer firmware is not designed to have tools that do not deposit material, therefore there were several variations that were made to the printer set-up gcode that is automatically added by the PrusaSlicer software. When an object is sliced, the tools are made ready according to the volume of filament that is used from each respective tool. In our method this would leave the compactor tool depositing $0mm^3$ the software would then disable the tool. Then, during the printing process the printer would stop and raise an error when it reaches the line that picks up the compactor tool. To solve this a extra volume was added on top of any object printed, this object was assigned to be "printed" with the compactor tool. This would allow the use of the compactor tool and since it is placed at a z layer higher than the print, the print could be stopped before it ever reached that portion of gcode. In Figure 4.13a, an example print is shown where a cylinder is added of fictitious compactor tool material to allow the printer to use the compactor tool.

Another process performed before the printing begins is the creation of a z level mesh and the wiping and priming of all the tools. The creation of a z level mesh is a process where the z height of the print bed is probed at multiple different points in order to create a mesh that allows the first layer to be placed accurately along the surface. This process is performed using a load cell in the tool to detect a collision with the printbed. The Prusa XL uses the known distance between the tip of the nozzle and the tool holder to set the z height. It is therefore important, due to the difference

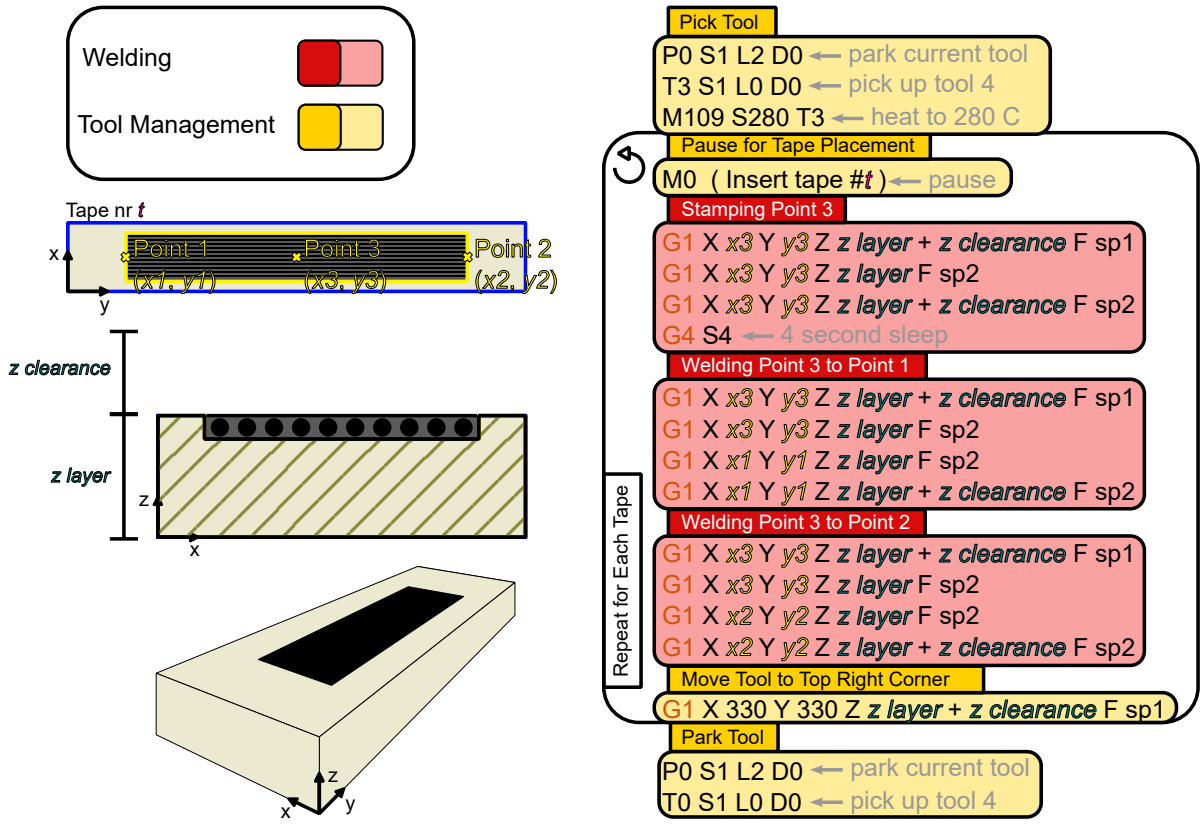

Figure 4.12: Tape welding g-code added at each layer with tapes

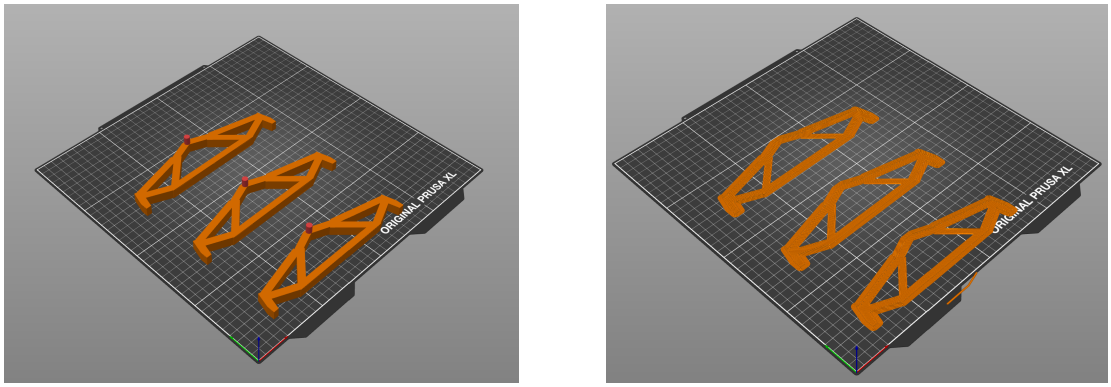

(a) Model before slicing showing the assignment of a fictitious volume that is set to the compactor tool in red

(b) First layer showing the wiping function at the bottom of the print bed

Figure 4.13: PrusaSlicer screenshots showing the assignment of the compactor tool volume and the wiping function

in height between the compactor tool and the nozzle, to perform this process with a tool that has a nozzle installed and not the compactor tool. Finally, in each print the tools must be primed and wiped to get the nozzle up to printing pressure and avoid oozing in the print. This is not needed in the compactor tool and could cause a collision with the print bed so that step is removed.

4.4. Chapter Summary

This chapter focuses on creating an in-house desktop-scale ATLAM workflow. The ATLAM process is broken down and analysed to choose alternative processes for tape laying that could work at a 400mm-200mm scale to create tape-reinforced structures. The manufacturing methods chosen to replicate these structures are FDM for the substrate and manual tape deposition and welding. The next section shows initial tests using this method and finds PLA is not suitable for this method, the substrate material is switched to ePa12 which prints over the tape without defects and manual tape welding is found too time intensive for larger structures. The need for a fast and more accurate welding method then drive the design of a printer mounted tool that can weld the tapes using thermal conduction welding. The pathing and process of the printer mounted tool is explained and the results from initial tests are used to develop the processing parameters.

The next chapter will focus on the use of the proposed workflow to manufacture test designs to benchmark their performance.

5

Experimental Validation of Geometric Projection Topology Optimisation for ATLAM

This chapter describes how the desktop ATLAM workflow is employed to develop and validate our topology-optimisation-based design method. The validation approach is outlined in Section 5.1, followed by the material characterisation required for the TO method in Section 5.2. The resulting material data is then used in our design method to achieve optimised structures for a test case in Section 5.3. Subsequently, these optimised structures are manufactured and tested as detailed in Section 5.4. The chapter is then concluded with a summary of the key findings.

5.1. Validation Method

The desktop ATLAM workflow was developed to allow experimental validation of the design methods for ATLAM. Experimental validation is key to ensure that manufacturing constraints are being respected in the designs and ensure the fidelity of a numerical approach and its subsequent real-world applicability.

In literature, topology optimisation methods are typically compared using benchmark load cases, these cases are sets of pre-described domains, loads, and boundary conditions that outline a design problem. The TO method is applied to the load case and the compliance or the displacement of the loading point is used to compare the performance to other TO methods. A similar approach can be used to validate the TO methods in this thesis, a load case is chosen, multiple methods are applied to the same load-case and the compliance is found experimentally.

The MMB Beam benchmark load-case is chosen as it can be tested by three point bending testing. A three-point bending configuration can be realised on a universal testing machine without the need for clamping supports, which are often challenging to implement.

Another design that is tested is the ground design for GPTO, in the GPTO algorithm this serves as the initial guess before the optimiser begins to iterate on the design. This will give another data point to validate the FEA model and allow insight into the performance of the optimiser within the constraints of the GPTO method.

5.2. Material Characterization

TO methods require the mechanical properties of the material to calculate the compliance, and therefore the sensitivity study of the compliance. Due to the process dependence of the material properties of FDM, the material was characterised in-house. The tapes would also be tested in house due to the lack of data available on the material properties.

In the finite element model of the TO algorithms, the substrate material is assumed to be isotropic and linear elastic. Therefore the material properties required to model the substrate are therefore the elastic modulus and the poison ratio.

Typically, the ASTM D0638 standard is used to find the elastic modulus for polymers using a tensile test. The standard is used to determine the shape of the ePa12 sample coupons. Accordingly,

the samples are printed using an ePa12 filament with a layer height of 0.2mm and a rectilinear infill of 100%. The printed samples are shown in Figure 5.1.

Since ePa12 is hygroscopic (it tends to absorb water molecules when exposed to ambient humidity) and this moisture trapped in the polymer can expand during printing as it is heated creating voids, which significantly affects the mechanical properties, the ePa12 filament is dried in a vacuum oven at 70°C for 12 h as specified in technical datasheet. Then placed in a heated dry box at 65°C to prevent it from absorbing moisture during printing. The samples are printed with a nozzle temperature of 285°C with the bed at 100°C. A brim of 5 mm is used to stop the warping of the print. Then, the prints are de-burred to remove the brim and stringing.

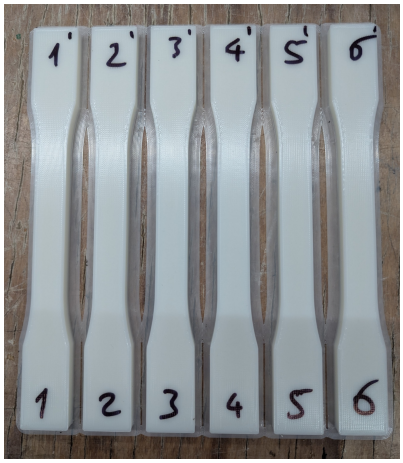

(a) Printed ePa12 as per ASTM D0638 [6 printed samples]

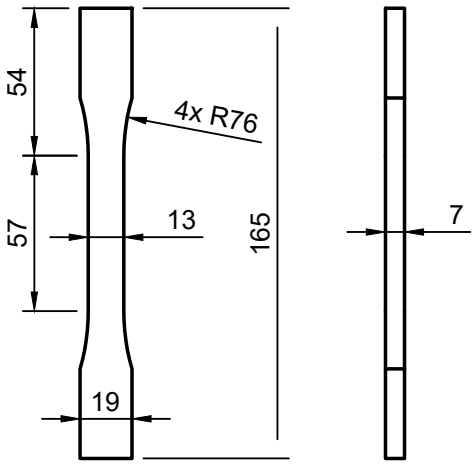

(b) ASTM D0638 drawing standard for polymer tensile testing for mechanical characterisation

Figure 5.1: Printed samples and ASTM D0638 tensile testing standard

The samples are placed in clamps on a Zwick 20kN universal static testing machine, seen in Figure 5.2. With an in-line 20kN load cell above to measure the force and an extensometer is placed on the gauge length of 57mm to obtain accurate displacement data.

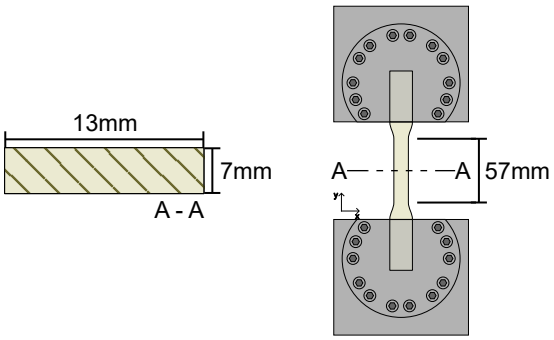

Figure 5.2: Test set-up printed ePa12 filament printed samples, A-A shows the cross-section of the sample at the gauge length which is used in calculations

When testing, the sample is preloaded with 5N to remove slack and align the sample. The force from the Zwick and the extension from the extensometer are then converted to engineering stress and strain using the actual gauge area cross-section length and width measured before testing using a calliper. The results, shown in Figure 5.3 (a), show consistent mechanical properties between the 6 samples. The samples show ductile failure with a large linear region.

Linear regression is used on the initial linear portion of the stress-strain graph to find the elastic

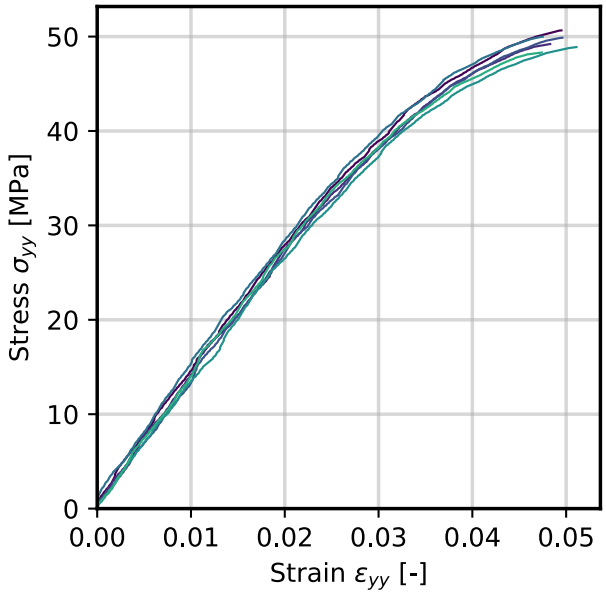

Figure 5.3: ePa12 stress-strain graph for tensile test [6 printed samples]

Property	Symbol	Value	Source
Elastic Modulus	E	1440 MPa	Measured
Failure Strength	σ_{st}	49.5 MPa	Measured
Poisson Ratio	ν	0.403	matweb
Shear Modulus	G	514 MPa	Calculated
Density	ρ	0.998 g/cm^3	Measured
Embodied CO2	I	4.610 kgCO_2/kg	[49]

Table 5.1: ePa12 Printed Filament Properties

modulus of every sample, and then values are averaged to get the average elastic modulus of the material. The failure strength is determined by the highest stress achieved in each sample, and then the average is taken between the samples. The Poisson ratio is found from the matweb material database. The shear modulus in Table 5.1 is calculated using the formula for the shear modulus in isotropic materials seen in Equation 5.1.

$$E = 2G(1+\nu) \tag{5.1}$$

The tape properties are also required for the TO FEA, the fibre reinforced tape is assumed linear orthotropic and therefore requires 4 independent material properties, E_1, E_2, G_{12}, ν_{12} to fully characterise. The CFRP tapes available for this project are 62% standard modulus carbon pre-impregnated fibres with a cross-section of a 0.17x12.7mm rectangle. The matrix material is Polyamide 12 (Nylon 12, Pa 12).

Typically in literature, the material properties of a UD Carbon FRP tape would be obtained by consolidating the pre-preg into a laminate and then testing the laminate. Since the end use of the tape would not be a laminate and there were no methods available to consolidate a laminate, the mechanical testing would be performed directly on the tape. A tensile test would be performed in the fibre direction as seen in Figure 5.4 to find E_x and ν_{12}, the rest of the values would be taken from literature.

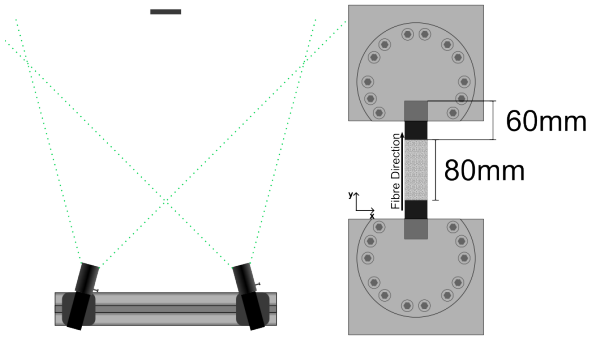

Figure 5.4: Test set-up for carbon fibre tape pre-preg, stereo cameras mounted on a rigid aluminium extrusion are used to capture the strains on the surface

To test the tape, 10 sections of 200mm CFRP tape are cut using scissors and the sections 80mm from the ends is covered with masking tape; they are then painted with white paint and speckled with black paint to create a section the DIC system could track displacements on. DIC is used to capture the strain on the surface of the sample, this allows for the capture of the transverse strain as well, which is used for measuring the ν_{12} Poisson ratio.

The testing device required a minimum spacing between the clamps, and this minimum distance exceeded the tape width. As a result, it was not possible to perform a mechanical test on the tape in the direction perpendicular to the fibres. The transverse properties could therefore not be tested.

Transverse mechanical properties were not measured experimentally because of geometric limitations of the testing setup. Instead, they were obtained through analytical methods. Since the material is primarily intended to carry loads along the fibre direction, its structural behaviour is dominated by the longitudinal properties. Therefore, the lack of experimental transverse testing does not affect the reliability of the conclusions drawn in this study.

Initially, the clamping pressure on the hydraulic clamps was set to 20 bar. Because slippage occurred during testing, the first two samples were rejected after sliding out of the clamps. The

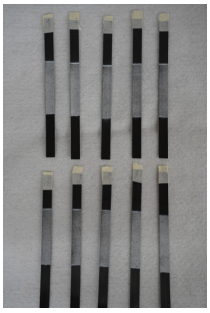

(a) 10 sections of 200mm CFRP tape with a painted speckle pattern applied

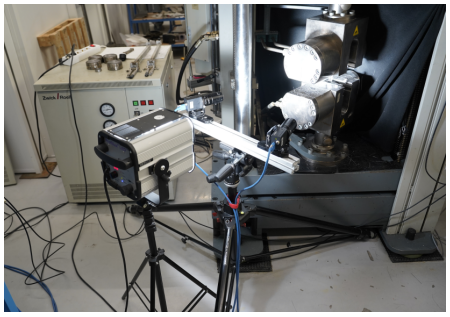

(b) Experimental set-up of tensile test on CFRP tape

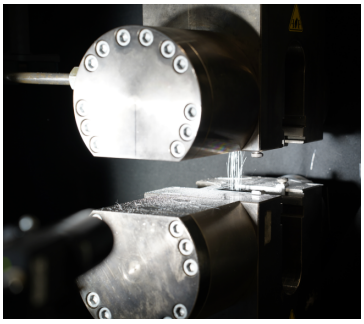

(c) Tape sample after tensile testing

Figure 5.5: Carbon fibre reinforced Pa12 tape experiment with DIC

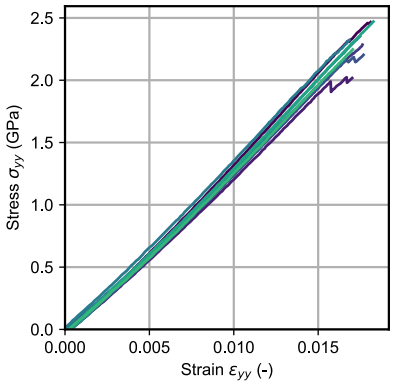

(a) Stress-strain graph

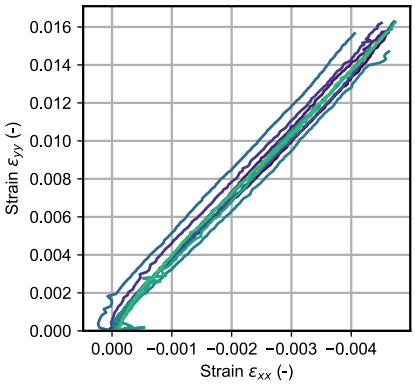

(b) Strain-transverse strain graph

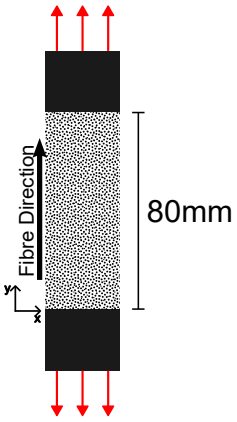

(c) Tape sample illustration with speckle pattern applied

Figure 5.6: Carbon fibre reinforced Pa12 tape mechanical properties

clamping pressure was then increased to 50 bar, which effectively prevented the tape sample from slipping.

Property	Symbol	Value	Source
Matrix Material	-	Polyamide 12	Supplier
Fibre Material	-	Carbon Fibre Standard Modulus	Supplier
Thickness	t	0.17 mm	Supplier
Width	w	12.7 mm	Supplier
Fibre Volume Fraction	v_f	0.62	Supplier
Elastic Modulus Parallel Fibre Direction	E_1	133.85 GPa	Measured
Elastic Modulus Perpendicular to Fibre Direction	$E_2 = E_3$	2164.776 MPa	Calculated
Poisson Ratio	$\nu_{12} = \nu_{13}$	0.291	Measured
Shear Modulus	$G_{12} = G_{13}$	6983.478 MPa	Calculated
Density	ρ	3.29 g/cm^3	Measured
Embodied CO2	I	54.823 kgCO_2/kg	[49]

Table 5.2: Carbon fibre unidirectional tape from Suprem

In Table 5.2, E_2 and G_{12} are calculated using Equation 5.2 and Equation 5.3 respectively with mechanical properties from the fibres and matrix taken from [50].

$$E_2 = \frac{(E_{2f} E_m)}{(\nu_m E_{2f} + \nu_f E_m)} \tag{5.2}$$

$$G_{12} = \frac{G_{12f} G_m}{\nu_m G_{12f} + \upsilon_f G_m} \tag{5.3}$$

5.3. Topology Optimised Designs & Manufacturing

The material properties obtained in the previous section is employed into our TO method. The volume fraction constraint in the TO methods is set to 0.4 make a fair comparison of the design method. The domain of the designs is shown in Figure 5.7, a length of 200mm is chosen for the largest dimension. The in plane thickness is set to 12mm and tape samples have 2 layers of tapes which are spaced 1mm from either end to give the samples a high out of plane bending stiffness. Out of plane bending will cause the sample to buckle and is therefore avoided.

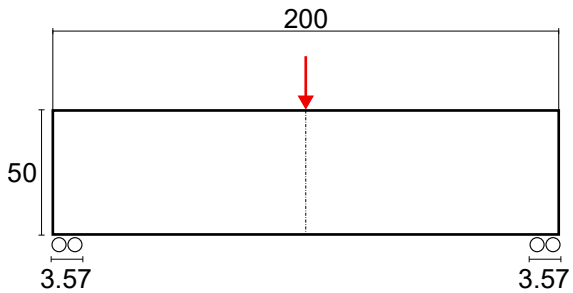

Figure 5.7: Dimensioned Messerschmitt-Bölkow-Blohm Beam domain: roller boundary conditions on either side and symmetry plane across the centre. Dimensions in millimeters.

The designs can be seen in Figure 5.8. (a)[DTO] shows the SIMP density based method which is made fully of the substrate ePa12 material, (b)[GPTONT] is the GPTO optimised design without the tapes, (c)[GPTO] is the optmised design with the tapes and finally (d)[GPTOGR] is the ground case for the GPTO for ATLAM method.

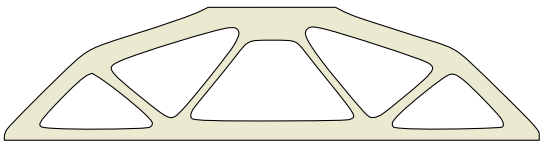

(a) Density based topology optimisation

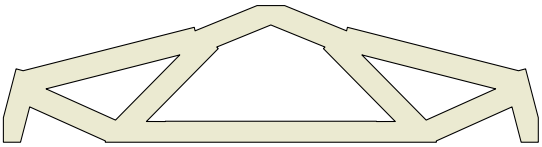

(b) Geometric projection topology optimisation without tapes

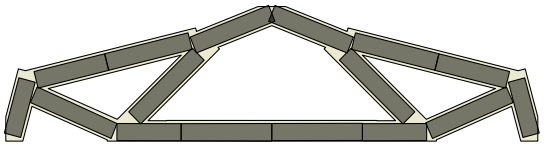

(c) Geometric projection topology optimisation

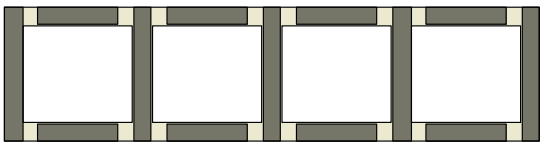

(d) Geometric projection topology optimisation ground case

Figure 5.8: Designs optimised for MBB loadcase, beige indicates substrate material and grey indicates tapes.

The structures are then manufactured using the workflow in Chapter 4, the one of each MBB Beam sample is shown in Figure 5.9. Three samples of each design is made for accurate and reliable results.

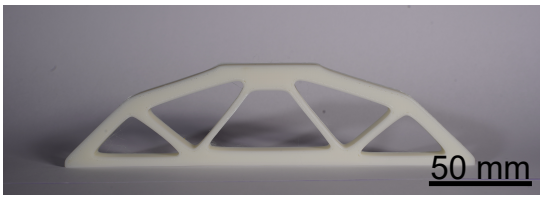

(a) Density based topology optimisation

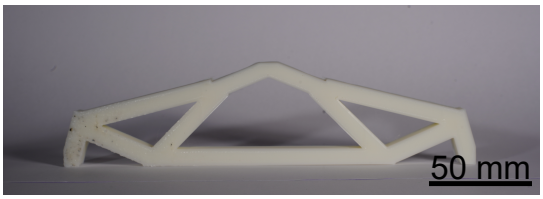

(b) Geometric projection topology optimisation without tapes

(c) Geometric projection topology optimisation

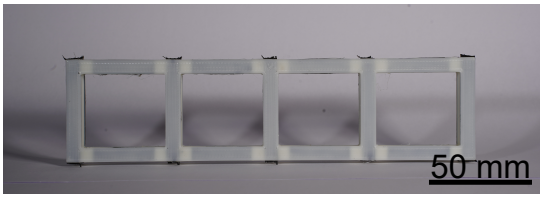

(d) Geometric projection topology optimisation ground case

Figure 5.9: Topology optimised ePa12 and Tape Messerschmitt-Bölkow-Blohm Beam specimens

5.4. Messerschmitt-Bölkow-Blohm Beam Experiments

The MBB beam load case lacks a one-to-one experimental realisation due to its idealized boundary conditions. Nevertheless, a three-point bending fixture offers a suitable approximation of the structural response under comparable loading. The three point bending fixture uses three fixed rollers, two fixed rollers for the roller boundary conditions at the bottom of the domain and one to apply the load in the top centre of the domain. The spacing on the bottom two rollers can be adapted to test varying sample sizes. The CAD model for the three point bending fixture is shown in Figure 5.10.

Mechanical testing of the MBB Beam samples is done to compare their experimental stiffness with the numerical stiffness. The samples are loaded using a 20kN Zwick Universal static testing machine. The top of the three point bending fixture is placed in-line with a load cell 20kN load cell, and the bottom of the fixture is placed on the moving cross-head. The experimental set-up is shown

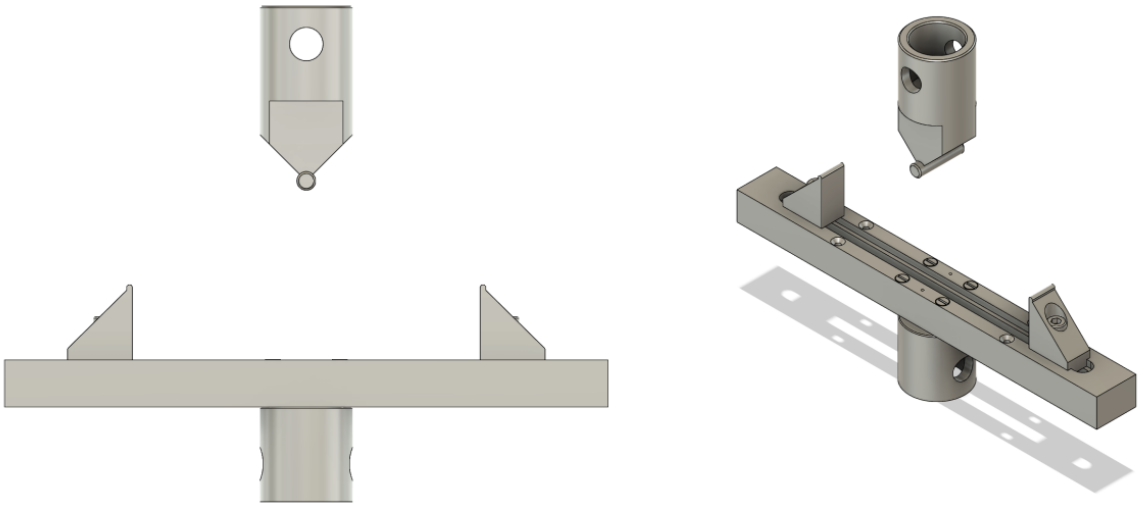

(a) Front view of the three point bending fixture

(b) Isometric view of the three point bending fixture

Figure 5.10: Three point bending fixture used as experimental MBB set-up, fixture uses roller sizes that can be changed and the distance between the bottom rollers can be adjusted.

in Figure 5.11.

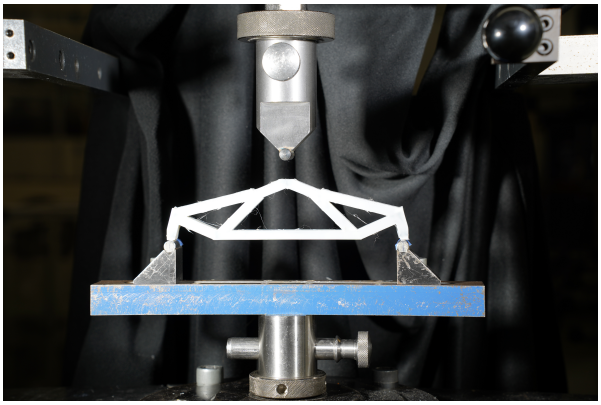

Figure 5.11: GPTO sample placed in the three point bending fixture

The cross-head is actuated using ball screw actuators with rotary encoders, and the encoder data is used for the displacement of the sample. In order to track local strain evolution, we use Digital Image Correlation (DIC) technique. To set up DIC technique, a set of monochrome cameras is used to capture pictures while the sample is being loaded. The samples are painted with a high contrast speckle pattern to allow the Vic 3D software from Correlated Solutions to track strains.

The DIC camera car uses two 4 Megapixel cameras that are placed on an aluminium extrusion, the extrusion is then mounted on a tripod and aimed at the centre of the sample. Both cameras are placed away from each other on the extrusion in order to have a 30° angle between each other (2 different angles are needed to track 3 dimensional strains).

To avoid interference from other experiments or light variations in the lab causing errors, a thick cloth is added behind the samples to block out light from behind. Then two flicker free, diffuse light spotlights are added, one from each side aiming at the sample from below to avoid any direct

reflections into the camera.

Before testing is started, the cameras must be focussed on the area of interest. First, the lights must be turned off, then the aperture of both cameras is opened up, this will make the depth of field short. Using this short depth of field, the live image from the camera will exaggerate the sharpness and blur in area in focus and out of focus, respectively, the sharpest section in the image is placed on the centre of the sample using the focus of the cameras. This makes the centre of the sample the focal point. The camera apertures are then closed and the lights turned on to have the cameras on their highest depth of field during the experiments. When a test begins, the cameras are set to take pictures at 2 frames per second.

During testing of the samples, the cross-head displacement is reset to zero at the moment the rollers pass over one another. The cross-head is set to 60mm apart at the start of each test to allow switching the sample in the fixture and have 10mm of clearance between the domain and the top roller. Then, the load cell is set to zero newtons when there is no contact on the top roller, this avoids load cell drift and ensures accuracy in the results. The test sequence begins with a 600mm/min move until a preload of 50N then the sequence is stopped until manually continued (this allows for the sample to be re-loaded if it is seen to be tilted or out of focus). The sample is then loaded at 5mm/min until the force drops to 80% of the maximum load or is stopped manually.

The force-displacement responses of all test designs from the tests shown in Figure 5.12. The response begins flatter with an initial stiffening from the rough surface and the burs being loaded, then the full structure is loaded. Next, there is a region where the behaviour is linear; in this region the structure and load paths are fully engaged, these are the points used for a least squares linear regression to find the stiffness of the structure. After the linear region, the samples begin to buckle or fracture, which causes the force-displacement diagram to plateau.

Sample	Code	Stiffness [kN/mm]		Relative Error In Stiffness [%]
		Experimental	Numerical	
Density-based Topology Optimization	DTO	0.366	0.390	6.64
Geometric Projection Topology Optimization without Tapes	GPTONT	0.355	0.344	-0.0352
Geometric Projection Topology Optimization	GPTO	0.493	0.929	88.5
Geometric Projection Topology Optimization Ground Case	GPTOGR	0.0562	0.0818	45.6

Table 5.3: Experimental & Numerical stiffness for MMB Beam Samples

The numerical results in Table 5.3 are generated using a finite element model based on the tape and substrate placement of each design. The model uses plane stress assumptions. Additionally, the model assumes the substrate to be linear and isotropic, and the tape to be transversely isotropic. The

The experimental and numerical stiffness can be seen in Table 5.3. The relative error is calculate using,

$$RE = 100 \times \frac{k_{\text{num}} - k_{\text{exp}}}{k_{\text{exp}}} \tag{5.4}$$

where RE is the relative error in %, k_{num} is the stiffness of the sample found using the numerical method and k_{exp} is the average stiffness of the samples evaluated experimentally. The stiffness for the DTO and GPTONT samples show agreement with a relative error of 6.64% and -0.0352% dif-

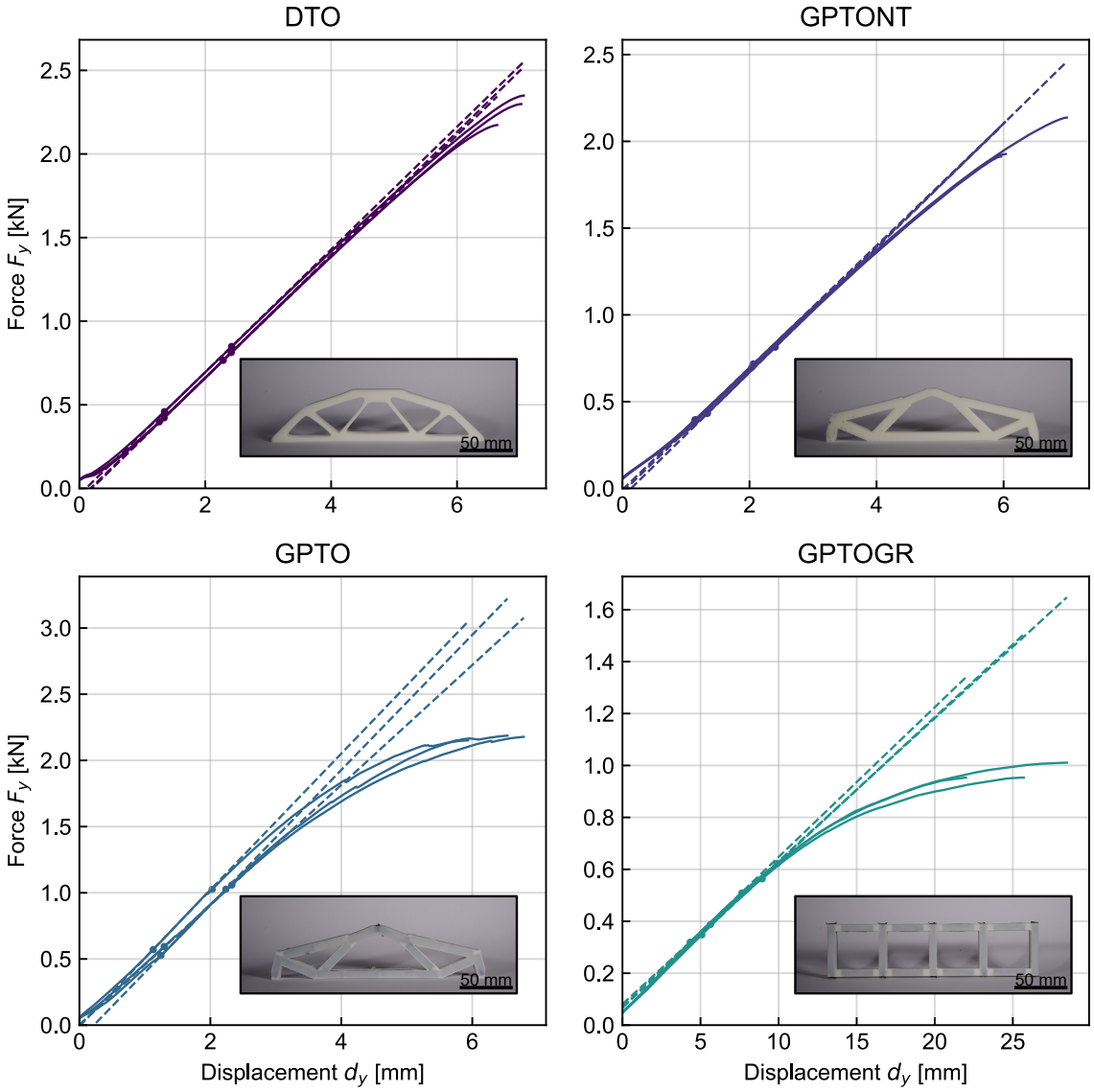

Figure 5.12: Computationally designed MMB Beam samples force-displacement graphs

ference respectively from the experimental results. The GPTO and GPTOGR samples, on the other hand, deviate substantially from the experimental results: the GPTO design exhibits an 88.5% error relative to the experimental value, while the GPTOGR shows a 45.6% error.

The agreement of the experimental and numerical results of the GPTONT and DTO samples, which are composed of only FDM manufactured substrate results, suggests that the model is accurate for FDM structures; therefore, the mismatch must stem from either the interface between the tapes and the substrate or the tapes themselves. Typically, an issue in the thermoplastic welding would show up as voids in the interface. These voids would then open up and coalesce as the structure is being loaded. The load-displacement graph shows no damage as the tapes are loaded or events of strain energy release. This indicates that the mismatch could stem from the modelling of the tapes.

The tapes are assumed linear elastic in both tension and compression, but in reality only tension material tests have been used in the characterisation. The MBB Beam load-case has many regions loaded in compression, and therefore, the assumption that the tapes behave the same in compression as in tension may not be valid; however, it is unlikely to be the dominant cause given that the compressive modulus of unidirectional CFRP is typically close to its tensile value. An additional source of the error could be the placement sensitivity of the tapes, by finding the most optimal design the optimiser will find a local minima in the design space with steep changes in design compliance alongside the optimum. These steep changes in compliance in the minima will inherently find designs with a high sensitivity to tape placement accuracy. A potential source of this sensitivity was the connection points between the tapes, a small error in the placement would allow the tapes to be fused to each other or to have a substrate gap in-between. In turn this small error would replace the material in the path of the load with compliant substrate material or stiff tape material, drastically changing the structure compliance. This was partially corroborate with the lower error for the GPTOGR sample in which the tapes are spaced with no potential overlaps or potential touching from placement error.

To investigate this issue, an additional design is created, this time the tapes that are adjacent and in-line are replaced with one longer tape, and non in-line tapes are spaced with substrate in between. This design should be significantly less sensitive to the placement of the tape. The design is shown in Figure 5.13, the number of tapes is reduced from 16 per tape embedded layer to 11.

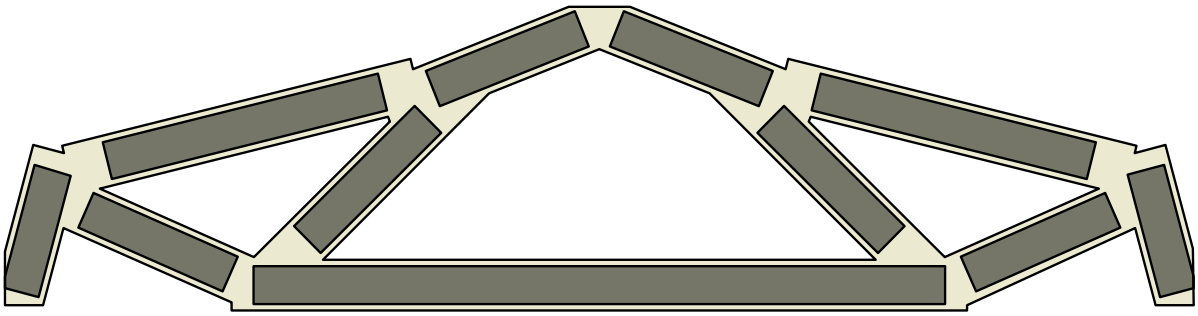

Figure 5.13: Geometric projection topology optimisation design with post processing for spacing the tapes at the joints and joining in-line tapes. optimised for MBB loadcase, beige indicates substrate material and grey indicates tapes.

The post-processed GPTO design was manufactured and 3 identical samples were tested using the 3 point bending fixture. The force deflection graph shown in Figure 5.14 depicts a similar shape to the GPTO sample with a slight increase in stiffness (+4.26%).

When the GPTOPP sample's experimental stiffness is compared with the numerical stiffness there is a decrease in the relative error. This indicates the sensitivity of the placement of the tape played a significant role in the numerical experimental discrepancy but there remains a error.

The remaining error is attributed to incomplete load introduction into the tapes: a shear lag

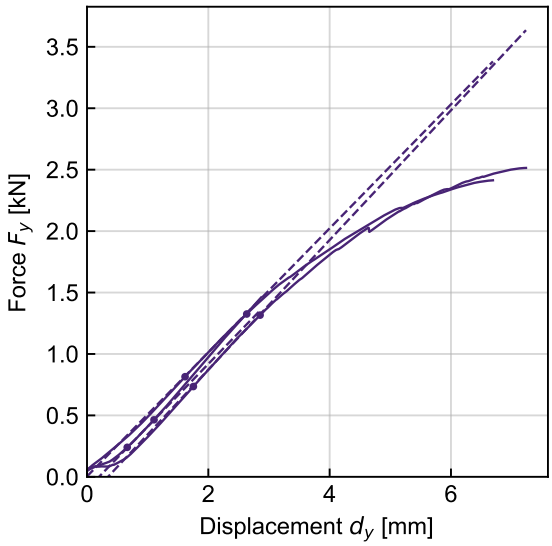

Figure 5.14: Force displacement graph of post processed GPTO design

Sample	Code	Stiffness [kN/mm]		Relative Error In Stiffness [%]
		Experimental	Numerical	
Geometric Projection Topology Optimization	GPTO	0.493	0.929	88.5
Geometric Projection Topology Optimization Post-processed	GPTOPP	0.514	0.782	52.2

Table 5.4: Experimental & Numerical stiffness for MMB Beam Samples

effect. In the numerical model, each tape is assumed to carry its full axial load uniformly along its entire length. In reality, load is transferred from the substrate into the tape through interfacial shear stress, and this transfer requires a finite length to develop. The rate of load transfer is governed by the ratio of the tape axial stiffness to the substrate shear stiffness. For the materials used here, this ratio is approximately 93 ($E_1/E_{\text{substrate}} \approx 133\ \text{GPa}/1.44\ \text{GPa}$), meaning the substrate is far too compliant to fully load the tape over a short transfer length. As a result, the tape axial load at mid-length remains below the value the model assumes, and the tape contributes less stiffness than predicted. This effect is visible in the DIC strain maps of the GPTO samples, seen in Appendix C, where elevated strain concentrations are observed at the tape endpoints, precisely the locations where the substrate is attempting to introduce load into the tape. The model would need to incorporate a shear lag correction factor, scaling the effective tape stiffness as a function of tape aspect ratio and the substrate-to-tape stiffness ratio, in order to reduce this remaining discrepancy.

The shear lag theory for the error is further corroborated by the comparison of the DIC strains to the FEM strains, seen in Figure 5.15, where the strain concentrations at the ends of the tapes from the DIC data are larger than expected.

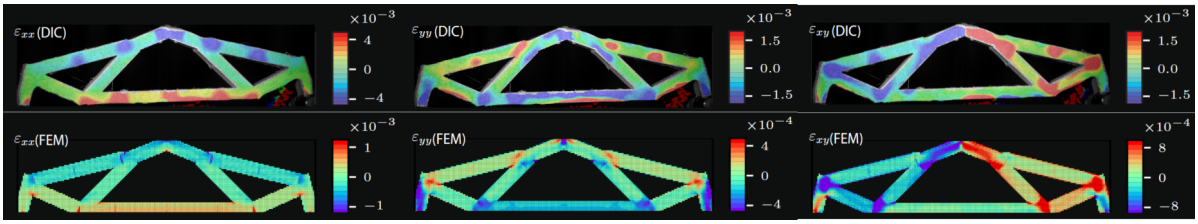

Figure 5.15: Local strain data of GPTO sample through DIC and FEM at 1kN force on the 3 point bending fixture and MBB domain respectively [49]

Figure 5.16 shows the resulting stiffness of the samples normalized by the experimental weight in (a) and by the calculated embodied CO_2 on the right (b). The material use shown in Table 5.5, is calculated using the filament volume predicted by PrusaSlicer for the Prusa XL gcode and the sum of the tape lengths used in the designs shown in Figure 5.8. The material use multiplied by the material embodied CO_2 gives the samples total CO_2 this value is shown in Table 5.5. The values for each design are then plotted in Figure 5.16.

The GPTO sample shows an improvement in the stiffness-weight ratio over FDM with DTO which highlights the stiffness gain from tape-reinforcement. The GPTONT sample is outperformed in stiffness by the DTO sample. This is due to the constraints added to GPTONT design method, as the TO algorithm is constrained to wide rectangular sections while DTO uses rounded slim shapes, which appears to improve the performance. The worst performing sample, GPTOGR is 10 times more compliant than its optimised version the GPTO sample. The optimiser has therefore shown a significant improvement in the stiffness to weight ratio over the ground design, which demonstrates the advantage of optimizing geometry and reinforcement placement using our approach.

Sample	Stiffness [kN/mm]	ePa12 Volume [mm^3]	Tape Length [mm]	Embodied CO_2 [kg of CO_2]
DTO	0.366	4.24×10^4	0	0.585
GPTONT	0.355	4.90×10^4	0	0.677
GTPO	0.493	4.74×10^4	948	1.17
GTPOGR	0.0562	4.81×10^4	980	1.19

Table 5.5: Stiffness, material use and embodied CO_2 for each design

The experiments shown in Figure 5.16, demonstrate that the GPTO for ATLAM method and the desktop workflow enables designs that span the range of higher stiffness-weight ratios and lower

stiffness-embodied CO_2 ratios. The GPTO design shows a stiffness to embodied CO_2 ratio of around 12 times the ground design, while changing the manufacturing method and material yields only a 1/3 increase, this emphasises strategic design as a key factor in eco-efficiency.

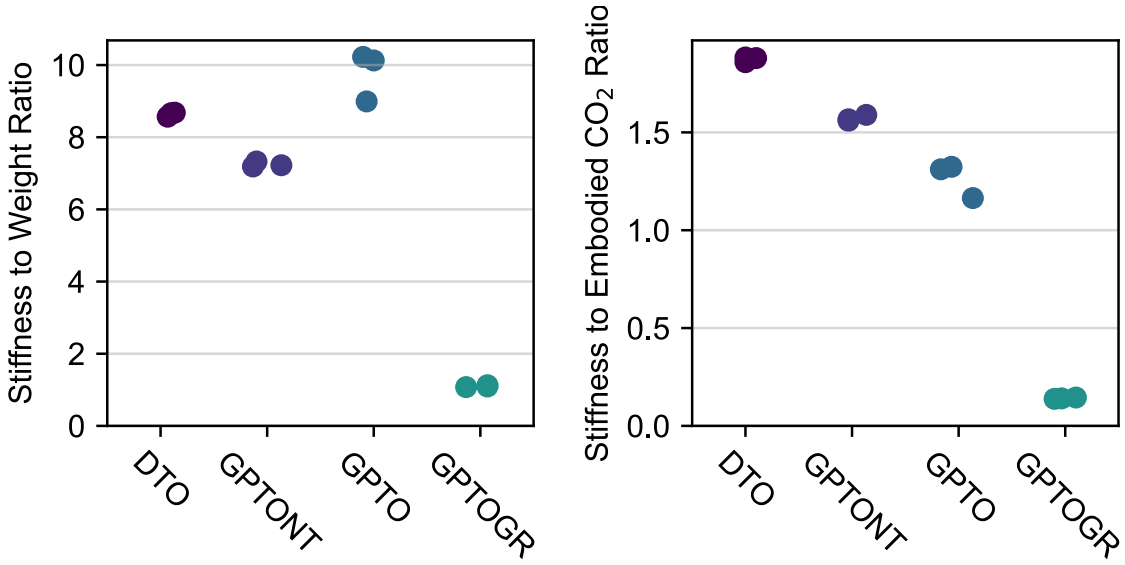

Figure 5.16: Computationally designed MMB Beam samples stiffness to weight ratio [(kN/mm)/kg] and stiffness to embodied CO_2 ratio [(kN/mm)/CO_2]

5.5. Chapter Summary

This chapter employed the desktop ATLAM workflow to experimentally validate the models and design methods implemented in GPTO for ATLAM. The validation procedure was described, and the selection of experiments was justified. Subsequently, the ePa12 substrate and Carbon FRP tape materials were characterised via tensile testing to obtain material properties required in the design methods. These methods were then applied to generate four designs, which were subsequently manufactured. The fabricated specimens were tested in a fixture selected to reproduce the MBB boundary conditions. The resulting sample stiffness was analysed and compared with the experimental data, revealing a significant discrepancy for the specimens with tape reinforcements, indicating that further research is needed to determine the underlying cause.

6

Conclusions

RQ1.1 How can scaled Advanced Tape Layer Additive Manufacturing architectures be produced with a conventional desktop 3D printer?

The literature study revealed multiple methods to create desktop scale ATLAM structures from continuous fibre printing to automated fibre placement methods for the tapes and fused deposition modelling for the substrate. The choice was made to use a simpler method that would avoid the use of expensive hardware such as an AFP machine. Although this would result in lower manufacturing quality for the purposes of development of the models and the design methods for ATLAM this is acceptable.

A workflow was designed to add continuous carbon fibre thermoplastic tapes within a 3D print, using the ability to embed items leaving a pocket in which the tapes are added and welded in. The method was used to create lap shear samples using 2 different manual welding methods, both manual welding methods provided enough strength but lacked the surface quality and reliability needed for this process. The first method, thermal conduction heating provided more consistent surface quality over the second method, ultrasonic welding. Both manual welding methods were time intensive and are therefore not suitable for the objective of the thesis.

The workflow was then adapted to use a in-house tool to weld the tapes using the 3D printer's gantry to provide accurate movement control. To control the tool a Python script was developed to create g-code commands that the 3D printer can use to weld the tapes. The automated welding provided a consistent smooth surface on the top of the tape which decreased the defects in the subsequent layer and reduced the fibres damaged in the welding process. In addition, the method was significantly faster, and this method was then used in the manufacturing of the samples for experimental validation.

RQ1.2 Does the inclusion of continuous fibre-reinforced tapes provide measurable mechanical reinforcement to the additively manufactured thermoplastic substrate?

The improvement in stiffness as an effect of the tape reinforcement is shown by the GPTO samples over the GPTONT samples, increasing stiffness by 39%. As a result, it has been proven that the automated welding method combined with the desktop ATLAM method is able to reinforce the substrate with continuous fibre tapes.

RQ2.1 Do the numerical models accurately reproduce the experimentally measured stiffness of the Geometrically Projected Topology-Optimised structures designed for ATLAM?

The numerical models demonstrate mixed agreement with the stiffness measured experimentally depending on the design configuration. For substrate-only designs, the models show excellent agreement: the DTO design exhibits a relative error of 6.64% and the GPTONT design an essentially negligible error of -0.035%, confirming that the finite element model accurately captures the structural behaviour of FDM-manufactured thermoplastic substrates. For tape-reinforced designs, however, the models significantly overpredict stiffness. The GPTO design exhibits a relative error of 88.5% and the GPTOGR design a relative error of 45.6% relative to the experimentally measured

values. To investigate the source of this discrepancy, a post-processed design GPTOPP was manufactured and tested, in which adjacent in-line tapes were merged into single continuous tapes and non-in-line tapes were spaced with substrate material between them to reduce sensitivity to tape placement accuracy. The GPTOPP design reduced the relative error from 88.5% to 52.2%, confirming that tape placement sensitivity at connection points is a significant contributing factor. The remaining discrepancy is attributed to a shear lag effect, whereby the compliant thermoplastic substrate is unable to fully introduce the axial load into the tape over the available transfer length. It is therefore concluded that the numerical model is fully validated for substrate behaviour but requires the incorporation of a tape knockdown factor to account for shear lag before it can be considered reliable for tape-reinforced ATLAM designs

RQ2.2 Does the local strain field obtained from Digital Image Correlation align qualitatively and quantitatively with the predictions of the finite element model?

The experimental DIC data show good qualitative agreement with the numerical strains. There is tension on the compression members and tension on the bottom members, with regions of strain concentrations at the locations where the tapes meet. The strain concentrations are larger in the experimental data, this indicates the presence of shear lag. The shear lag effect reduces the reinforcement effect of the tapes within the structure, as the substrate requires a significant length of tape to fully load the tape in the axial direction.

In tape reinforced GPTO design, there is a systematic and substantial quantitative discrepancy in strain magnitude. The DIC measurements show ϵ_{xx} values reaching approximately $\pm 4 \times 10^{-3}$, while the FEM predicts only $\pm 1 \times 10^{-3}$, a factor of roughly four. The same trend is observed in ϵ_{yy} (DIC: $\pm 1.5 \times 10^{-3}$, FEM: $\pm 4 \times 10^{-4}$) and ϵ_{xy} (DIC: $\pm 1.5 \times 10^{-3}$, FEM: $\pm 8 \times 10^{-4}$). Since these strain measurements were taken at the same applied load, a strain field that is uniformly larger by a factor of approximately four corresponds directly to a structure that is approximately four times more compliant than the model assumes, consistent with the 88.5% stiffness overprediction observed in the global force-displacement response.

The fact that the discrepancy is uniform across all three strain components and consistent with the global stiffness error, rather than localised or pattern-distorting, rules out bond failure and localised defects as the primary cause. Bond failure would produce strain discontinuities or anomalous localised fields not predicted by the FEM; none are observed. This supports the shear lag interpretation: the tapes are active and carrying load along the correct paths, but at a globally reduced magnitude because the substrate cannot introduce the full axial load into each tape over the available transfer length.

RQ3.1 How does the structural efficiency of GPTO compare to that of conventional density-based topology optimisation approaches?

The GPTO design achieves a higher experimental stiffness-to-weight ratio of 9.78 kN/mm/kg compared to 8.64 kN/mm/kg for the DTO design, demonstrating that the geometric projection approach, which explicitly incorporates ATLAM manufacturing constraints and selective tape reinforcement, produces structurally superior designs relative to the established density-based industry standard for this load case and material system.

RQ3.2 How does the stiffness of the GPTO optimised design compare to that of its unoptimised initial configuration?

The optimised GPTO design is approximately 8.8 times stiffer than the GPTOGR ground case (0.493 vs 0.056 kN/mm), confirming that the optimisation process provides a very large structural improvement over the unoptimised initial design.

RQ3.3 How does the structural performance of the tape-reinforced GPTO design compare to the geometrically equivalent isotropic unreinforced substrate design?

The tape-reinforced GPTO design is approximately 39% stiffer than the geometrically equivalent substrate-only GPTONT design, confirming the structural benefit of tape reinforcement even under the conservative load introduction conditions of the desktop manufacturing process.

RQ3.4 How does the stiffness-to-embodied-CO_2 ratio achieved by GPTO compare to that of established industry-standard topology optimisation methods?

The GPTO design achieves a higher experimental stiffness-to-weight ratio of approximately 10 kN/mm/kg compared to the DTO design which achieves approximately 8–9 kN/mm/kg. This demonstrates that the geometric projection approach, which explicitly incorporates ATLAM manufacturing constraints and selective tape reinforcement, produces structurally superior designs relative to the established density-based industry standard for this load case and material system.

The GPTO design achieves a higher stiffness-to-embodied-CO_2ratio than the DTO design, as shown in Figure 5.16. While the DTO design benefits from a lower embodied CO_2due to the exclusive use of thermoplastic substrate material, the GPTO design compensates through a disproportionately larger gain in structural stiffness. This confirms that the eco-efficiency constraint embedded in the GPTO framework successfully identifies designs that are both structurally and materially efficient, outperforming the density-based industry standard on this metric.

Overall Conclusion

The desktop ATLAM workflow developed in this thesis successfully bridges the gap between the full-scale ATLAM process and affordable experimental validation. The substrate model is fully validated, and the GPTO design method is shown to outperform density-based alternatives on both stiffness-to-weight and stiffness-to-embodied-CO_2 metrics. The principal outstanding limitation is the overprediction of tape-reinforced stiffness. This has been partially resolved by reducing tape placement sensitivity through the GPTOPP post-processing approach, which alone reduced the relative error from 88.5% to 52.2%. The DIC strain analysis provides strong evidence that the remaining error is a shear lag effect: the strain patterns are qualitatively correct but uniformly underestimated by the model by a factor of approximately four, consistent with the global stiffness overprediction and inconsistent with localised failure mechanisms.

The results of this thesis were included in a publication:

C. Jansari, D. Canosa Ybarra, M. Langelaar, C. Ayas, and K. Masania, "Design for Tape-reinforced Additive Manufacturing using Geometric Projection Topology Optimization," Additive Manufacturing, *under review*, 2026.

Recommendations

The experimental results and DIC strain analysis presented in this thesis provide strong evidence that the primary source of discrepancy between the numerical and experimental stiffness of tape-reinforced designs is a shear lag effect, whereby the compliant thermoplastic substrate is unable to fully introduce the axial load into the tape over the available transfer length. A full shear lag correction implemented directly into the finite element model would resolve this discrepancy but would introduce significant additional computational complexity, which is undesirable in an optimisation framework where the finite element problem must be solved repeatedly at each iteration. It is therefore recommended that future work investigates the implementation of a tape knockdown factor applied directly to the tape material properties within the GPTO stiffness model. This knockdown factor would scale the effective tape axial stiffness as a function of the tape aspect ratio and the substrate-to-tape stiffness ratio, capturing the influence of shear lag without requiring an explicit shear lag formulation in the finite element model. Such an approach represents a practical compromise between model fidelity and computational efficiency, and could be calibrated against the existing experimental dataset presented in this thesis, providing an immediately available validation basis. Once calibrated, this corrected model would be expected to significantly reduce the remaining stiffness overprediction observed in the GPTO and GPTOPP designs, bringing the nu-

merical predictions into closer agreement with experimental results and increasing confidence in the GPTO framework as a reliable design tool for ATLAM structures.

When welding the tapes a phenomenon was revealed where the process of stamping the tape to keep it in place would attach the tape onto the tool, subsequently the stamping for a longer duration would attach the tape onto the substrate. Although in the previous experiments it was undesired this process could in the future be used to deposit tapes at exact locations using the tool. A additional motor could be added to the current extruder that would use the existing electronics, replacing the extruder (which is not used to compact tapes), to rotate the compactor tool around a vertical axis. This would allow for the rotation and depositing of tapes to the correct location. This would drastically cut down the time needed to produce these tape reinforced structures and increase the placing accuracy and precision over manual placement.

The desktop-scale ATLAM workflow was limited to two tape layers through the 12mm thickness, reinforcing only 0.34mm of the cross-section, and future work should investigate the maximum number of tape layers per millimetre that can feasibly be placed, as increasing tape content would directly improve the stiffness-to-weight ratio towards industrially relevant performance levels.

When creating desktop scale ATLAM samples many printing parameters were adjusted to best mimic the ATLAM process. Therefore 100% infill was used throughout the sample but the strategic placement of higher infills can be further used to increase the strength to weight ratio. A consistent layer height of 0.2mm was used to simplify the process but the tapes were 0.17mm thick so adjustable layer heights could be used to improve the geometrical match of the pocket and the tape, so that the layer is as thick as the tape. Finally the process could be sped up by using a nozzle with a larger diameter, this would increase the roughness of the surface of the print but that does not affect this specific application.

In this thesis, a method was developed to bond thermoplastic tapes to a thermoplastic substrate, but the strength of the resulting joint and the quality were not evaluated. Future work should address this by determining the limits of this bonding technique. Furthermore, the compactor was designed to accommodate a spring around the shaft, enabling the compaction pressure to be controlled via the printer's displacement settings. By replacing this spring, different compaction pressures can be applied. This option should be investigated, and its influence on bond strength and on the void content within the bond should be quantified.

Bibliography

[1] H. Ritchie, "What share of global CO emissions come from aviation?,"

[2] S. Writer, "A brief history of aircraft materials."

[3] "Airplane - materials, construction, design | britannica."

[4] "Aviation's material evolution | airbus."

[5] X. Xu, G. Peng, B. Zhang, F. Shi, L. Gao, and J. Gao, "Material performance, manufacturing methods, and engineering applications in aviation of carbon fiber reinforced polymers: A comprehensive review," vol. 209, p. 112899.

[6] B. Iacopo, M. Chiara, S. Michela, and V. Tommaso, "Life cycle analyses of a composite towbar realized via filament winding and comparison with traditional metallic alternatives," vol. 40, p. e00980.

[7] "Changing the world with new materials. a half-century history of CFRP. - revista MMC."

[8] P. K. Mallick, *Fiber-reinforced composites: materials, manufacturing, and design.* CRC Press, 3. ed ed.

[9] "Fabrics for reinforcement of engineering composites," in *Engineering of High-Performance Textiles*, pp. 489–512, Woodhead Publishing.

[10] "Forged composites replace complex metal parts."

[11] A. Arulprasanna and M. Omkumar, "A review on composites: Selection and its applications,"

[12] D. P. B. C. B. J. Julie Teuwen, Ran Tao, "PCM_Online_Lecture1 - AE4ASM110-22 Polymer Composites Manufacturing (2022/23 Q2)."

[13] M. A. Lamontia, M. B. Gruber, B. J. Waibel, R. D. Cope, and A. B. Hulcher, "CONFORMABLE COMPACTION SYSTEM USED IN AUTOMATED FIBER PLACEMENT OF LARGE COMPOSITE AEROSPACE STRUCTURES,"

[14] M. Özkaymak, Y. Öz, and Z. Evis, "Review, manufacturing, and tooling processes for continuous reinforced high-performance thermoplastic composites and related thermal analyses," p. 07316844251345653.

[15] D. Peeters, "PCM_Online_Lecture7 - AE4ASM110-22 Polymer Composites Manufacturing (2022/23 Q2)."

[16] J. P. H. Belnoue, T. Mesogitis, O. J. Nixon-Pearson, J. Kratz, D. S. Ivanov, I. K. Partridge, K. D. Potter, and S. R. Hallett, "Understanding and predicting defect formation in automated fibre placement pre-preg laminates," vol. 102, pp. 196–206.

[17] A. Brasington, C. Sacco, J. Halbritter, R. Wehbe, and R. Harik, "Automated fiber placement: A review of history, current technologies, and future paths forward," vol. 6, p. 100182.

[18] I. F. V. Bram Jongbloed, "PCM_Online_Lecture11 - AE4ASM110-22 Polymer Composites Manufacturing (2022/23 Q2)."

[19] G. Rousseau, R. Wehbe, J. Halbritter, and R. Harik, "Automated fiber placement path planning: A state-of-the-art review," vol. 16, no. 2, pp. 172–203.

[20] H. Suemasu, Y. Aoki, H. Hoshi, Y. Tateishi, S. Sugimoto, and T. Nakamura, "Thermal analysis for in-situ consolidation in the AFP process," vol. 172, p. 107577.

[21] J. Jiang, Y. He, H. Wang, and Y. Ke, "Modeling and experimental validation of compaction pressure distribution for automated fiber placement," vol. 256, p. 113101.

[22] R. J. Cano, H. L. Belvin, A. B. Hulcher, and R. W. Grenoble, "Studies on automated manufacturing of high performance composites," NTRS Author Affiliations: NASA Langley Research Center NTRS Document ID: 20040086087 NTRS Research Center: Langley Research Center (LaRC).

[23] F. O. Sonmez and H. T. Hahn, "Modeling of heat transfer and crystallization in thermoplastic composite tape placement process," vol. 10, no. 3, pp. 198–240. Publisher: SAGE Publications Ltd STM.

[24] "General atomics aeronautical developing tool-less thermoplastics composites process."

[25] D. H. J. A. Lukaszewicz, C. Ward, and K. D. Potter, "The engineering aspects of automated prepreg layup: History, present and future," vol. 43, no. 3, pp. 997–1009.

[26] M. Wiehn and R. Hale, "Low cost robotic fabrication methods for tow placement," in *47 th International SAMPE Symposium and Exhibition 2002*, pp. 1842–1852, 2002.

[27] D. H.-J. A. Lukaszewicz, *Optimisation of high-speed automated layup of thermoset carbon-fibre preimpregnates*. PhD thesis, University of Bristol, 2011.

[28] M. Rakhshbahar and M. Sinapius, "A novel approach: Combination of automated fiber placement (AFP) and additive layer manufacturing (ALM)," vol. 2, no. 3, p. 42. Publisher: Multidisciplinary Digital Publishing Institute.

[29] G. Clancy, D. Peeters, R. M. O'Higgins, and P. M. Weaver, "In-line variable spreading of carbon fibre/thermoplastic pre-preg tapes for application in automatic tape placement," vol. 194, p. 108967.

[30] G. Rasiya, A. Shukla, and K. Saran, "Additive manufacturing-a review," vol. 47, pp. 6896–6901.

[31] A. Cano-Vicent, M. M. Tambuwala, S. S. Hassan, D. Barh, A. A. A. Aljabali, M. Birkett, A. Arjunan, and Serrano-Aroca, "Fused deposition modelling: Current status, methodology, applications and future prospects," vol. 47, p. 102378.

[32] Y. Shi, C. Yan, Y. Zhou, J. Wu, Y. Wang, S. Yu, and Y. Chen, "Chapter 4 - Polymer material for additive manufacturing–filament materials," in *Materials for Additive Manufacturing* (Y. Shi, C. Yan, Y. Zhou, J. Wu, Y. Wang, S. Yu, and Y. Chen, eds.), 3D Printing Technology Series, pp. 361–401, Academic Press.

[33] Y. Li and Y. Lou, "Tensile and Bending Strength Improvements in PEEK Parts Using Fused Deposition Modelling 3D Printing Considering Multi-Factor Coupling," vol. 12, no. 11, p. 2497.

[34] M. A. Islam, M. H. Mobarak, M. I. H. Rimon, M. Z. Al Mahmud, J. Ghosh, M. M. S. Ahmed, and N. Hossain, "Additive manufacturing in polymer research: Advances, synthesis, and applications," vol. 132, p. 108364.

[35] S. Grieder, I. Zhilyaev, M. Küng, C. Brauner, M. Akermann, J. Bosshard, P. Inderkum, J. Francisco, Y. Willemin, and M. Eichenhofer, "Consolidation of Additive Manufactured Continuous Carbon Fiber Reinforced Polyamide 12 Composites and the Development of Process-Related Numerical Simulation Methods," vol. 14, no. 16, p. 3429.

[36] M. Ueda, S. Kishimoto, M. Yamawaki, R. Matsuzaki, A. Todoroki, Y. Hirano, and A. Le Duigou, "3D compaction printing of a continuous carbon fiber reinforced thermoplastic," vol. 137, p. 105985.

[37] N. Elderfield and J. C. H. Wong, "Discrete in-situ consolidation of additively manufactured continuous fiber-reinforced polymer composites," vol. 171, p. 107562.

[38] M. Eichenhofer, G. CAVOLINA, and C. HOUWINK, "Verfahren und vorrichtung zum abschneiden eines extrudates."

[39] A. LUIJTEN, P. ZDROIK, C. HOUWINK, M. Eichenhofer, and G. CAVOLINA, "Method and apparatus for modeling and forming fiber-reinforced composite objects."

[40] K. A. Fetfatsidis, "Systems and methods relating to 3D printing composite structures."

[41] G. T. Mark and A. S. Gozdz, "Additively manufactured part including a compacted fiber reinforced composite filament."

[42] G. T. Mark and A. S. Gozdz, "Methods for composite filament threading in three dimensional printing."

[43] A. V. AZAROV, M. V. GOLUBEV, F. K. ANTONOV, and A. R. KHAZIEV, "Print head for additive manufacturing of articles."

[44] A. V. AZAROV, F. K. ANTONOV, M. V. GOLUBEV, and A. R. KHAZIEV, "Production of articles made of composite materials by 3D-printing method."

[45] H. Li, B. Liu, L. Ge, Y. Chen, H. Zheng, and D. Fang, "Mechanical performances of continuous carbon fiber reinforced PLA composites printed in vacuum," vol. 225, p. 109277.

[46] H. J. O'Connor and D. P. Dowling, "Low-pressure additive manufacturing of continuous fiber-reinforced polymer composites," vol. 40, no. 11, pp. 4329–4339.

[47] "ATLAM combines composite tape laying, large-scale thermoplastic 3D printing in one printhead."

[48] J. A. Norato, B. K. Bell, and D. A. Tortorelli, "A geometry projection method for continuum-based topology optimization with discrete elements," vol. 293, pp. 306–327.

[49] M. L. C. A. K. M. Chintan Jansari, David Canosa Ybarra, "Design for tape-reinforced additive manufacturing using geometric projection topology optimization,"

[50] S. Grieder, I. Zhilyaev, M. Küng, C. Brauner, M. Akermann, J. Bosshard, P. Inderkum, J. Francisco, Y. Willemin, and M. Eichenhofer, "Consolidation of Additive Manufactured Continuous Carbon Fiber Reinforced Polyamide 12 Composites and the Development of Process-Related Numerical Simulation Methods," vol. 14, no. 16.

A

Code

Listing A.1: Code to create the compaction gcode for the Prusa XL

```
import matplotlib.pyplot as plt
import matplotlib as mpl
import numpy as np
from openpyxl import load_workbook
from SampleTapeTopOp.functions.VectorMath import *
from SampleTapeTopOp.functions.PlottingSlotCode import *

mpl.rcParams['figure.dpi'] = 300
def mag(array: np.array):
    A = array[:, 1] - array[:, 0]
    mag = (A[0] ** 2 + A[1] ** 2) ** 0.5
    return mag


class Line:
    def __init__(self, x1, y1, x2, y2, Cx1, Cy1):
        self.data = np.array([[x1, x2],
                              [y1, y2]])
        self.x1, self.y1, self.x2, self.y2 = x1, y1, x2, y2
        dx, dy = x2 - x1, y2 - y1
        self.grad = dy / dx if dx != 0 else np.inf
        self.normGrad = -1 / self.grad if not np.isclose(self.grad, 0, rtol=1
            e-8) else np.inf
        self.centerPoint = np.array([[(x1 + x2) / 2],
                                     [(y1 + y2) / 2]])
        self.normLine = np.array([[self.centerPoint[0, 0], Cx1],
                                  [self.centerPoint[1, 0], Cy1]])

        # self.normLine /= mag(self.normLine) NOT A VECTOR YET
        self.Cx1, self.Cy1 = Cx1, Cy1

    def plot(self, color="Blue", constructionLines=True):
        plt.plot(self.data[0, :], self.data[1, :], color=color, linewidth=1)
        if constructionLines:
            plt.plot(self.normLine[0, :], self.normLine[1, :], color="r",
                linewidth=0.5)
            plt.plot(self.centerPoint[0, 0], self.centerPoint[1, 0], marker="
                x", color="r", linewidth=3)
            plt.plot(self.Cx1, self.Cy1, marker="x", color="r", linewidth=3)
```

```
    def __repr__(self):
        return f"L: ({self.data[0, 0]}, {self.data[1, 0]}) - ({self.data[0, 
            1]}, {self.data[1, 1]})"

    def find_intersection(self, other):
        # find y intercept in y = mx + >c<
        cs = self.y1 - (self.grad * self.x1)
        co = other.y1 - (other.grad * other.x1)
        # find intersection
        x_intersection = (co - cs)/(self.grad - other.grad)
        y_intersection = self.grad * x_intersection + cs

        # check if in bounds


class Rectangle:
    """
    Class creates a rectangle defined by the center line endpoints and the
        width of the rectangle.
    :param x1: X location of the center line first endpoint.
    :param y1: Y location of the center line first endpoint.
    :param x2: X location of the center line second endpoint.
    :param y2: Y location of the center line second endpoint.
    :param w: Width of the rectangle.
    :param offset: Offset allows for the creation of a rectangle that is
        offset by a small distance from the initially prescribed one on all
        sides.
    """

    def __init__(self, x1: float, y1: float, x2: float, y2: float, w: float,
        offset: float = 0):
        self.x1, self.x2 = x1, x2
        self.y1, self.y2 = y1, y2
        self.w = w

        dx, dy = self.x2 - self.x1, self.y2 - self.y1
        self.angle = np.arctan2(dy, dx)
        self.x1, self.x2 = self.x1 - offset * np.cos(self.angle), self.x2 +
            offset * np.cos(self.angle)
        self.y1, self.y2 = self.y1 - offset * np.sin(self.angle), self.y2 +
            offset * np.sin(self.angle)
        dx, dy = self.x2 - self.x1, self.y2 - self.y1

        self.length = np.sqrt(dx * dx + dy * dy)
        self.Cx1, self.Cy1 = (self.x1 + self.x2) / 2, (self.y1 + self.y2) / 2
        self.angleNormal = self.angle + np.pi / 2
        self.Cx2, self.Cy2 = self.Cx1 + (self.w / 2 + offset) * np.cos(self.
            angleNormal), self.Cy1 + (
                self.w / 2 + offset) * np.sin(
```

```
            self.angleNormal)
        self.Cx3, self.Cy3 = self.Cx1 - (self.w / 2 + offset) * np.cos(self.
            angleNormal), self.Cy1 - (
                self.w / 2 + offset) * np.sin(
            self.angleNormal)
        # Setting up the corner point coordinates
        # A *-----C2-----* C
        # 1 |             | 2
        # B *-----C3-----* D
        self.Ax = self.x1 + (self.w / 2 + offset) * np.cos(self.angleNormal)
        self.Ay = self.y1 + (self.w / 2 + offset) * np.sin(self.angleNormal)
        self.Bx = self.x1 - (self.w / 2 + offset) * np.cos(self.angleNormal)
        self.By = self.y1 - (self.w / 2 + offset) * np.sin(self.angleNormal)
        self.Cx = self.x2 + (self.w / 2 + offset) * np.cos(self.angleNormal)
        self.Cy = self.y2 + (self.w / 2 + offset) * np.sin(self.angleNormal)
        self.Dx = self.x2 - (self.w / 2 + offset) * np.cos(self.angleNormal)
        self.Dy = self.y2 - (self.w / 2 + offset) * np.sin(self.angleNormal)
        AB = Line(self.Ax, self.Ay, self.Bx, self.By, self.Cx1, self.Cy1)
        CD = Line(self.Cx, self.Cy, self.Dx, self.Dy, self.Cx1, self.Cy1)
        AC = Line(self.Ax, self.Ay, self.Cx, self.Cy, self.Cx1, self.Cy1)
        BD = Line(self.Bx, self.By, self.Dx, self.Dy, self.Cx1, self.Cy1)
        self.Lines = [AB, CD, AC, BD]



    def mirrorX(self, x_line):
        return Rectangle(-(self.x1 - x_line), self.y1, -(self.x2 - x_line),
            self.y2, self.w)

    def translate(self, transform):
        return Rectangle(self.x1 + transform[0], self.y1 + transform[1], self
            .x2 + transform[0], self.y2 + transform[1],
                         self.w)

    def rotate(self, point, angle):
        x1 = self.x1 - point[0]
        y1 = self.y1 - point[1]
        x2 = self.x2 - point[0]
        y2 = self.y2 - point[1]
        x1, y1 = x1 * np.cos(angle) - y1 * np.sin(angle), x1 * np.sin(angle)
            + y1 * np.cos(angle)
        x2, y2 = x2 * np.cos(angle) - y2 * np.sin(angle), x2 * np.sin(angle)
            + y2 * np.cos(angle)
        return Rectangle(x1 + point[0], y1 + point[1], x2 + point[0], y2 +
            point[1], self.w)

    def create_contour_rectangle(self, offset):
        return Rectangle(self.x1, self.y1, self.x2, self.y2, self.w, offset=
            offset)
```

```
    def plot(self, color: str = "blue", constructionLines: bool = True,
        add_length: bool = False, nr:str = None):
        if add_length:
            plt.annotate(f"{self.length:.0f} mm", (self.Cx1, self.Cy1))
        if nr is not None:
            plt.annotate("#"+nr, (self.Cx1, self.Cy1), color="red", fontsize
                =8, ha="center", va="center")
        for Line in self.Lines:
            Line.plot(color, constructionLines)


class DesignGeometry:
    def __init__(self, File, verbose=False):
        wb = load_workbook(filename=File)
        sheet = wb["Sheet"]
        startRow = 2
        row = startRow
        inRange = True
        while inRange:
            row += 1
            inRange = False if sheet["A" + str(row)].value is None else True
                # Break once it reaches the end
            # print(f"Row: {row} :::: Val: {sheet["A"+str(row)].value}")
        startRow += 1
        endRow = row
        self.SubRectLST = []
        self.TapeRectLST = []
        for i in range(startRow, endRow):
            ReadColumn = lambda x: float(sheet[x + str(i)].value)
            self.SubRectLST.append(
                Rectangle(ReadColumn("A"), ReadColumn("B"), ReadColumn("C"),
                    ReadColumn("D"), ReadColumn("E")))
            self.TapeRectLST.append(
                Rectangle(ReadColumn("F"), ReadColumn("G"), ReadColumn("H"),
                    ReadColumn("I"), ReadColumn("J")))

        if verbose:
            for i in range(startRow, endRow):
                ReadColumn = lambda x: sheet[x + str(i)].value
                print(
                    f"Row: {i} Substrate\t - X1: {ReadColumn("A"):^3.2f} - Y1
                        : {ReadColumn("B"):^3.2f} - X2: {ReadColumn("C"):^3.2f
                        } - Y2: {ReadColumn("D"):^3.2f} - Width: {ReadColumn("
                        E"):^3.2f}")
                print(
                    f"Row: {i} Tape\t\t\t - X1: {ReadColumn("F"):^3.2f} - Y1:
                        {ReadColumn("G"):^3.2f} - X2: {ReadColumn("H"):^3.2f}
                        - Y2: {ReadColumn("I"):^3.2f} - Width: {ReadColumn("J
                        "):^3.2f}")
        self.calc_bounding_box(verbose)
```

```
def __add__(self, other):
    self.SubRectLST += other.SubRectLST
    self.TapeRectLST += other.TapeRectLST
    self.DomainRectLST += other.DomainRectLST[1:]
    return self

def create_domain(self, domain:Rectangle):
    self.DomainRectLST = [Rectangle(0, 360/2, 360, 360/2, 360), domain]

def calc_bounding_box(self, verbose=False):
    # Get max x and y
    self.xmax = max([self.SubRectLST[0].Ax, self.SubRectLST[0].Bx, self.
        SubRectLST[0].Cx, self.SubRectLST[0].Dx])
    self.xmin = min([self.SubRectLST[0].Ax, self.SubRectLST[0].Bx, self.
        SubRectLST[0].Cx, self.SubRectLST[0].Dx])
    self.ymax = max([self.SubRectLST[0].Ay, self.SubRectLST[0].By, self.
        SubRectLST[0].Cy, self.SubRectLST[0].Dy])
    self.ymin = min([self.SubRectLST[0].Ay, self.SubRectLST[0].By, self.
        SubRectLST[0].Cy, self.SubRectLST[0].Dy])
    if 1 < len(self.SubRectLST):
        for substrate in self.SubRectLST[1:]:
            self.xmax = max([self.xmax, substrate.Ax, substrate.Bx,
                substrate.Cx, substrate.Dx])
            self.xmin = min([self.xmin, substrate.Ax, substrate.Bx,
                substrate.Cx, substrate.Dx])
            self.ymax = max([self.ymax, substrate.Ay, substrate.By,
                substrate.Cy, substrate.Dy])
            self.ymin = min([self.ymin, substrate.Ay, substrate.By,
                substrate.Cy, substrate.Dy])
    if verbose:
        print(f"Bounding␣Box␣of␣\n"
              f"X:␣{self.xmax:.2f},␣{self.xmin:.2f}\n"
              f"Y:␣{self.ymax:.2f},␣{self.ymin:.2f}")

def mirrorX(self, x_line):
    imageLST = []
    for substrate in self.SubRectLST:
        substrate_image = substrate.mirrorX(x_line)
        imageLST.append(substrate_image)
    self.SubRectLST = self.SubRectLST + imageLST

    imageLST = []
    for tape in self.TapeRectLST:
        tape_image = tape.mirrorX(x_line)
        imageLST.append(tape_image)
    self.TapeRectLST = self.TapeRectLST + imageLST

    self.calc_bounding_box()
def translate_relative(self, coords: tuple):
```

```
        x, y = coords
        translate = (x, y)
        image: list[Rectangle] = []
        for substrate in self.SubRectLST:
            substrate_image = substrate.translate(translate)
            image.append(substrate_image)
        self.SubRectLST = image

        image = []
        for tape in self.TapeRectLST:
            tape_image = tape.translate(translate)
            image.append(tape_image)
        self.TapeRectLST = image

        image = []
        for domain in self.DomainRectLST[1:]:
            domain_image = domain.translate(translate)
            image.append(domain_image)
        self.DomainRectLST = [self.DomainRectLST[0]]+image

        self.calc_bounding_box()
    def translate_center_to(self, coords: tuple, use_domain=False, copy=False
        ):
        x, y = coords
        if use_domain:
            centerX, centerY = self.DomainRectLST[-1].Cx1, self.DomainRectLST
                [-1].Cy1
        else:
            centerX, centerY = ((self.xmin + self.xmax) / 2, (self.ymin +
                self.ymax) / 2)
        translate = (x - centerX, y - centerY)
        image:list[Rectangle] = []
        for substrate in self.SubRectLST:
            substrate_image = substrate.translate(translate)
            image.append(substrate_image)
        if copy:
            self.SubRectLST += image
        else:
            self.SubRectLST = image

        image = []
        for tape in self.TapeRectLST:
            tape_image = tape.translate(translate)
            image.append(tape_image)
        if copy:
            self.TapeRectLST += image
        else:
            self.TapeRectLST = image

        image = []
```

```
        for domain in self.DomainRectLST[1:]:
            domain_image = domain.translate(translate)
            image.append(domain_image)
        if copy:
            self.DomainRectLST += [self.DomainRectLST[0]]+image
        else:
            self.DomainRectLST = [self.DomainRectLST[0]]+image


        self.calc_bounding_box()
        print(f"Translated X - {translate[0]:.2f}\nTranslated Y - {translate
            [1]:.2f}")

    def translate_center_to_lst(self, coords: list, use_domain=False, copy=
        False):

        image_domain = []
        image_tape = []
        image_sub:list[Rectangle] = []
        for x, y in coords:
            if use_domain:
                centerX, centerY = self.DomainRectLST[-1].Cx1, self.
                    DomainRectLST[-1].Cy1
            else:
                centerX, centerY = ((self.xmin + self.xmax) / 2, (self.ymin +
                     self.ymax) / 2)
            translate = (x - centerX, y - centerY)
            for substrate in self.SubRectLST:
                substrate_image = substrate.translate(translate)
                image_sub.append(substrate_image)

            for tape in self.TapeRectLST:
                tape_image = tape.translate(translate)
                image_tape.append(tape_image)

            for domain in self.DomainRectLST[1:]:
                domain_image = domain.translate(translate)
                image_domain.append(domain_image)
        if copy:
            self.SubRectLST += image_sub
            self.TapeRectLST += image_tape
            self.DomainRectLST += [self.DomainRectLST[0]]+image_domain
        else:
            self.SubRectLST = image_sub
            self.TapeRectLST = image_tape
            self.DomainRectLST = [self.DomainRectLST[0]]+image_domain


        self.calc_bounding_box()
        print(f"Translated X - {translate[0]:.2f}\nTranslated Y - {translate
```

```
        [1]:.2f}")

    def rotate_about_center(self, angle):
        center_x, center_y = ((self.xmin + self.xmax) / 2, (self.ymin + self.
            ymax) / 2)
        point = (center_x, center_y)
        image:list[Rectangle] = []
        for substrate in self.SubRectLST:
            substrate_image = substrate.rotate(point, np.deg2rad(angle))
            image.append(substrate_image)
        self.SubRectLST = image

        image = []
        for tape in self.TapeRectLST:
            tape_image = tape.rotate(point, np.deg2rad(angle))
            image.append(tape_image)
        self.TapeRectLST = image

        self.calc_bounding_box()

    def plot(self, show=True, on_plate=True, add_length=False, nr=False, save
        =False):
        for rect in self.SubRectLST:
            rect.plot(constructionLines=False)
        for i, rect in enumerate(self.TapeRectLST):
            rect.plot(color="yellow", constructionLines=False, add_length=
                add_length, nr=f"{i+1}" if nr else None)
        for rect in self.DomainRectLST:
            rect.plot(color="red", constructionLines=False)
        ax = plt.gca()
        if on_plate:
            ax.set_xlim(0, 360)
            ax.set_ylim(0, 360)
        ax.set_aspect('equal', adjustable='box')
        if save:
            plt.savefig("temp.png")
        if show:
            plt.show()

    def create_bom(self):
        tape_lengths = []
        for rect in self.TapeRectLST:
            tape_lengths.append(int(round(float(rect.length),0)))
        print(sorted(tape_lengths))
        bom = [(i+1, tape_lengths) for i, tape_lengths in enumerate(
            tape_lengths)]
        print(bom)
        for i in bom:
            print(f"Tape␣Nr␣{i[0]:>5}␣Tape␣Length␣{i[1]:>5}␣mm␣\t\ t  \n\n")
```

```
def create_fusion_file(self, show=True):
    mm_to_cm = lambda x: x * 0.1
    # Set a clearance to allow the tape to enter the pocket
    self.tape_clearance = 0.2  # mm
    with open(r'C:\Users\David\My_Drive\Aerospace\Master\8_Thesis\Code\
        SampleTapeTopOp\output\Fusion.txt', 'w') as file:
        for rect in self.SubRectLST:
            file.write(
                f"{mm_to_cm(rect.Ax)},{mm_to_cm(rect.Ay)},{mm_to_cm(rect.
                    Bx)},{mm_to_cm(rect.By)},{mm_to_cm(rect.Cx)},{mm_to_cm
                    (rect.Cy)}\n")
            rect.plot(color="blue", constructionLines=False)
        file.write("-\n")
        for rect in self.TapeRectLST:
            rect.plot(color="yellow", constructionLines=False)
            rect = rect.create_contour_rectangle(offset=self.
                tape_clearance)
            rect.plot(color="orange", constructionLines=False)
            file.write(
                f"{mm_to_cm(rect.Ax)},{mm_to_cm(rect.Ay)},{mm_to_cm(rect.
                    Bx)},{mm_to_cm(rect.By)},{mm_to_cm(rect.Cx)},{mm_to_cm
                    (rect.Cy)}\n")
        file.write("-\n")
        for rect in self.DomainRectLST:
            rect.plot(color="red", constructionLines=False)
            file.write(
                f"{mm_to_cm(rect.Ax)},{mm_to_cm(rect.Ay)},{mm_to_cm(rect.
                    Bx)},{mm_to_cm(rect.By)},{mm_to_cm(rect.Cx)},{mm_to_cm
                    (rect.Cy)}\n")
        ax = plt.gca()
        ax.set_aspect('equal', adjustable='box')
        if show: plt.show()

def create_compacting_gcode(self, compacting_plane, layer, center_loc=
    None, compact_sides=True, using_domain=False, show=False):
    """
    Generates gcode for the compactor to attach the tape onto the 3d
        print.
    The rotation is not taken into account so the model must NOT be
        rotated in the slicer.
    :param layer: File addon to indicate which layer it is
    :param compact_sides: A boolean that determines if the compactor
        should also take a path along the sides.
    :param center_loc: The location of the center of the model on the
        Prusa slicer.
    :param compacting_plane: The height of the print at the pause.
    :return: None
    """
    z = compacting_plane
    self.tool_radius = 6 # mm
```

```
# Going from top op coordinates to origin in center of model
    coordinates
if not using_domain:
    x_offset, y_offset = (self.xmax + self.xmin) / 2, (self.ymax +
        self.ymin) / 2  # Removed
else:
    raise NotImplementedError

if center_loc is None:
    to_global_x = lambda x: x #- x_offset
    to_global_y = lambda y: y #- y_offset
else:
    x_c, y_c = center_loc
    to_global_x = lambda x: x + x_c - x_offset
    to_global_y = lambda y: y + y_c - y_offset

self.plot(show=False, on_plate=True)
with open(rf"C:\Users\David\My␣Drive\Aerospace\Master\8_Thesis\Code\
    SampleTapeTopOp\output\Compacting_gcode_{layer}.txt", "w") as file
    :
    file.write("P0␣S1␣L2␣D0\n")  # Park current tool
    #file.write("M0\n")  # Pause
    # Place tapes
    file.write("T3␣S1␣L0␣D0\n")  # Pick up compactor tool
    # Assume clearance of 10mm
    clearance = 10  # mm
    speed = 2.5 * 60  # mm/min

    z = z - 2.2  # correction for tool length
    file.write("M109␣S280␣T3\n")  # Set "Extruder" temperature
    def stamp(coord):
        # Stamp middle
        file.write(
            f"G1␣X{coord[0]}␣Y{coord[1]}␣Z{z␣+␣clearance}␣F{speed␣*␣
                6}\n")  # First travel is long so 6x speed
        file.write(f"G1␣X{coord[0]}␣Y{coord[1]}␣Z{z}␣F{speed}\n")
        file.write(f"G4␣S2\n")  # Sleep 2 seconds
        file.write(f"G1␣X{coord[0]}␣Y{coord[1]}␣Z{z␣+␣clearance}␣F{
            speed}\n")
        file.write(f"G4␣S4\n")  # Sleep 4 seconds to allow cooling

    def iron_between(coord1, coord2):
        file.write(f"G1␣X{to_global_x(coord1[0])}␣Y{to_global_y(
            coord1[1])}␣Z{z␣+␣clearance}␣F{speed␣*␣6}\n")
        file.write(f"G1␣X{to_global_x(coord1[0])}␣Y{to_global_y(
            coord1[1])}␣Z{z}␣F{speed}\n")
        file.write(f"G1␣X{to_global_x(coord2[0])}␣Y{to_global_y(
            coord2[1])}␣Z{z}␣F{speed}\n")
        file.write(f"G1␣X{to_global_x(coord2[0])}␣Y{to_global_y(
            coord2[1])}␣Z{z␣+␣clearance}␣F{speed}\n")
```

```
            #plt.plot([coord1[0], coord2[0]], [coord1[1], coord2[1]],
                linestyle='-', color='r', alpha=0.3, linewidth=6)
            plot_slot(coord1, coord2, 12, filled=True, facecolor="red",
                edgecolor="black", ax=plt.gca(), alpha=0.3)



        # Stamp all the tapes in place
        for i, Tape in enumerate(self.TapeRectLST):
            print(f"Stamp Middle Loc (local): {Tape.Cx1:.2f}, {Tape.Cy1
                :.2f}")
            print(f"Stamp Middle Loc (global): {to_global_x(Tape.Cx1):.2f
                }, {to_global_y(Tape.Cy1):.2f}")
            print(f"Offset: {x_offset:.2f}, {y_offset:.2f}")
            print(f"x max/x min: {self.xmax:.2f}, {self.xmin:.2f}")
            print(f"y max/y min: {self.ymax:.2f}, {self.ymin:.2f}")

            file.write(f"M0 (Insert tape #{i+1})\n")  # Pause
            # Stamp middle of tape
            stamp((to_global_x(Tape.Cx1), to_global_y(Tape.Cy1)))
            # Stamp corners of tape
            # stamp((to_global_x(Tape.Ax), to_global_y(Tape.Ay)))
            # stamp((to_global_x(Tape.Cx), to_global_y(Tape.Cy)))
            # stamp((to_global_x(Tape.Bx), to_global_y(Tape.By)))
            # stamp((to_global_x(Tape.Dx), to_global_y(Tape.Dy)))

        # Iron all the tapes
        # for Tape in self.TapeRectLST:
            # Iron out from middle
            tool_path_rectangle = Tape.create_contour_rectangle(offset=-
                self.tool_radius+self.tape_clearance)
            # C1->1
            iron_between([tool_path_rectangle.Cx1, tool_path_rectangle.
                Cy1], [tool_path_rectangle.x1, tool_path_rectangle.y1])
            # C1->2
            iron_between([tool_path_rectangle.Cx1, tool_path_rectangle.
                Cy1], [tool_path_rectangle.x2, tool_path_rectangle.y2])
            if compact_sides:
                # C2->C
                iron_between([tool_path_rectangle.Cx2,
                    tool_path_rectangle.Cy2], [tool_path_rectangle.Cx,
                    tool_path_rectangle.Cy])
                # C3->B
                iron_between([tool_path_rectangle.Cx3,
                    tool_path_rectangle.Cy3], [tool_path_rectangle.Bx,
                    tool_path_rectangle.By])
                # C2->A
                iron_between([tool_path_rectangle.Cx2,
                    tool_path_rectangle.Cy2], [tool_path_rectangle.Ax,
```

```
                    tool_path_rectangle.Ay])
                # C3->D
                iron_between([tool_path_rectangle.Cx3,
                    tool_path_rectangle.Cy3], [tool_path_rectangle.Dx,
                    tool_path_rectangle.Dy])

            # Move tool out of the way
            file.write(f"G1 X{330} Y{330} Z{z + clearance} F{speed * 6}\n
                ")

        # Switch back to tool 1
        file.write("P0 S1 L2 D0\n")  # Park current tool
        file.write("T0 S1 L0 D0\n")  # Pick up initial tool
        if show:
            plt.show()

    def slice(self):
        pass


if __name__ == "__main__":
    A = Vec2(0, 1)
    B = Vec2(1, 1)
    AB = Ray2(A, B, 2)
    ax = plt.gca()
    ax.set_aspect('equal', adjustable='box')
    AB.plot()
    plt.show()
```

Listing A.2: Code to transform GPTO designs into sketches on fusion

```
#Author-
#Description-
import adsk.core, adsk.fusion, adsk.cam, traceback

def run(context):
    ui = None
    try:
        app = adsk.core.Application.get()
        ui = app.userInterface
        ui.messageBox('Generating Sketch')
        design = adsk.fusion.Design.cast(app.activeProduct)
        rootComponent = design.rootComponent

        # Loading design
        with open(r"/SampleTapeTopOp/Fusion.txt", "r") as file:
            lines = file.readlines()



        substrates = True
        sub, tape = [], []
        for i in lines:
            line = i.strip("\n")
            if line == "-":
                substrates = False
                continue
            if substrates:
                sub.append([float(j) for j in line.split(",")])
            else:
                tape.append([float(j) for j in line.split(",")])


        # Create sketch on the x-y plane
        sketches = rootComponent.sketches
        xyPlane = rootComponent.xYConstructionPlane
        sketch = sketches.add(xyPlane)

        # Initiate lines
        lines = sketch.sketchCurves.sketchLines

        # Draw rectangles
        for rectangle in sub:
            P1x, P1y, P2x, P2y, P3x, P3y = rectangle
            rectLines = lines.addThreePointRectangle(
                adsk.core.Point3D.create(P1x, P1y, 0),
                adsk.core.Point3D.create(P2x, P2y, 0),
                adsk.core.Point3D.create(P3x, P3y, 0)
            )
```

```
        # Create sketch on the x-y plane
        sketches = rootComponent.sketches
        xyPlane = rootComponent.xYConstructionPlane
        sketch = sketches.add(xyPlane)

        # Initiate lines
        lines = sketch.sketchCurves.sketchLines

        # Draw rectangles
        for rectangle in tape:
            P1x, P1y, P2x, P2y, P3x, P3y = rectangle
            rectLines = lines.addThreePointRectangle(
                adsk.core.Point3D.create(P1x, P1y, 0),
                adsk.core.Point3D.create(P2x, P2y, 0),
                adsk.core.Point3D.create(P3x, P3y, 0)
            )

    except:
        if ui:
            ui.messageBox('Failed:\n{}'.format(traceback.format_exc()))
```

B

Messerschmitt-Bölkow-Blohm Beam Experiments Photos

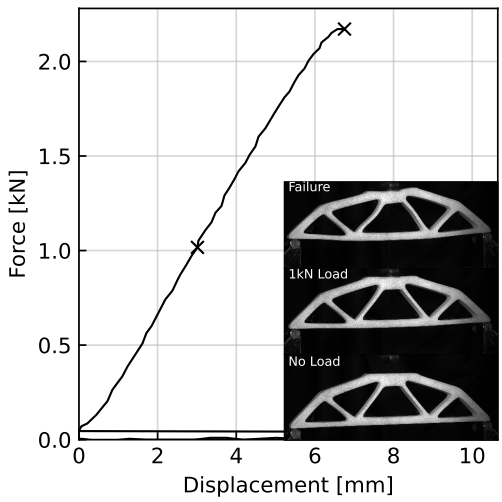

(a) DTO1

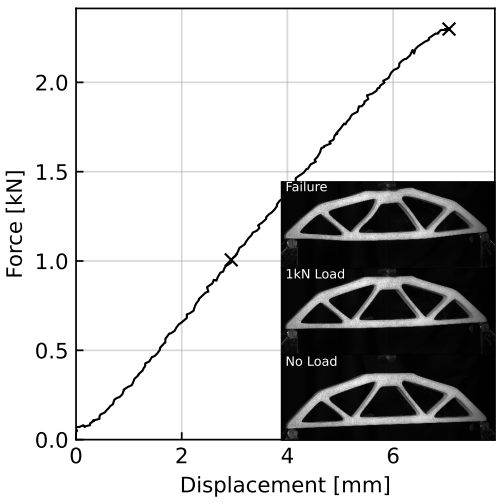

(b) DTO2

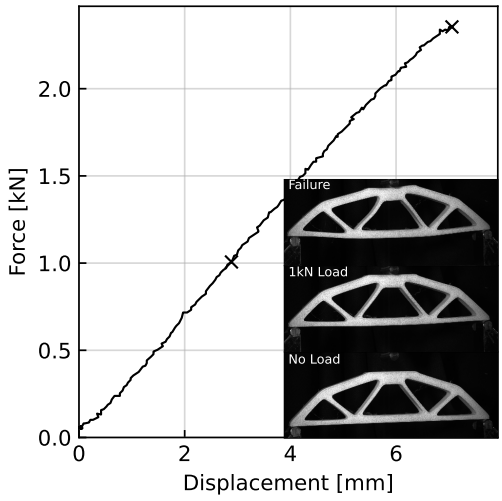

(c) DTO3

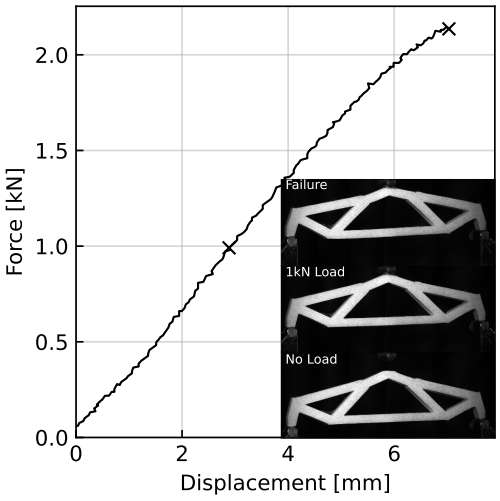

(d) GPTONT1

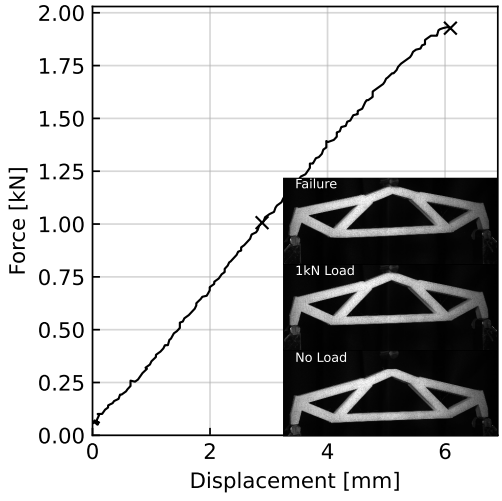

(e) GPTONT2

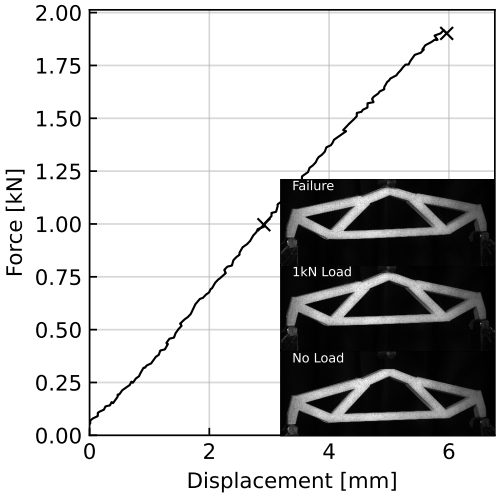

(f) GPTONT3

Figure B.1: Force-displacement graphs of MMB Beam samples DTO and GPTONT with images shown for key points: No load on the sample, 1kN of load and 1 frame after maximum load (Failure)

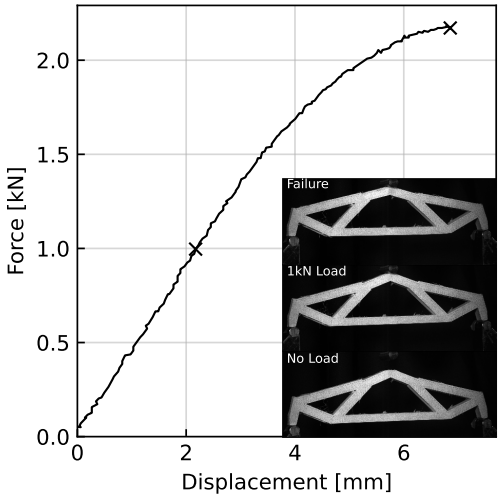

(a) GPTO1

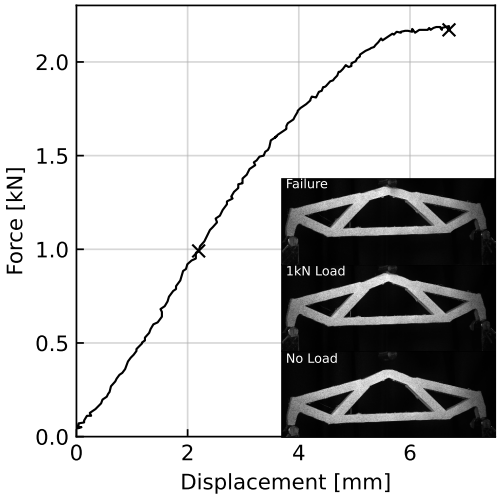

(b) GPTO2

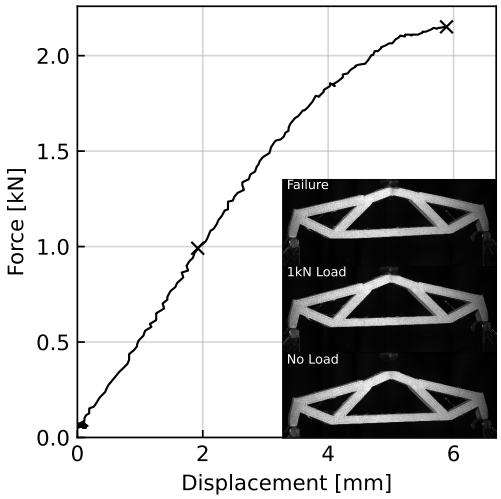

(c) GPTO3

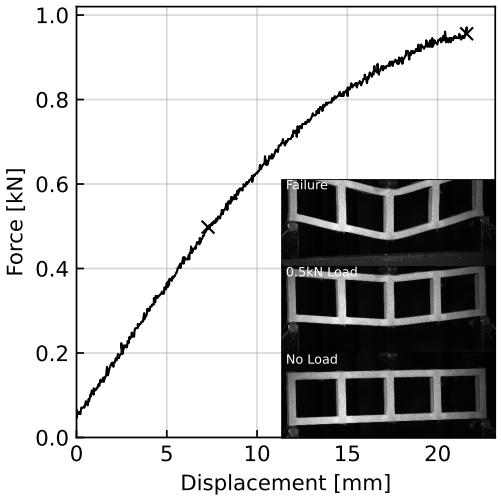

(d) GPTOGR1

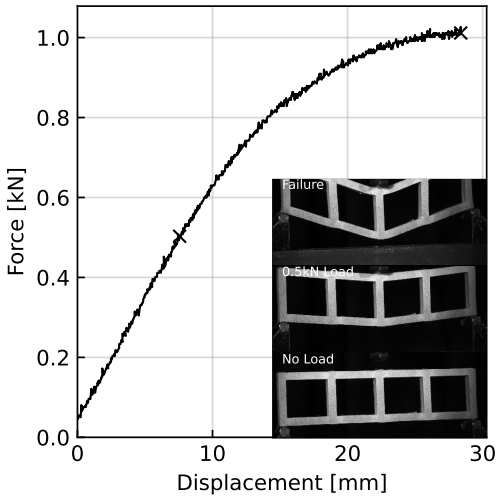

(e) GPTOGR2

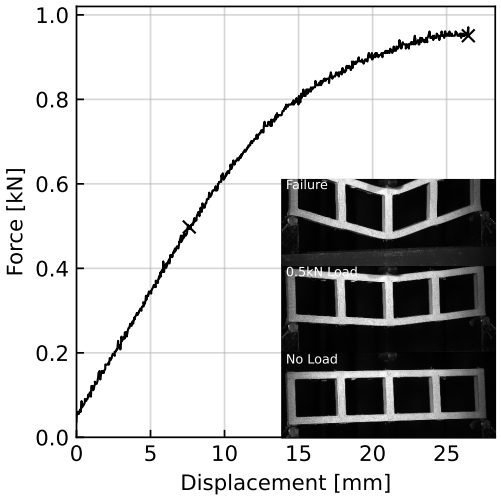

(f) GPTOGR3

Figure B.2: Force-displacement graphs of MMB Beam samples GPTO and GPTOGR with images shown for key points: No load on the sample, 1kN of load for GPTO and 0.5kN for GPTOGR and 1 frame after maximum load (Failure)

C

DIC Strains

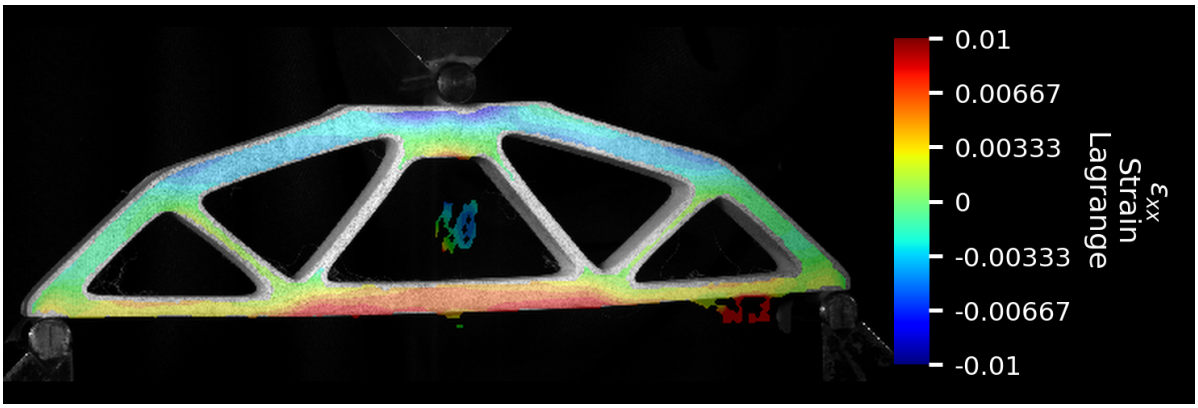

(a) Strain ϵ_{xx} DTO1

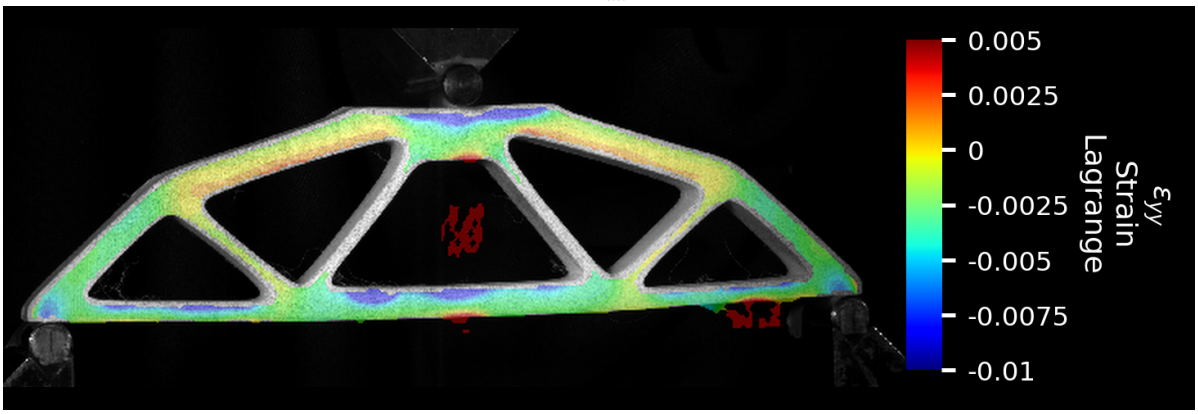

(b) Strain ϵ_{yy} DTO1

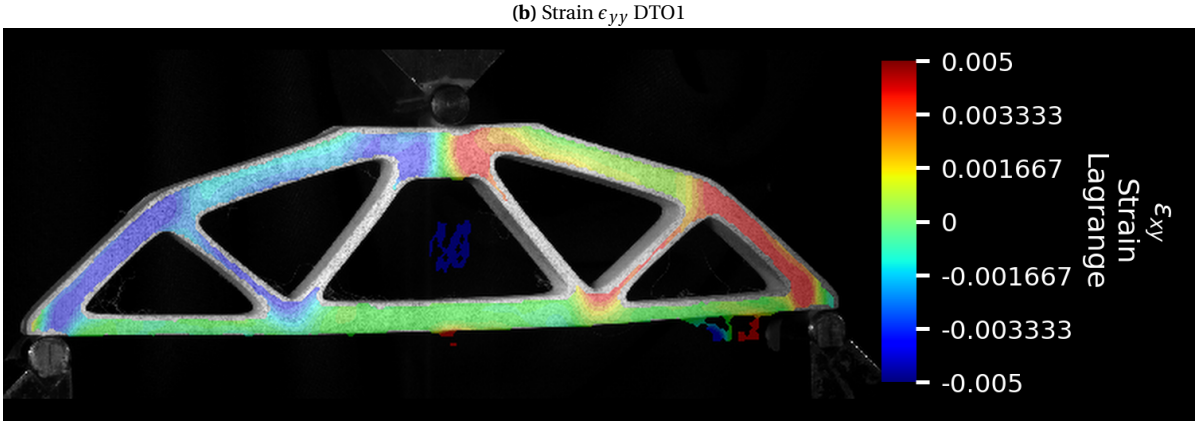

(c) Strain ϵ_{xy} DTO1

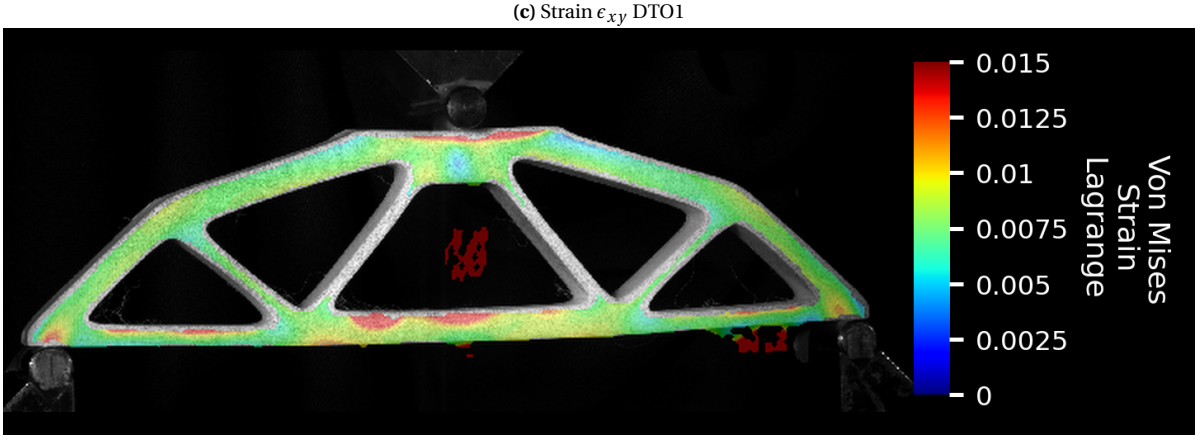

(d) Strain Von Mises ϵ_{vm} DTO1

Figure C.1: Strain on MBB Beam samples at 1kN of load using DIC separated between strain in the x direction ϵ_{xx}, strain in the y direction ϵ_{yy}, shear strain in the xy direction ϵ_{xy} and Von Mises strain ϵ_{vm}.

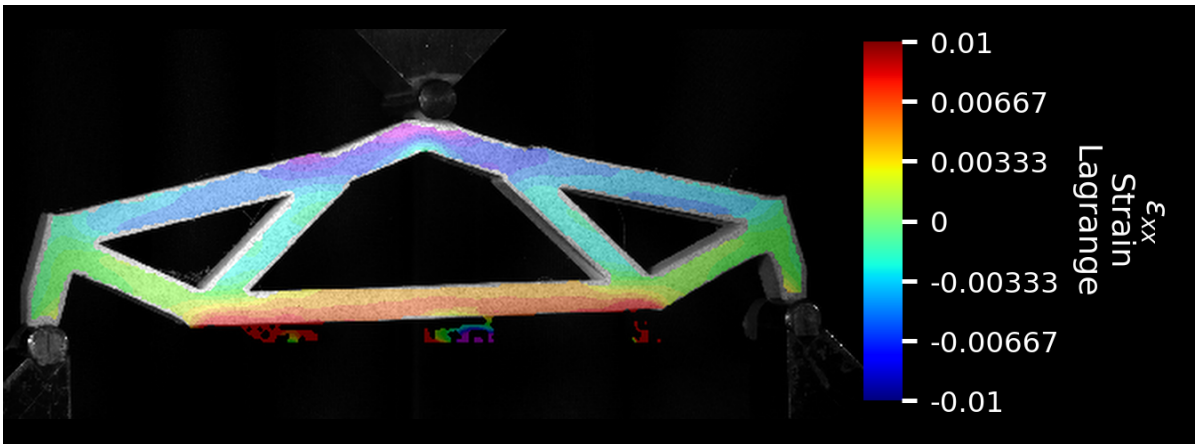

(a) Strain ϵ_{xx} GPTONT1

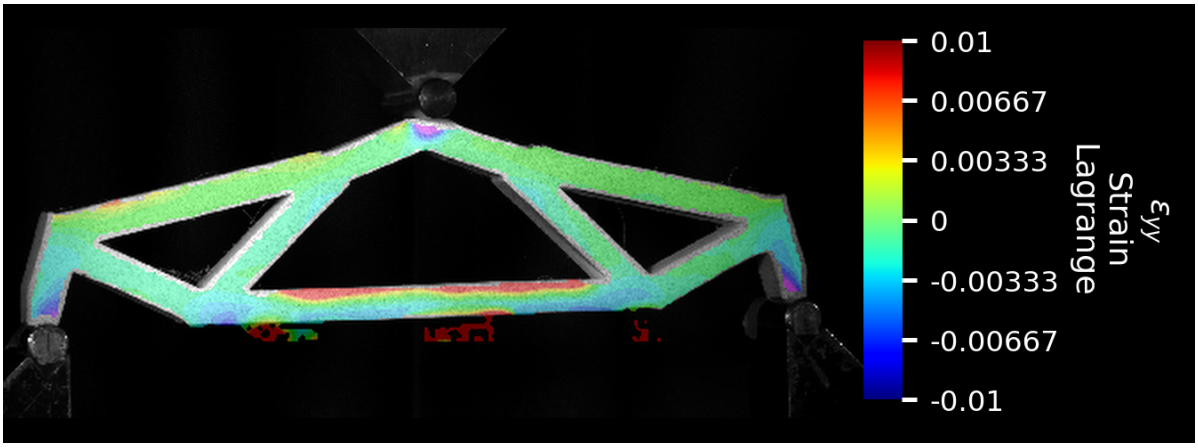

(b) Strain ϵ_{yy} GPTONT1

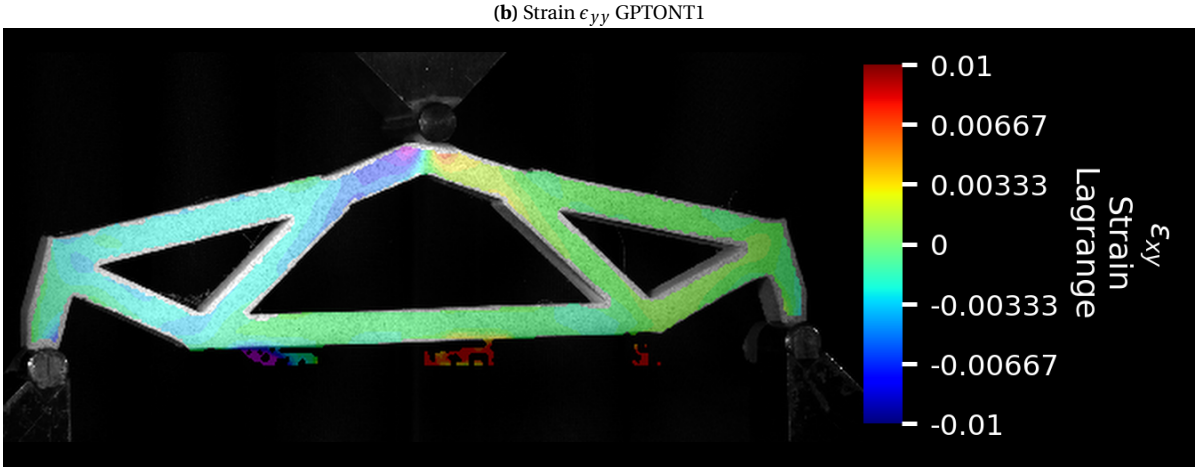

(c) Strain ϵ_{xy} GPTONT1

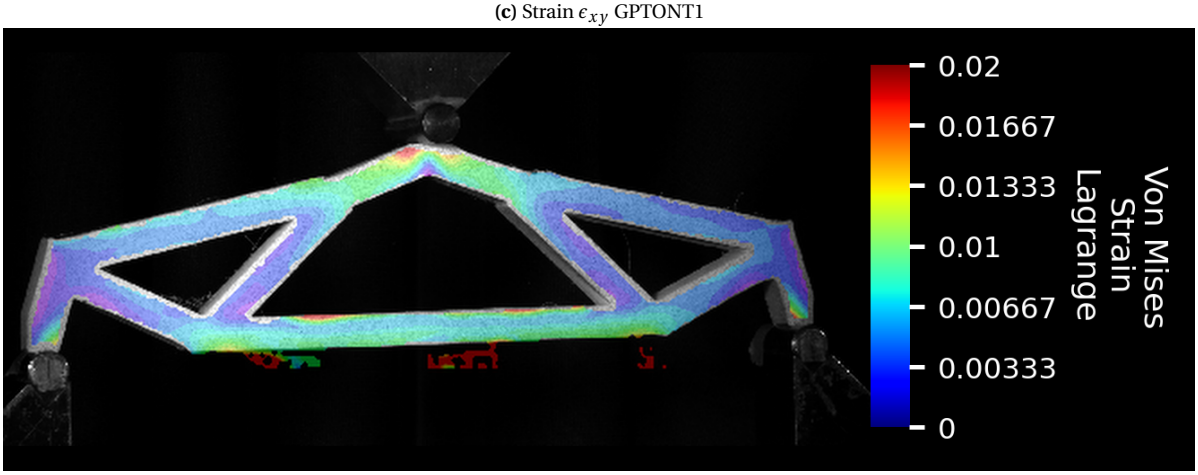

(d) Strain Von Mises ϵ_{vm} GPTONT1

Figure C.2: Strain on MBB Beam GPTONT1 sample at 1kN of load using DIC separated between strain in the x direction ϵ_{xx}, strain in the y direction ϵ_{yy}, shear strain in the xy direction ϵ_{xy} and Von Mises strain ϵ_{vm}.

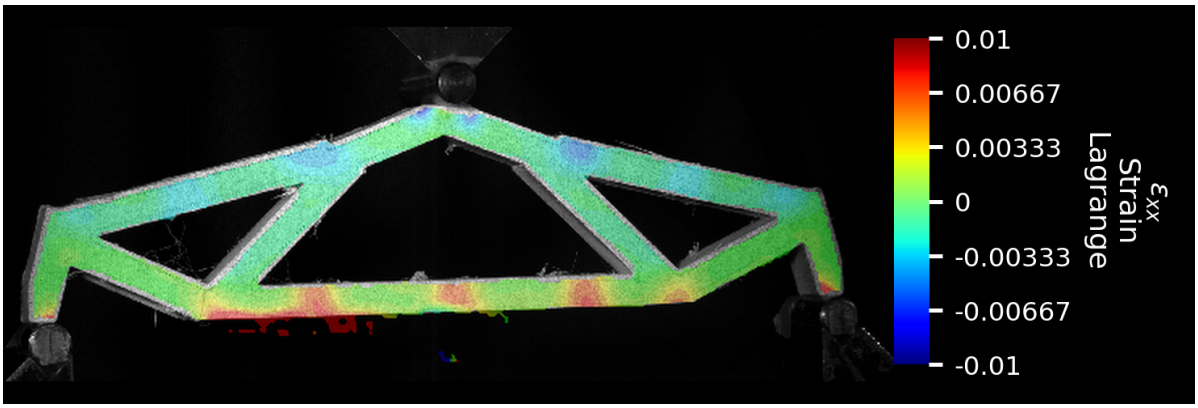

(a) Strain ϵ_{xx} GPTO1

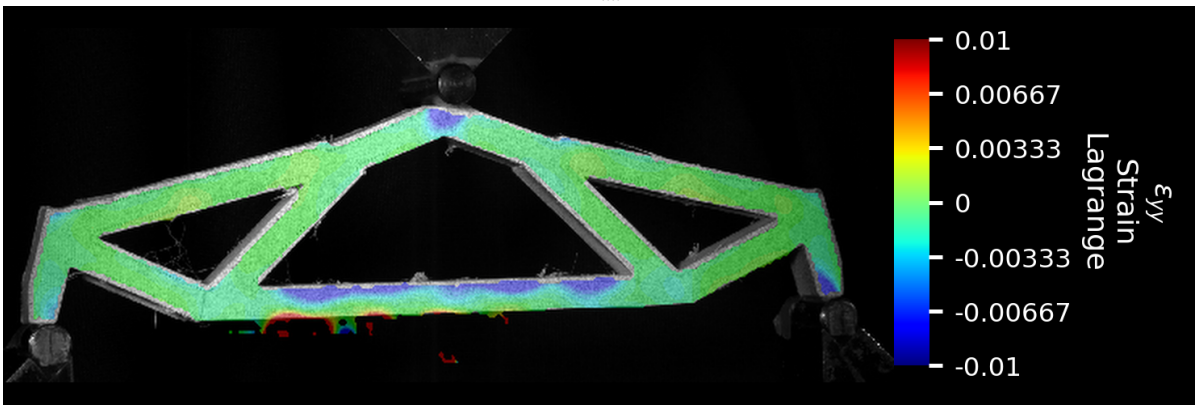

(b) Strain ϵ_{yy} GPTO1

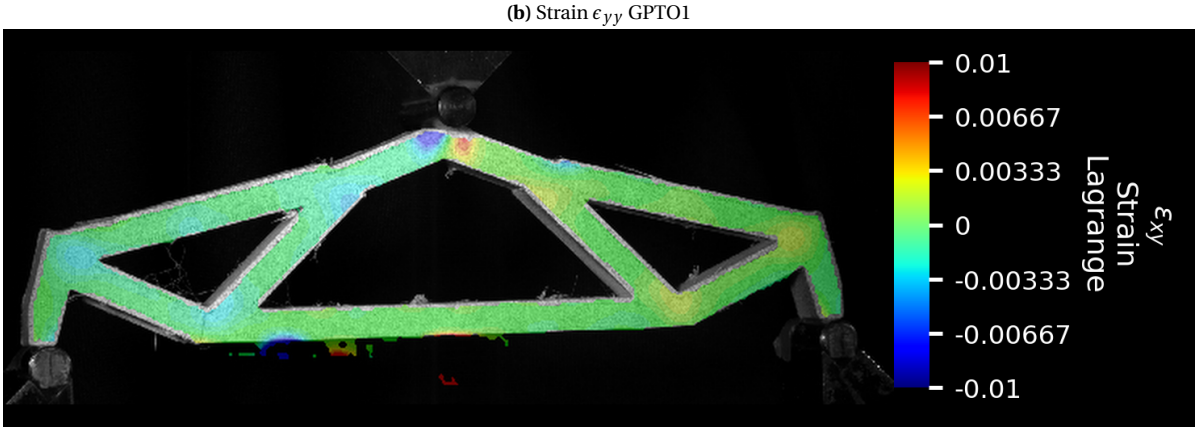

(c) Strain ϵ_{xy} GPTO1

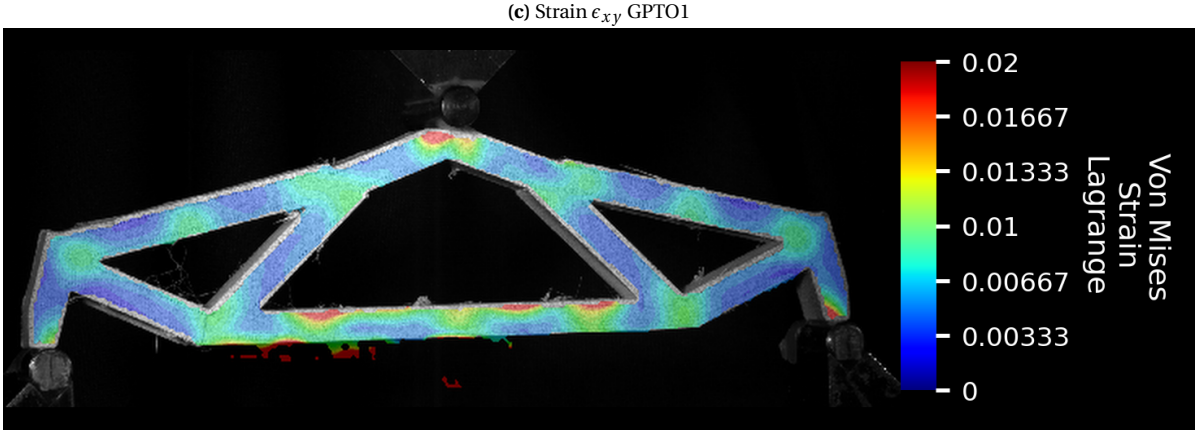

(d) Strain Von Mises ϵ_{vm} GPTO1

Figure C.3: Strain on MBB Beam GPTO sample at 1kN of load using DIC separated between strain in the x direction ϵ_{xx}, strain in the y direction ϵ_{yy}, shear strain in the xy direction ϵ_{xy} and Von Mises strain ϵ_{vm}.

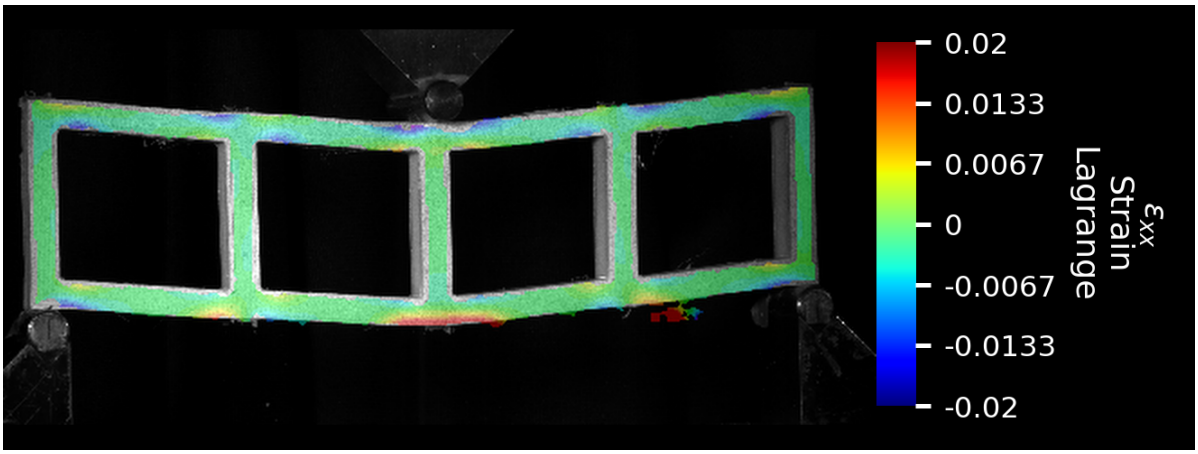

(a) Strain ϵ_{xx} GPTOGR1

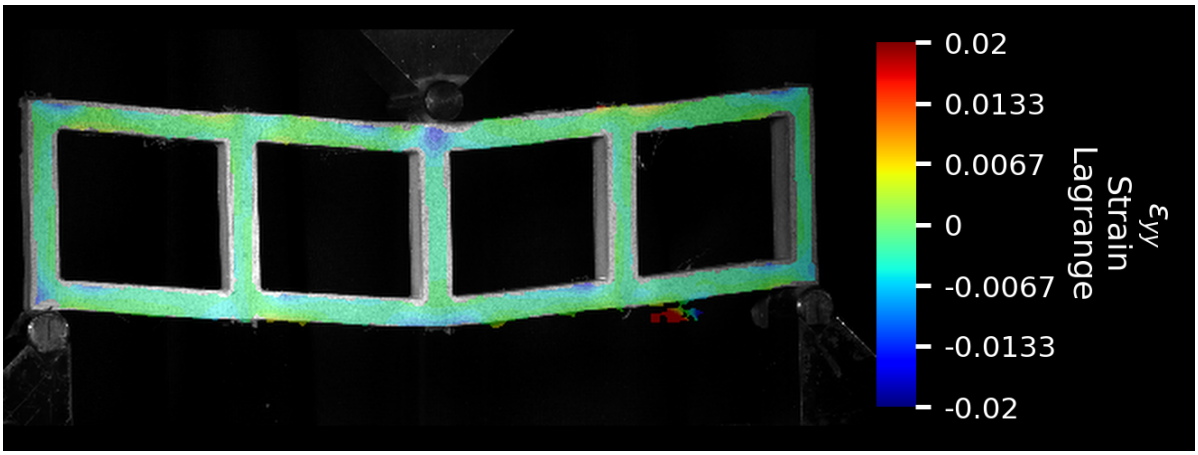

(b) Strain ϵ_{yy} GPTOGR1

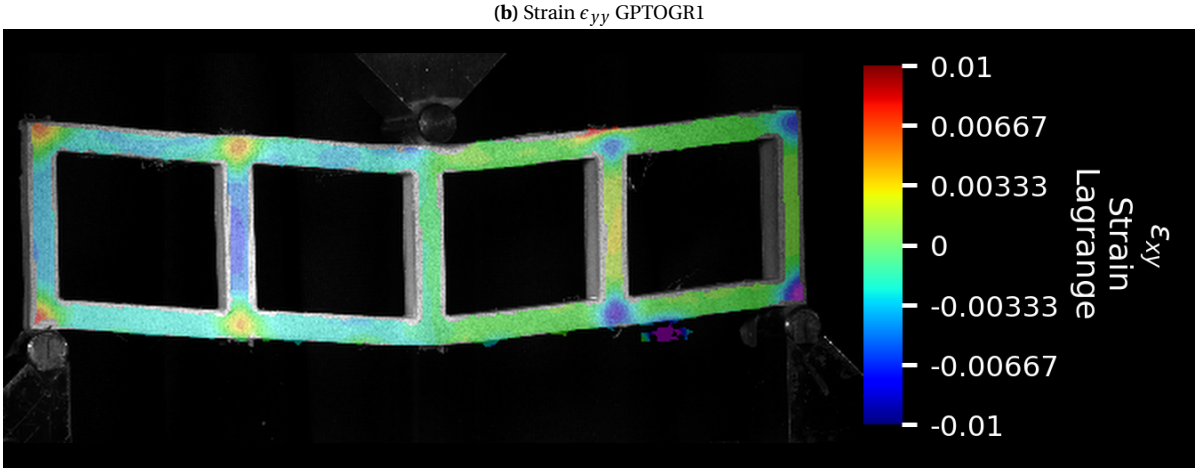

(c) Strain ϵ_{xy} GPTOGR1

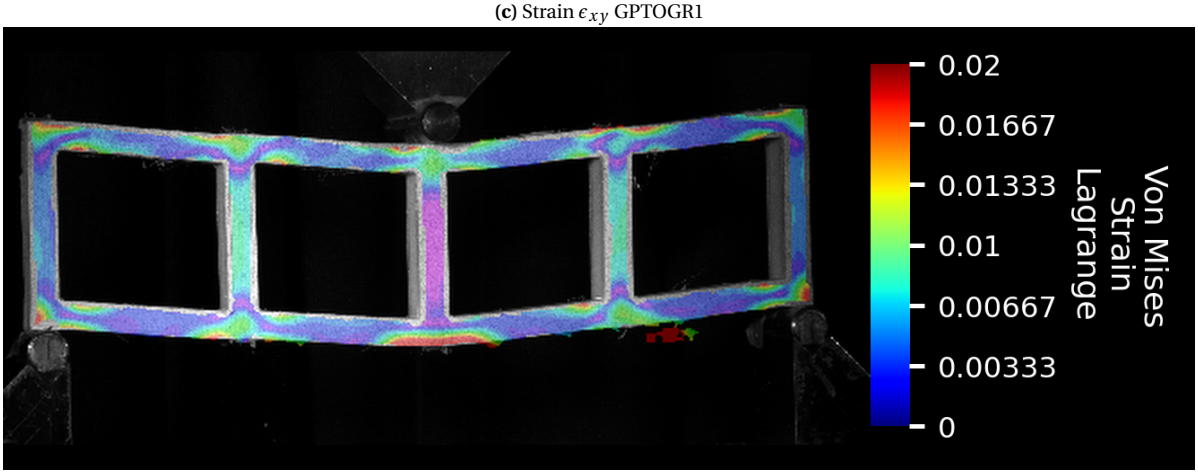

(d) Strain Von Mises ϵ_{vm} GPTOGR1

Figure C.4: Strain on MBB Beam GPTOGR1 sample at 1kN of load using DIC separated between strain in the x direction ϵ_{xx}, strain in the y direction ϵ_{yy}, shear strain in the xy direction ϵ_{xy} and Von Mises strain ϵ_{vm}.